

Doctoral thesis

Doctoral theses at NTNU, 2020:97

Stein-Martin Tilrum Fagerland

Nanoparticles, ultrasound and microbubble mediated drug delivery in cancer models

NTNU
Norwegian University of Science and Technology
Thesis for the Degree of
Philosophiae Doctor
Faculty of Medicine and Health Sciences
Department of Circulation and Medical Imaging



Norwegian University of
Science and Technology

Stein-Martin Tilrum Fagerland

Nanoparticles, ultrasound and microbubble mediated drug delivery in cancer models

Thesis for the Degree of Philosophiae Doctor

Trondheim, March 2020

Norwegian University of Science and Technology
Faculty of Medicine and Health Sciences
Department of Circulation and Medical Imaging



Norwegian University of
Science and Technology

NTNU

Norwegian University of Science and Technology

Thesis for the Degree of Philosophiae Doctor

Faculty of Medicine and Health Sciences
Department of Circulation and Medical Imaging

© Stein-Martin Tilrum Fagerland

ISBN 978-82-326-4546-6 (printed ver.)
ISBN 978-82-326-4547-3 (electronic ver.)
ISSN 1503-8181

Doctoral theses at NTNU, 2020:2020:97

Printed by NTNU Grafisk senter

Sammendrag

Denne avhandlingen omhandler forbedring av kreftbehandling gjennom økt levering av cellegift til kreftvev ved bruk av nanopartikler eller ultralyd kombinert med mikrobobler. Ved å kapsle cellegift inn i nanopartikler kan man øke leveringen av cellegiften til kreftvev på grunn av økt permeabilitet i blodårer i kreftvevet og manglende lymfatisk drenering fra kreftvevet. Økt levering av cellegift gjennom bruk av ultralyd og mikrobobler er antatt å skje på grunn av endringer i blodgjennomstrømming i kreftvevet, økt permeabilitet i kapillærene og dannelse av strømmer i væsken i ekstracellulær matriks. I denne avhandlingen brukte vi to ulike kreftmodeller for å studere effektene av nanopartikler og ultralyd med mikrobobler på leveringen av cellegift: Mus med immunsvikt med svulster dannet fra kreftcellerlinjer fra mennesker og en genmodifisert spontan prostatakreftmodell kalt 'transgenic adenocarcinoma of the mouse prostate' (TRAMP).

Levering av cellegift til svulster forbedres gjennom innkapsling i nanopartikler, men fordelingen av cellegift innad i svulsten er begrenset. I artikkel 1 undersøkte vi om ultralyd kunne forbedre leveringen av polymer-nanopartikler til svulster fra menneskelige kreftcellerlinjer i mus. Studien viste at ultralyd kan forbedre både opptak og fordelingen av nanopartikler i svulstene. Videre studier gjennomført av forskningsgruppen viste lovende resultat, og etter hvert ønsket vi å teste behandlingene i en kreftmodell som var mer representativ for kreft i mennesker. Dette førte til at vi begynte å jobbe med den spontane prostatakreftmodellen TRAMP. Imidlertid førte skiftet til en spontan kreftmodell til nye utfordringer, siden TRAMP-modellen utvikler ulike sykdomsfenotyper og har en uforutsigbar start og utvikling av sykdom. Målet med artikkel 2 var å bruke ultralyd- og MR-avbildning til å lette arbeidet med TRAMP-modellen. Vi viste at ultralyd-avbildning var en god metode for å oppdage aggressive, hurtigvoksende svulster i TRAMP-modellen og kunne brukes til å måle svulstvolum og at MR var best til å måle volumet av prostataen. Bruken av avbildning muliggjør inndeling i behandlingsgrupper basert på fenotype før behandling og longitudinelle målinger av behandlingsrespons. I artikkel 3 undersøkte vi behandlingseffekten av å kombinere nanopartikkel-innkapsling og ultralyd kombinert med mikrobobler sammen

med cellegiften cabazitaxel i TRAMP-modellen. Vi fant at cabazitaxel reduserte volumet av både svulster og prostata forbigående i TRAMP-modellen, men at volumet ikke ble redusert ytterligere ved innkapsling i nanopartikler eller kombinasjon med ultralyd og mikrobobler. Disse funnene skiller seg fra tidligere studier i mus med immunsvikt og svulster fra menneskelige kreftcellerlinjer.

Avhandlingens viktigste bidrag er bruken av en spontan prostatekreftmodell til å studere levering av cellegift gjennom innkapsling i nanopartikler og ultralyd kombinert med mikrobobler. Selv om avhandlingen ikke viste bedring i behandlingsrespons, har vi vist metoder for å forbedre studier i spontane kreftmodeller gjennom bruk av avbildning. En bedre forståelse av interaksjonene mellom nanopartikler og svulster, og ultralyd kombinert med mikrobobler og svulster, trengs for å optimalisere behandlingene og velge ut de pasientene som vil ha størst nytte av behandlingene.

Navn kandidat: Stein-Martin Tilrum Fagerland

Institutt: Institutt for sirkulasjon og bildediagnostikk

Veiledere: Førsteamanuensis Eva Hofslie, seniorforsker Sigrid Berg og professor Catharina de Lange Davies.

Finansieringskilde: NTNU og Norges forskningsråd

Ovennevnte avhandling er funnet verdig til å forsvares offentlig

for graden ph.d. i medisin og helsevitenskap.

Disputas finner sted i F2, Gamle fysikk, NTNU Gløshaugen

Fredag 20. mars , kl. 12.15

Abstract

This thesis is about improving cancer treatment by increasing delivery of chemotherapeutic agents to cancer tissue using nanoparticles (NPs) or ultrasound (US) combined with microbubbles (MBs). NP encapsulation is thought to improve drug delivery through the enhanced permeability and retention effect, which is accumulation of NPs in tumors because of permeable capillaries and lack of lymphatic drainage. Drug delivery through combination of US and MB (US+MB), also known as sonopermeation or sonoporation, is thought to work through altering tumor perfusion, capillary permeability and streams in the tumor extracellular matrix. In this thesis we used immunodeficient mice with xenografted prostate tumors and the spontaneous prostate cancer model transgenic adenocarcinoma of the mouse prostate (TRAMP) to study the effects of NP and US+MB on drug delivery.

NP encapsulation of drug improves drug delivery to tumors, but is still limited by low tumor penetration. In paper 1 we examined if US could improve delivery of polymeric NPs to xenografted prostate tumors in mice. The study showed that US can improve both uptake and distribution of NPs in tumors. The group continued with assessing the effect from NP and US+MB drug delivery on tumor volume and xenografted models with promising results. Further we wanted to move to models more representative of human disease and started using the TRAMP model. However, working with the TRAMP was challenging because it develops different disease phenotypes with an unpredictable debut and degree of disease. The aim of paper 2 was to address these challenges by using *in vivo* imaging for treatment group stratification based on phenotype and for measurement of treatment response. We showed that US could be used for screening for poorly differentiated tumors in the TRAMP model and that MRI had the lowest intraobserver variation when assessing prostate volume. In paper 3 we tested the treatment efficacy of NP and US mediated delivery of the chemotherapeutic drug cabazitaxel (Cab) in the TRAMP model. We found that Cab reduced both tumor and prostate volume but combining Cab with NPs or US+MB did not improve treatment efficacy. These findings are in contrast to NP and US+MB studies conducted in immunodeficient mice with xenografts.

The main novelty of this thesis is the application of NP and US+MB drug delivery in a spontaneous orthotopic prostate cancer model. Even if the thesis failed to prove increased therapeutic efficacy from NP and US+MB drug delivery, we have demonstrated methodology to improve studies in spontaneous cancer models using in vivo imaging. A deeper understanding of the interactions between NPs and tumors and US+MB and tumors is needed to optimize the treatments and to select the patients who will benefit the most from the treatments.

Acknowledgements

I would like to thank the Norwegian University of Science and Technology (NTNU) for founding my PhD and the Norwegian Research Council for funding parts of the experiments.

When I became part of the research group in 2012, through the medical student research program, I had enormous ambitions: The group was already doing nanoparticle and ultrasound treatment in mice, so I thought clinical testing and a revolution in cancer treatment was imminent. Many months and microscopy slides later my concerns had shifted from curing cancer to defect lasers and heterogenous tumors, so heterogenous that nothing would separate my plots of different treatment groups. I have been through this cycle of hope, enthusiasm and frustration many times by now and have so far carried on thanks to constructive support and enthusiasm from my fantastic research group, and especially my supervisor Catharina.

Thanks to my colleagues at biophysics for a great social life, it has been great to share ups and downs with you. I would also like to thank our collaborators from SINTEF, the MR cancer group, the MR core facility, comparative medicine core facility and the cellular and molecular imaging core facility for a good collaboration. I would never have accomplished what I did or gained any skills without all the experts surrounding me. Finally, I would like to thank my friends and family, and especially my dear Bergliot, for being understanding and supportive during the completion of my PhD.

List of papers

1 **Ultrasound-enhanced drug delivery in prostate cancer xenografts by nanoparticles stabilizing microbubbles**

Eggen S, Fagerland SM, Mørch Y, Hansen R, Søvik K, Berg S, Furu H, Dybvik Bøhn A, Borstad Lilledahl M, Angelsen A, Angelsen B, Davies C de L

Journal of Controlled Release

DOI: <http://dx.doi.org/10.1016/j.jconrel.2014.05.020>

2 **Ultrasound and magnetic resonance imaging for group stratification and treatment monitoring in the transgenic adenocarcinoma of the mouse prostate model**

Fagerland SM, Hill DK, van Wamel A, Davies C de L., Kim J

The Prostate

DOI: 10.1002/pros.23930

3 **Nanoparticle and ultrasound mediated delivery of chemotherapy in the transgenic adenocarcinoma of the mouse prostate model**

Fagerland SM, Berg S, Hill DK, Snipstad S, Sulheim E, Hyldbakk A, Kim J, Davies C de L

Manuscript in preparation

List of abbreviations

ARF	acoustic radiation force
Cab	cabazitaxel
ECM	extracellular matrix
MB	microbubble
MRI	magnetic resonance imaging
NP	nanoparticle
PD	poorly differentiated
PACA	poly(alkyl cyanoacrylate)
PEBCA	poly(2-ethyl-butyl cyanoacrylate)
TRAMP	transgenic adenocarcinoma of the mouse prostate
US	ultrasound
US+MB	ultrasound combined with microbubbles

Table of content

Sammendrag	I
Abstract.....	III
Acknowledgements	V
List of papers	VII
List of abbreviations	IX
Table of content.....	XI
Background.....	1
Objectives	9
Summary of papers.....	11
Discussion.....	13
Outlook.....	17
References	19
Papers	27

Background

Cancer treatment

Cancer is a broad range of diseases characterized by uncontrolled cell proliferation and metastasis. Cancer is the second leading cause of death globally, with estimated 9.6 million deaths in 2018¹. Treatment of cancer depend on the type and the stage of the cancer and the health and life expectancy of the patient. Generally, the goal of treatment can be curative, life pro-longing or palliative, focusing on symptom relief. The most commonly used treatments are surgery, radiotherapy and chemotherapy, used alone or in combination. Some types of cancer also respond to hormonal therapies or immunotherapy. Treatment of solid tumors often require local treatment with surgery or radiotherapy to be curative. Chemotherapy is used as curative treatment for some types of solid tumors but is more commonly used to reduce tumor volume before local treatment (neoadjuvant) or after local treatment to reduce risk of recurrence (adjuvant). In many metastatic types of solid cancers, chemotherapy is used to increase life expectancy or reduce symptoms. Prostate cancer is the most common cancer among males and had an estimated 450 000 new cases and 107 300 deaths in the European Union in 2018². The prognosis and treatment depend on the blood sample level of prostate specific antigen, the grading of biopsies (Gleason score) and the extent of the cancer (in the prostate, locally invasive or metastasized)³. Examples of treatment options are observation, surgical removal, radiotherapy, hormone therapy and chemotherapy. Chemotherapy is indicated for patients who present with metastatic disease or in patients with recurrence of prostate cancer after androgen deprivation therapy⁴. Chemotherapy improve overall survival, but the prognosis in these subgroups of prostate cancer remain poor. This thesis focuses on how the efficacy of chemotherapeutic drugs can be improved through increasing drug delivery using nanoparticle (NP) encapsulation or ultrasound combined with microbubbles (US+MB).

Nanoparticles

NPs are typically from tens to hundreds of nm in diameter and can be made from materials like phospholipids, polymers, carbon tubes, gold etc., and drugs can either be encapsulated or attached to the surface of the NP. This way, the drug pharmacokinetics can be altered to improve efficacy and reduce adverse effect. The first NP drug approved by the FDA was Doxil in 1995⁵, and since then seven other NP drugs for cancer treatment have reached the market^{6,7}. NPs improve drug delivery through the enhanced permeability and retention effect (EPR effect), which is caused by a combination of leaky capillaries and lack of lymphatic drainage. This allows NPs to extravasate from blood vessels into the extracellular matrix (ECM) and be retained within the tumor because of the lack of lymphatic drainage^{8,9}. However, the EPR effect is variable between different types of tumors and is heterogeneously distributed within tumors^{10,11}. NPs are usually administered intravenously and need to pass through several different compartments of the body before reaching cancer cells, this is often described in four steps: Circulating in the blood while avoiding excretion, exiting from the circulation into tumor ECM, moving through the tumor ECM and reaching cancer cells where the NP, or the drug from the NP, need to enter the target cells.

When NPs are administered intravenously, blood proteins will immediately adhere to the surface of the NPs. This layer of proteins is referred to as the protein corona and consist of hundreds of different types of proteins in many layers¹². The protein corona is crucial in determining the further fate of the NPs^{13,14}. The surface of NPs is often modified to avoid degradation and increase circulation half-life. One method is adding polyethylene glycol, which will attract water, reducing interactions between the NP and proteins in the blood to reduce excretion¹⁵. The NPs used in this thesis have been shown to accumulate mainly in the liver and spleen^{16,17}, which have fenestrated epithelial cells facilitation extravasation and have a high number of macrophages that can clear out NPs from circulation¹⁸. A review study of NP delivery to tumors calculated that a median 0.7% of the injected dose end up in the tumor, while the rest stays in the blood, other organs or is excreted¹⁹.

After reaching the tumor, the NPs need to extravasate into the tumor's ECM, a process that is enhanced by leaky tumor capillaries caused by a pathologic angiogenesis.

The content of the ECM varies between tumor types and within tumors, but generally consist of proteins like collagen and elastin, glycosaminoglycans like hyaluronic acid and cells like fibroblast and macrophages. The NPs need to pass through the spatial obstacles in the ECM to reach the cancer cells. This process is mainly driven by diffusion due to the high interstitial fluid pressure in most solid tumors^{20,21}. Diffusion is a slow process for large molecules and the increased size of NPs slows down the distribution throughout the ECM. The last step is for the NPs or the drug delivered by NPs is to enter the cancer cells. NPs are normally internalized by endocytosis, whereas hydrophobic drugs can diffuse through the plasma membrane. However, only a small amount of the injected drugs reach its target¹⁹ and the NPs are heterogeneously distributed and located mainly close to vessel wall^{10,11}. Thus, NP drug delivery has been combined with other therapies to further improve delivery. Our research group has focused on US+MB treatment to improve NP delivery to tumors.

Ultrasound and microbubbles in drug delivery

Combining US with MBs to improve delivery of drugs, also known as sonopermeation or sonoporation, have shown promise as a method to improve the therapeutic efficacy of chemotherapeutic drugs^{22,23} or NPs^{24,25} in tumors. This is thought to occur through altering blood perfusion, increasing capillary permeability and by facilitation drug transport through the ECM^{24,26}. Traditionally the biological effects of US have been separated into thermal effects and mechanical effects. Thermal effects are caused by absorption of energy from the US pulse to the medium it propagates through. The degree of local heating will depend on the frequency and power of the US and the properties of the sonicated tissue. Heating can increase drug transport by affecting blood perfusion, capillary permeability and increasing the diffusion rate of drugs in the tumor ECM. Mechanical effects are divided into acoustic radiation force (ARF) and cavitation. ARF occurs when the propagating US pulse transfers momentum to the medium it travels through and cause streaming in the same direction as the pulse²⁷. This can move MBs in the capillaries closer to the endothelial cells and can cause convection in the ECM, which can transport drugs in the direction of the US pulse²⁸. The ARF gets stronger at higher frequencies, at the cost of decreased depth penetration. Acoustic cavitation is the creation

and oscillation of gas bubbles in an acoustic field. Bubbles can be formed in the acoustic field during high negative pressures or MBs can be added artificially to create cavitation effects at lower pressures. During stable cavitation, the bubble oscillates around an equilibrium for relatively many cycles. The oscillation creates a stream of fluid around it, which can influence cells in the vicinity of the MB. Inertial cavitation happens at higher amplitudes than stable cavitation and is characterized by growth of the bubble radius per oscillation until the bubble implodes. This implosion creates shock waves around it and can create a jet stream if a solid surface is close²⁸. Both cavitation mechanisms increase permeability through effects on cells and the vessel wall in their vicinity. In human tissue high US pressures are needed for bubbles to appear through cavitation. Because of this, MBs are administered iv to enable cavitation effects at lower US pressures.

A wide range of US systems are being used in therapeutic US research and researchers within the field generally have three options: Use approved diagnostic systems and customize them for therapeutic application, built a custom set-up or buy a pre-built therapeutic set-up for clinical or research use. Diagnostic systems are available and approved for clinical use, making it easier to get approval for clinical trials. However, producers of diagnostic systems generally try to minimize US bioeffects, and systems are rarely configurable to match desired settings for US+MB therapy. Examples of therapeutic US applications for treatment of human disease are extracorporeal shockwave lithotripsy, for destruction of some types of kidney stone and the Exablate models from Insightec, which use MRI to guide high-intensity focused US for ablation therapy of uterine fibroids and localized prostate cancer, among other indications²⁹. There are also dedicated systems for pre-clinical therapeutic US+MB or ablation, like the systems provided by FUS instruments. Another option is to make a custom set-up with a transducer, amplifier and signal generator of choice. In paper 1 we used a custom set-up with a single element transducer and in paper 3 we used a system developed by FUS Instruments.

In addition to the US setup, the choice of MB is essential. MB size, material and gas are among important factors to consider^{30,31}. The MB's size affects the resonance frequency and the MBs need to be small enough to pass through capillaries, to increase circulation time. The material used will influence resonance frequency and the flexibility

of the shell, which will affect how the MB interact with the US pulse: Stiffer MBs will crack while more flexible MBs can resonate for several cycles. Some MBs contain the drug in the shell of the MB or associated to the surface, while most treatments with sonopermeation inject the therapeutic agent separate but close in time. The gas in the MB is important for stability, as an easy soluble gas will quickly dissolve into the blood, shortening the circulation time of the MB. Using approved US contrast agents like SonoVue or Sonazoid makes it easier to translate US+MB therapies into clinical studies, since US contrast agents are already approved for human use. A downside with this solution is that the MBs are not optimized for therapy. The size distribution is often wide and circulation time is relatively short. Clinically available MBs are also restricted to blood vessels and will have less effect on ECM transport and cancer cell uptake of drug. MBs developed specific for therapy can be made to resonate at a specific frequency to match the US setup and the size distribution can be narrowed down to create a more predictable effect or even make MBs that extravasate. Another possibility is to incorporate the drug in the MB, to make sure the drug is close to where the US treatment is strongest³². Figure 1 display some of the features of NP and US enhanced drug delivery. In paper 1 we use a combined NP and MB platform developed by SINTEF and in paper 3 we used the commercially available US contrast agent SonoVue.

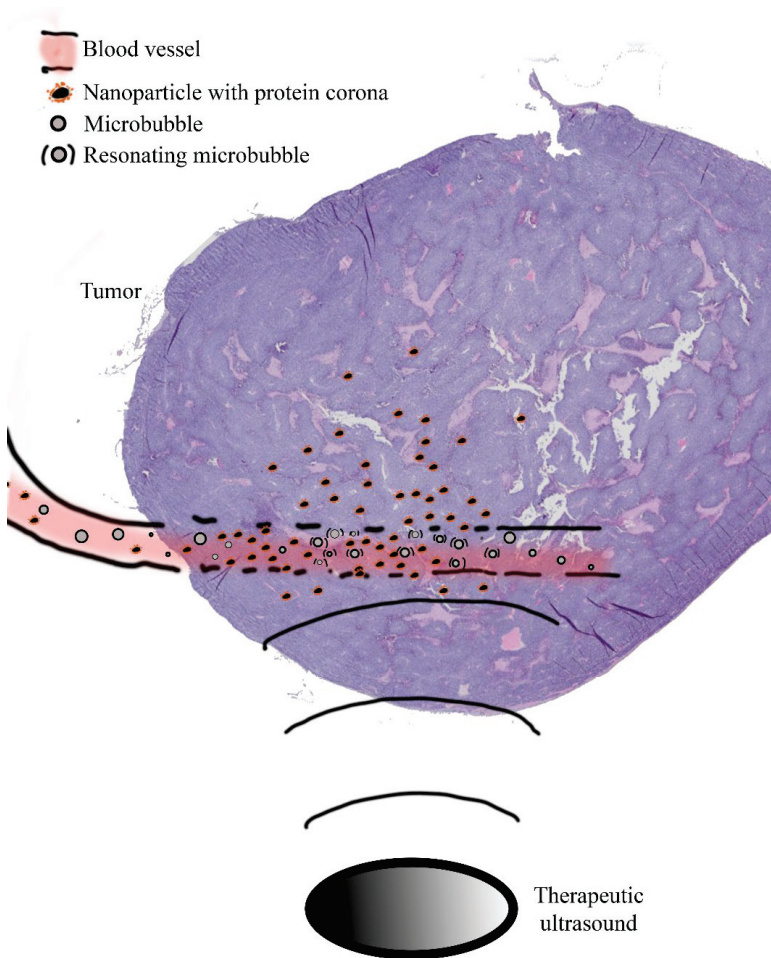


Figure 1:

Draft indicating some of the mechanisms of nanoparticle and ultrasound mediated drug delivery. Nanoparticles from the circulation leave through fenestrations in the tumor capillaries, aided by bioeffects created by ultrasound exposure. Resonating microbubbles enhance the effects of ultrasound further. The figure is not drawn to scale.

Cancer models

Cancer models are used both to study mechanisms involved in carcinogenesis and to study mechanisms and effects of cancer treatments. Cancer models are vital in selecting the

most promising treatments from pre-clinical testing for further development and clinical testing. Unfortunately, many novel drugs are not approved after clinical testing, despite promising results in cancer models³³. Improving cancer models could lead to a better selection of novel treatments and could bring more novel treatments to the clinic. A wide range of cancer models, both in vitro and in vivo, have been used to study the effects of NP and US+MB drug delivery^{23,24,26}.

In vitro experiments with immortalized cancer cells can be relevant for studying cellular uptake of drugs after treatments. For NP drug delivery studies, this could be used to either study the step from vasculature to ECM through endothelial cells or the last step of internalization into cancer cells. For US-MB research, it will only represent the extravasation step, since the MBs are confined to the intravascular space. To recapitulate all the steps of drug delivery, from intravenous administration to the target cancer cell, in vivo models are needed. The most commonly used in vivo cancer models are xenografted subcutaneous tumors in immunodeficient mice³³. These models have a relatively predictable natural course of their disease, making it easier to plan and execute experiments. However, several factors make them less representative of cancer in humans: The cancer genetics is more homogenous, since the cancer developed from immortalized cancer cell lines; the cancer is usually implanted outside its site of origin, preventing interplay between the cancer cells and the organ specific connective tissue; and the mice are immunodeficient, not taking into account the role of the immune system in cancer treatment³³. Genetically engineered models can address these shortcomings through a de novo carcinogenesis in the correct stroma in immunocompetent mice. In paper 2 and 3 we use a genetically engineered spontaneous prostate cancer model named the transgenic adenocarcinoma of the mouse prostate (TRAMP).

The TRAMP model was developed during the 1990s^{34,35} and has become a widely used prostate cancer model³⁶⁻³⁸. The carcinogenesis is driven by transcription of simian virus 40 (SV40) large T antigen under the prostate-specific rat probasin promoter. This leads to a relatively prostate specific expression of the SV40 large T antigen, which again leads to inhibition of several tumor suppressor genes, including p53 and Rb. The TRAMP mice develop cancer from cells that start out with a normal histology and gradually progress from mild to high grade of dysplasia before becoming malignant and

metastatic^{39,40}. A wide range of therapies have been tested in the TRAMP model, including diets⁴¹, supplements of silibinin⁴² or selen⁴³, non-steroidal anti-inflammatory drugs⁴⁴ and anti-angiogenic drugs⁴⁵. Most studies have assessed the cancer preventive effects of therapies and started therapy at an early age, before onset of disease. When assessing the treatment efficacy against established, cancer treatment should start later in life, when cancer has developed. Docetaxel⁴⁶ and doxorubicin⁴⁷ are among the few chemotherapeutic agents have been tested in the TRAMP model.

Objectives

The overall objective of this thesis was to improve cancer treatment through improved delivery of chemotherapeutic drugs by encapsulating drugs in NPs and combining drugs or NP-encapsulated drugs with therapeutic US and MBs.

The goal of paper 1 was to examine if US could enhance delivery and distribution of NPs in tumor xenografts in mice. Both NPs without MBs and a novel NP stabilizing MB platform was investigated. In addition, intravital microscopy was done to examine the in vivo distribution of NPs stabilizing MBs.

The goal of paper 2 was to find out if in vivo imaging could be used to alleviate some of the challenges faced when conducting studies in the TRAMP model. More specifically, the performance of US for prostate tumor screening and the intraobserver variation when assessing volume of tumor or prostate for both US and MRI, were assessed.

The goal of paper 3 was to assess the treatment efficacy of cabazitaxel with and without drug delivery through NPs and/or US+MB in the TRAMP model. After promising results in xenograft models, this was seen as a way to assess treatment efficacy in a model more representative of human disease.

Summary of papers

Paper 1 – Ultrasound-enhanced drug delivery in prostate cancer xenografts by nanoparticles stabilizing microbubbles

This paper was the first paper published from our group using SINTEF developed polymeric poly(alkyl cyanoacrylate) (PACA) NPs. The goal was to find out if US could enhance the delivery of NPs and NPs stabilizing MBs. In addition, intravital microscopy of tumors was done to study the extravasation of NPs stabilizing MBs. Tumors were grown from the prostate cancer cell line PC3 in Balb/c nude mice and NP uptake and distribution after different US exposures at different time points after injection of NPs were examined. A fluorescent dye was used as the model drug and the NP's payload. Blood vessels were stained with tomato lectin for visualization. The effects of US on NP delivery were assessed using confocal laser scanning microscopy both intravitaly and in tumor sections. All US treatments given minutes after NP administration were found to increase NP uptake. Treatment given 24 hours after NP administration did not increase uptake. Even though the uptake was improved on group level, the uptake was heterogenous both between tumors in the same treatment group and within the same tumor. Intravital microscopy confirmed a large variation in the extravasation of NPs.

Paper 2 – Ultrasound and magnetic resonance imaging for group stratification and treatment monitoring in the transgenic adenocarcinoma of the mouse prostate model

When we started working with the TRAMP model, the MR cancer group had a lot of experience doing MR imaging of the model. Since MR imaging was relatively time consuming and expensive compared to US imaging, we wanted to find out how US imaging performed compared to MR imaging for detection and volumetric analysis of TRAMP tumors and prostates. US imaging was an efficient method for detecting poorly differentiated tumors in the TRAMP model and performed good for measuring tumor volumes. Detection of poorly differentiated tumors in the TRAMP model is important because they progress quickly and mice with the phenotype needs to be euthanized within

weeks. By detecting the tumors before start of treatment, the inherent random variation in the TRAMP model can be reduced. MRI was superior for assessment of prostate volume, because of a lower intraobserver variation.

Paper 3 – Nanoparticle and ultrasound mediated delivery of chemotherapy in the transgenic adenocarcinoma of the mouse prostate model

NP encapsulation and US+MB drug delivery has shown promising results in xenografted tumors in immunodeficient mice and with this study we wanted to assess the efficacy of the treatments in a more clinically relevant cancer model. The efficacy of the chemotherapeutic agent cabazitaxel (Cab) by itself and combined with NP encapsulation or US+MB treatment was assessed in the TRAMP model. In addition, MS was used to compare the biodistribution of Cab after the different treatments. This was the first study we know of to examine these drug delivery methods in a spontaneous prostate cancer model. Cab was found to have a transient effect on both tumor and prostate volume in the TRAMP model. However, after end of treatment most tumors and prostates regrew past the starting volume. NP encapsulation or US+MB treatment did not improve treatment efficacy. Encapsulation in NPs was found to affect the biodistribution of Cab with a prolonged circulation time and an increased uptake of Cab in liver and spleen.

Discussion

My research group has studied drug delivery with NPs and US for several years in collaboration with SINTEF, other groups at NTNU and other universities. A wide range of in vitro models have been used in addition to in vivo models like immunodeficient mice with xenografts. In general, it is easier to control experiment parameters when using in vitro models and therefore they are often used to model specific steps of the drug delivery process like interactions between NPs and blood or NPs and cancer cells. To recapitulate all the steps of drug delivery, from intravenous drug or NP administration to the target cancer cell, in vivo models are needed. The validity of in vivo models will vary depending on how representative the disease in the mouse is compared to the disease in humans. The main contribution of this thesis is to demonstrate the use of a spontaneous prostate cancer model to study the efficacy of NP and US+MB drug delivery. Compared to the xenografted models used earlier, this introduces more randomness and less control, but might be more representative of human disease.

Paper 1 was the first paper published from the group using the SINTEF PACA polymeric NPs^{32,48} and was conducted in a period when the group focused on drug delivery assessed with microscopy. Fluorescent dyes were used as a model drug to detect where NPs would deliver their content. Paper 1 demonstrated that US could improve drug uptake and distribution in solid tumors in immunodeficient mice, especially in the periphery of the tumor, where the PC3 tumors had more vasculature. Subsequent studies in the group assessed the effect of NP and US+MB drug delivery on therapeutic efficacy by following tumor volume in xenografted tumors¹⁷. With my PhD work we wanted to move to spontaneous models in immunocompetent mice, which were viewed as more representative of human disease. This led to a collaboration with the MR cancer group combining their expertise on the TRAMP model and prostate imaging with our drug delivery platforms, leading to paper 2 and 3. Paper 2 suggests ways US and MR imaging can be used to alleviate some of the challenging aspects of working with the TRAMP model. Based on imaging, the mice can be stratified into treatment groups depending on phenotype and disease burden can be followed longitudinally. These measures can reduce the inherent variation in the TRAMP model and reduce numbers of mice needed for

statistically significant results in studies. In paper 3, Cab was shown to be effective in reducing PD tumor volume and prostate volume in TRAMP mice. One mouse with a PD tumor receiving Cab combined with US+MB stayed in remission during several weeks of follow up. However, the numbers of mice in the study was low and most tumors started growing within weeks after end of treatment. In mice with dysplastic prostates the volume was reduced by Cab during treatment, but NP encapsulation of Cab or combination with US+MB did not reduce the prostate volume more than Cab alone, even if NP encapsulation increased circulation time and the amount of Cab in the prostate.

NP accumulation in cancerous tissues is dependent on the EPR effect, which is highly variable between tumor types and within tumors themselves. The EPR effect is dependent on factors like blood perfusion, vasculature and the ECM surrounding the vasculature. The EPR effect has been described in many xenograft models, including PC3 xenografts used in paper 1. NP increased drug delivery of Cab in the dysplastic TRAMP prostate, but not the therapeutic efficacy. Compared to most xenografted tumors the dysplastic prostates shows highly differentiated structures, lacking necrotic areas and recruitment of larger blood vessels. Thus, the TRAMP prostate does not display many of the characteristics from tumors displaying high EPR. The PD tumor phenotype of the TRAMP model is more similar to xenografted models because it can exhibit both necrosis and obvious neoangiogenesis. All TRAMP mice receiving NP treatment suffered from transient apnea and bradycardia, which has not occurred in previous studies with Balb/c nude mice. During pilot experiments with NPs stabilizing MBs in the TRAMP, the mice also developed acute respiratory problems with mortality rate up to 50%. Further investigations are needed to discover why the TRAMP model is prone to respiratory problems from NPs and NPs stabilizing MBs.

US+MB treatment is thought to increase drug delivery by increasing permeability of blood vessels and affecting perfusion in tumors. On the cellular level, there are many suggestions for mechanisms involved and studies indicate that drug transport happens both via transient pores in cell membranes, endocytosis, transcytosis and/or exocytosis, opening of intracellular tight junctions and changes in perfusion and the perivascular space^{24,26}. The transport mechanisms respond differently to either heating, acoustic radiation force, stable and inertial cavitation, and optimal settings for one transport

mechanism might not facilitate uptake with another. It is not clear which tissue characteristics which predict a good response to US+MB, but Theek et al. showed that US+MB increased the uptake of liposomal NPs to a large degree in a xenografted tumor with a low degree of EPR effect⁴⁹. The PD tumors of the TRAMP shares some characteristics with xenografted tumors and both display angiogenesis and development of necrotic areas. Further studies of US+MB effects in the TRAMP model is needed to assess treatment efficacy, as we did not breed enough TRAMP mice with PD tumors for paper 3. TRAMP mice with dysplastic prostates did not show any extra effect from combining US+MB with Cab. This might result from unfavorable properties of the prostate microenvironment or that a sufficient amount of Cab was already delivered to the prostate.

Even though the TRAMP model is closer to human cancer than xenografted models in some regards, like heterogenous tumor genetics, orthotopic placement of cancer and an intact immune system, the translation is not straight forward. Grabowska et al. argue that a representative prostate cancer model should recapitulate several features of human prostate cancer⁵⁰: The cancer cells should evolve from epithelial cells and develop through a premalignant lesion before becoming adenocarcinoma. The model should then respond to androgen deprivation therapy, before becoming castration resistant and progress. In addition, it should metastasize, ideally to bone. We used C57BL6 mice as the background strain for TRAMP, where around 20% of mice develop PD tumors⁵¹. The majority of the mice does not develop defined tumors but develop an enlarged prostate with dysplastic glands. There is controversy regarding the malignant potential of the dysplastic epithelial lesions and some argue that they do not represent premalignant lesions⁵², while others argue that they will develop into cancer eventually^{36,40}. This makes translation to human disease challenging. Chiaverotti et al. argue that the PD tumors of the TRAMP develop directly from pluripotent stem cells and not from epithelial cells undergoing malignant transformation⁵². In addition, the PD tumors are positive for neuroendocrine markers. In men, neuroendocrine prostate tumors constitute <1% of primary prostate tumors and predicts a poor prognosis, in addition some adenocarcinomas differentiate to a neuroendocrine phenotype at a late stage when the cancer becomes castration resistant⁵³. Thus, TRAMP PD neuroendocrine tumors might

be a more representative for the subgroup who present or develop neuroendocrine prostate cancer. The dysplastic TRAMP prostate is more difficult to compare to human disease, since it has been classified as both malignant, premalignant and benign by different researchers.

Outlook

Polymeric NPs based on poly(alkyl cyanoacrylate) (PACA) have been extensively investigated because of ease of fabrication, high drug loading capacity and controllable degradation^{54,55}. The SINTEF developed PACA NP platform used in this thesis has been used in pre-clinical research both as a drug carrier and to stabilize MBs for enhanced sonopermeation. Polymer based NPs have so far not been approved for clinical use, but some clinical trials have been done. The most promising polymeric NP so far was the doxorubicin transdrug developed by Onxeo for treatment of hepatocellular carcinoma. However, a phase III clinical trial completed in 2019 assessing the effect of doxorubicin transdrug in patients in whom first line treatment had failed, concluded that doxorubicin transdrug did not improve overall survival compared to standard care⁵⁶. In the fall of 2019 nine NP drugs for cancer treatment were approved by the FDA or EMA⁷. Seven of the drugs were liposomal NPs with or without surface modification with polyethylene glycol, one drug was albumin bound (nano albumin bound-paclitaxel) and the last hafnium-oxide particles for combination with radiotherapy. The future of NPs in cancer treatment is promising, with close to 40 different NPs in clinical cancer trials as of the fall of 2019. The NPs that have reached the clinic have been better than free drug formulations either by reduced toxicity or improved efficacy. A deeper understanding of in vivo NP behavior and how it interacts with tumor tissue could help discover new NPs and find indications for existing NPs. If the SINTEF NPs are to be successful in the future, they will need to fill a niche where it improves treatment outcomes for patients. Toxicity is also an area where more work needs to be done for the NPs.

US+MB is not standard care in the clinic, but there have been and are some clinical trials in humans. One of the most successful clinical trials was conducted in patients with unresectable pancreatic duct adenocarcinoma with a diagnostic US scanner and the commercially available US contrast agent SonoVue given after injection of the chemotherapeutic agent gemcitabine⁵⁷. Compared to historic controls the toxicity was the same and patients tolerated an increased number of gemcitabine cycles. Several studies are ongoing to assess the effect of US+MB combined with chemotherapy or monoclonal antibodies on either pancreatic cancer (ClinicalTrials.gov identifier NCT04146441); liver

metastasis from colorectal, pancreatic or breast cancer (ClinicalTrials.gov identifier NCT02233205, NCT03458975 and NCT03477019) and brain metastasis from malignant melanoma (ClinicalTrials.gov identifier NCT04021420).

US+MB drug delivery have some inherent challenges by being dependent on blood vessel distribution and MB concentration and distribution, making the treatment heterogenous. Some papers have also reported US+MB treatment reducing the effect of some therapies⁵⁸. This emphasize the need for finding the correct applications for US+MB therapy. Because of the heterogeneity of the treatment, it is hard to quantify the ‘dose’ of US+MB treatment. An effort is being made to quantify the effects of US+MB treatment based on detecting the reflected US signal and interpreting bubble behavior⁵⁹. This development could help make US+MB treatment more standardized and make it easier for researchers to compare results. With further research to understand the mechanisms behind US+MB drug delivery to tumors, US+MB treatments can be optimized, and methods can be developed to identify the patients who will benefit from the treatment.

The main novelty of this thesis is the application of NP and US+MB drug delivery in a spontaneous orthotopic prostate cancer model. Even if the thesis failed to prove increased therapeutic efficacy from NP and US+MB drug delivery, we have demonstrated methodology to improve studies in spontaneous cancer models using in vivo imaging. In addition to the practical challenges, the TRAMP model has challenges related to translation, since it is not straight forward which part of human disease it represents. A deeper understanding of the interactions between NPs and tumors and US+MB and tumors is needed to optimize the treatments and to select the patients who will benefit most from the treatments.

References

1. WHO. Cancer key facts. 2018.
2. Ferlay J, Colombet M, Soerjomataram I, et al. Cancer incidence and mortality patterns in Europe: Estimates for 40 countries and 25 major cancers in 2018. *European journal of cancer (Oxford, England : 1990)*. 2018;103:356-387.
3. Mottet N, Bellmunt J, Bolla M, et al. EAU-ESTRO-SIOG Guidelines on Prostate Cancer. Part 1: Screening, Diagnosis, and Local Treatment with Curative Intent. *European urology*. 2017;71(4):618-629.
4. Cornford P, Bellmunt J, Bolla M, et al. EAU-ESTRO-SIOG Guidelines on Prostate Cancer. Part II: Treatment of Relapsing, Metastatic, and Castration-Resistant Prostate Cancer. *European urology*. 2017;71(4):630-642.
5. Barenholz Y. Doxil(R)--the first FDA-approved nano-drug: lessons learned. *Journal of controlled release : official journal of the Controlled Release Society*. 2012;160(2):117-134.
6. Anselmo AC, Mitragotri S. Nanoparticles in the clinic. *Bioengineering & translational medicine*. 2016;1(1):10-29.
7. Anselmo AC, Mitragotri S. Nanoparticles in the clinic: An update. *Bioengineering & translational medicine*. 2019;4(3):e10143.
8. Fang J, Nakamura H, Maeda H. The EPR effect: Unique features of tumor blood vessels for drug delivery, factors involved, and limitations and augmentation of the effect. *Advanced drug delivery reviews*. 2011;63(3):136-151.
9. Matsumura Y, Maeda H. A new concept for macromolecular therapeutics in cancer chemotherapy: mechanism of tumoritropic accumulation of proteins and the antitumor agent smancs. *Cancer research*. 1986;46(12 Pt 1):6387-6392.

10. Eggen S, Fagerland SM, Morch Y, et al. Ultrasound-enhanced drug delivery in prostate cancer xenografts by nanoparticles stabilizing microbubbles. *Journal of controlled release : official journal of the Controlled Release Society*. 2014;187:39-49.
11. Yuan F, Leunig M, Huang SK, Berk DA, Papahadjopoulos D, Jain RK. Microvascular permeability and interstitial penetration of sterically stabilized (stealth) liposomes in a human tumor xenograft. *Cancer research*. 1994;54(13):3352-3356.
12. Tenzer S, Docter D, Kuharev J, et al. Rapid formation of plasma protein corona critically affects nanoparticle pathophysiology. *Nature nanotechnology*. 2013;8(10):772-781.
13. Bertrand N, Grenier P, Mahmoudi M, et al. Mechanistic understanding of in vivo protein corona formation on polymeric nanoparticles and impact on pharmacokinetics. *Nature communications*. 2017;8(1):777.
14. Gunawan C, Lim M, Marquis CP, Amal R. Nanoparticle–protein corona complexes govern the biological fates and functions of nanoparticles. *Journal of Materials Chemistry B*. 2014;2(15):2060-2083.
15. Harris JM, Chess RB. Effect of pegylation on pharmaceuticals. *Nature reviews Drug discovery*. 2003;2(3):214-221.
16. Fusser M, Overbye A, Pandya AD, et al. Cabazitaxel-loaded Poly(2-ethylbutyl cyanoacrylate) nanoparticles improve treatment efficacy in a patient derived breast cancer xenograft. *Journal of controlled release : official journal of the Controlled Release Society*. 2019;293:183-192.
17. Snipstad S, Berg S, Morch Y, et al. Ultrasound Improves the Delivery and Therapeutic Effect of Nanoparticle-Stabilized Microbubbles in Breast Cancer Xenografts. *Ultrasound in medicine & biology*. 2017;43(11):2651-2669.
18. Alexis F, Pridgen E, Molnar LK, Farokhzad OC. Factors affecting the clearance and biodistribution of polymeric nanoparticles. *Molecular pharmaceutics*. 2008;5(4):505-515.

19. Wilhelm S, Tavares AJ, Dai Q, et al. Analysis of nanoparticle delivery to tumours. *Nature Reviews Materials*. 2016;1(5):16014.
20. Boucher Y, Baxter LT, Jain RK. Interstitial pressure gradients in tissue-isolated and subcutaneous tumors: implications for therapy. *Cancer research*. 1990;50(15):4478-4484.
21. Eikenes L, Tari M, Tufto I, Bruland OS, de Lange Davies C. Hyaluronidase induces a transcapillary pressure gradient and improves the distribution and uptake of liposomal doxorubicin (Caelyx) in human osteosarcoma xenografts. *Br J Cancer*. 2005;93(1):81-88.
22. Kotopoulos S, Delalande A, Popa M, et al. Sonoporation-enhanced chemotherapy significantly reduces primary tumour burden in an orthotopic pancreatic cancer xenograft. *Molecular imaging and biology*. 2014;16(1):53-62.
23. Lammertink BH, Bos C, Deckers R, Storm G, Moonen CT, Escoffre JM. Sonochemotherapy: from bench to bedside. *Frontiers in pharmacology*. 2015;6:138.
24. Snipstad S, Sulheim E, de Lange Davies C, et al. Sonopermeation to improve drug delivery to tumors: from fundamental understanding to clinical translation. *Expert opinion on drug delivery*. 2018;15(12):1249-1261.
25. Burke CW, Alexander Et, Timbie K, Kilbanov AL, Price RJ. Ultrasound-activated agents comprised of 5FU-bearing nanoparticles bonded to microbubbles inhibit solid tumor growth and improve survival. *Molecular therapy : the journal of the American Society of Gene Therapy*. 2014;22(2):321-328.
26. Lentacker I, De Cock I, Deckers R, De Smedt SC, Moonen CT. Understanding ultrasound induced sonoporation: definitions and underlying mechanisms. *Advanced drug delivery reviews*. 2014;72:49-64.
27. Sarvazyan AP, Rudenko OV, Nyborg WL. Biomedical applications of radiation force of ultrasound: historical roots and physical basis. *Ultrasound in medicine & biology*. 2010;36(9):1379-1394.

28. Frenkel V. Ultrasound mediated delivery of drugs and genes to solid tumors. *Advanced drug delivery reviews*. 2008;60(10):1193-1208.
29. Dick EA, Gedroyc WMW. ExAblate® magnetic resonance-guided focused ultrasound system in multiple body applications. *Expert Review of Medical Devices*. 2010;7(5):589-597.
30. Ferrara K, Pollard R, Borden M. Ultrasound microbubble contrast agents: fundamentals and application to gene and drug delivery. *Annual review of biomedical engineering*. 2007;9:415-447.
31. Kooiman K, Vos HJ, Versluis M, de Jong N. Acoustic behavior of microbubbles and implications for drug delivery. *Advanced drug delivery reviews*. 2014;72:28-48.
32. Morch Y, Hansen R, Berg S, et al. Nanoparticle-stabilized microbubbles for multimodal imaging and drug delivery. *Contrast Media Mol Imaging*. 2015;10(5):356-366.
33. Gengenbacher N, Singhal M, Augustin HG. Preclinical mouse solid tumour models: status quo, challenges and perspectives. *Nature reviews Cancer*. 2017;17(12):751-765.
34. Gingrich JR, Barrios RJ, Morton RA, et al. Metastatic prostate cancer in a transgenic mouse. *Cancer research*. 1996;56(18):4096-4102.
35. Greenberg NM, DeMayo F, Finegold MJ, et al. Prostate cancer in a transgenic mouse. *Proceedings of the National Academy of Sciences of the United States of America*. 1995;92(8):3439-3443.
36. Berman-Booty LD, Sargeant AM, Rosol TJ, et al. A review of the existing grading schemes and a proposal for a modified grading scheme for prostatic lesions in TRAMP mice. *Toxicologic pathology*. 2012;40(1):5-17.
37. Gelman IH. How the TRAMP Model Revolutionized the Study of Prostate Cancer Progression. *Cancer research*. 2016;76(21):6137.

38. Kido LA, de Almeida Lamas C, Marostica MR, Jr., Cagnon VHA. Transgenic Adenocarcinoma of the Mouse Prostate (TRAMP) model: A good alternative to study PCa progression and chemoprevention approaches. *Life sciences*. 2019;217:141-147.
39. Gingrich JR, Barrios RJ, Foster BA, Greenberg NM. Pathologic progression of autochthonous prostate cancer in the TRAMP model. *Prostate cancer and prostatic diseases*. 1999;2(2):70-75.
40. Kaplan-Lefko PJ, Chen TM, Ittmann MM, et al. Pathobiology of autochthonous prostate cancer in a pre-clinical transgenic mouse model. *The Prostate*. 2003;55(3):219-237.
41. Liu Y, Wu X, Jiang H. Combined maternal and post-weaning high fat diet inhibits male offspring's prostate cancer tumorigenesis in transgenic adenocarcinoma of mouse prostate model. *The Prostate*. 2019;79(5):544-553.
42. Raina K, Rajamanickam S, Singh RP, Deep G, Chittezhath M, Agarwal R. Stage-specific inhibitory effects and associated mechanisms of silibinin on tumor progression and metastasis in transgenic adenocarcinoma of the mouse prostate model. *Cancer research*. 2008;68(16):6822-6830.
43. Wang L, Bonorden MJ, Li GX, et al. Methyl-selenium compounds inhibit prostate carcinogenesis in the transgenic adenocarcinoma of mouse prostate model with survival benefit. *Cancer prevention research (Philadelphia, Pa)*. 2009;2(5):484-495.
44. Silva RS, Kido LA, Montico F, Vendramini-Costa DB, Pilli RA, Cagnon VHA. Steroidal hormone and morphological responses in the prostate anterior lobe in different cancer grades after Celecoxib and Goniotalamin treatments in TRAMP mice. *Cell biology international*. 2018;42(8):1006-1020.
45. da Silva RF, Banzato TP, Alves LF, Carvalho JE, Agarwal R, Cagnon VHA. Antiangiogenic therapy with Nintedanib affects hypoxia, angiogenesis and apoptosis in the ventral prostate of TRAMP animals. *Cell and tissue research*. 2019.
46. Sogaard CK, Moestue SA, Rye MB, et al. APIM-peptide targeting PCNA improves the efficacy of docetaxel treatment in the TRAMP mouse model of prostate cancer. *Oncotarget*. 2018;9(14):11752-11766.

47. Degrassi A, Russo M, Scanziani E, et al. Magnetic resonance imaging and histopathological characterization of prostate tumors in TRAMP mice as model for pre-clinical trials. *The Prostate*. 2007;67(4):396-404.
48. Aslund AKO, Sulheim E, Snipstad S, et al. Quantification and Qualitative Effects of Different PEGylations on Poly(butyl cyanoacrylate) Nanoparticles. *Molecular pharmaceutics*. 2017;14(8):2560-2569.
49. Theek B, Baues M, Ojha T, et al. Sonoporation enhances liposome accumulation and penetration in tumors with low EPR. *Journal of controlled release : official journal of the Controlled Release Society*. 2016;231:77-85.
50. Grabowska MM, DeGraff DJ, Yu X, et al. Mouse models of prostate cancer: picking the best model for the question. *Cancer metastasis reviews*. 2014;33(2-3):377-397.
51. Fagerland ST, Hill DK, van Wamel A, de Lange Davies C, Kim J. Ultrasound and magnetic resonance imaging for group stratification and treatment monitoring in the transgenic adenocarcinoma of the mouse prostate model. *The Prostate*. 2019.
52. Chiaverotti T, Couto SS, Donjacour A, et al. Dissociation of epithelial and neuroendocrine carcinoma lineages in the transgenic adenocarcinoma of mouse prostate model of prostate cancer. *The American journal of pathology*. 2008;172(1):236-246.
53. Sun Y, Niu J, Huang J. Neuroendocrine differentiation in prostate cancer. *American journal of translational research*. 2009;1(2):148-162.
54. Kumari A, Yadav SK, Yadav SC. Biodegradable polymeric nanoparticles based drug delivery systems. *Colloids and surfaces B, Biointerfaces*. 2010;75(1):1-18.
55. Vauthier C, Dubernet C, Fattal E, Pinto-Alphandary H, Couvreur P. Poly(alkylcyanoacrylates) as biodegradable materials for biomedical applications. *Advanced drug delivery reviews*. 2003;55(4):519-548.
56. Merle P, Blanc JF, Phelip JM, et al. Doxorubicin-loaded nanoparticles for patients with advanced hepatocellular carcinoma after sorafenib treatment failure (RELIVE): a

phase 3 randomised controlled trial. *The lancet Gastroenterology & hepatology*. 2019;4(6):454-465.

57. Dimcevski G, Kotopoulis S, Bjanec T, et al. A human clinical trial using ultrasound and microbubbles to enhance gemcitabine treatment of inoperable pancreatic cancer. *Journal of controlled release : official journal of the Controlled Release Society*. 2016;243:172-181.

58. van Wamel A, Sontum PC, Healey A, et al. Acoustic Cluster Therapy (ACT) enhances the therapeutic efficacy of paclitaxel and Abraxane(R) for treatment of human prostate adenocarcinoma in mice. *Journal of controlled release : official journal of the Controlled Release Society*. 2016;236:15-21.

59. Sun T, Zhang Y, Power C, et al. Closed-loop control of targeted ultrasound drug delivery across the blood-brain/tumor barriers in a rat glioma model. *Proceedings of the National Academy of Sciences of the United States of America*. 2017;114(48):E10281-e10290.

Paper I



Ultrasound-enhanced drug delivery in prostate cancer xenografts by nanoparticles stabilizing microbubbles

Siv Eggen ^{a,*}, Stein-Martin Fagerland ^a, Ýrr Mørch ^b, Rune Hansen ^{c,f}, Kishia Søvik ^a, Sigrd Berg ^c, Håkon Furu ^a, Audun Dybvik Bøhn ^a, Magnus B. Lilledahl ^a, Anders Angelsen ^{d,e}, Bjørn Angelsen ^f, Catharina de Lange Davies ^a

^a Department of Physics, Norwegian University of Science and Technology, Trondheim, Norway

^b SINTEF Materials and Chemistry, Dept. of Polymer Particles and Surface Chemistry, Trondheim, Norway

^c SINTEF Technology and Society, Dept. of Medical Technology, Trondheim, Norway

^d Department of Cancer Research and Molecular Medicine, Norwegian University of Science and Technology, Trondheim, Norway

^e Department of Urological Surgery, St. Olavs Hospital, Trondheim University Hospital, Norway

^f Department of Circulation and Diagnostic Imaging, Norwegian University of Science and Technology, Trondheim, Norway

ARTICLE INFO

Article history:

Received 24 February 2014

Accepted 9 May 2014

Available online 20 May 2014

Keywords:

Ultrasound

Drug delivery

Solid tumor

Nanoparticles

Microbubbles

Microdistribution

ABSTRACT

The delivery of nanoparticles to solid tumors is often ineffective due to the lack of specificity towards tumor tissue, limited transportation of the nanoparticles across the vascular wall and poor penetration through the extracellular matrix of the tumor. Ultrasound is a promising tool that can potentially improve several of the transportation steps, and the interaction between sound waves and microbubbles generates biological effects that can be beneficial for the successful delivery of nanocarriers and their contents. In this study, a novel platform consisting of nanoparticle-stabilized microbubbles has been investigated for its potential for ultrasound-enhanced delivery to tumor xenografts. Confocal laser scanning microscopy was used to study the supply of nanoparticles from the vasculature and to evaluate the effect of different ultrasound parameters at a microscopic level. The results demonstrated that although the delivery is heterogeneous within tumors, there is a significant improvement in the delivery and the microscopic distribution of both nanoparticles and a released model drug when the nanoparticles are combined with microbubbles and ultrasound. The mechanisms that underlie the improved delivery are discussed.

© 2014 Elsevier B.V. All rights reserved.

1. Introduction

Nanotechnology has brought about a new era of engineering multifunctional nanoparticles (NPs) for improved cancer diagnosis and therapy, incorporating both contrast agents for imaging and drugs for therapy. The rationale for using NPs for drug delivery is to improve the pharmacokinetics of cytotoxic drugs by aiming for the specific accumulation in tumor tissue and reducing the toxic effects towards healthy tissue. Circulating NPs may passively accumulate in solid tumors due to fenestrations in the tumor capillaries and a lack of functional lymphatics, a phenomenon that is known as the enhanced permeability and retention (EPR) effect [1,2]. Several different types of nanocarriers have been developed for delivering their payload to tumor cells including liposomes [3], polymeric micelles [4], virus particles [5], conjugates of polymer-drug [6] or lipid-drug [7] and polymeric NPs [8]. Despite the extensive research in this field and the number of particle formulations being developed, only a few pharmacological products have received FDA approval and are ready for use in the clinic [9].

A common feature among nanocarrier systems is that the particles encounter several barriers on their journey to the disease site. To obtain sufficient tumor accumulation, the NPs need to remain in the circulation for a sufficiently long time. This implies that the particles need to escape phagocytosis by the mononuclear phagocyte system (MPS). A common approach to avoid this is to coat the surface of the NPs with poly(ethylene glycol) (PEG) [10,11]. Nonetheless, to reach the cancer cells, the particles need to leave the circulation and enter the extracellular matrix (ECM) of the tumor. This is possible due to the EPR effect, although the hyperpermeability is heterogeneous [12, 13]. Furthermore, the high interstitial fluid pressure (IFP) in a tumor [1,14,15] reduces convection-mediated transport of NPs across the capillary wall and throughout the ECM, and hence only a small population of cancer cells located close to blood vessels is exposed to the particles and their cargo [16,17].

Several strategies to improve the therapeutic effect, by improving the delivery and accumulation of NPs to cancer tissue, are being explored. The use of therapeutic ultrasound (US) has received great interest during the past two decades. US is non-invasive and can be focused on an area of interest in the body without affecting the surrounding tissue. US has been shown to enhance the delivery of NPs [18–20], drugs encapsulated in the shell of microbubbles (MBs) [21] and drugs co-

* Corresponding author. Tel.: +47 73593465.

E-mail address: siv.eggen@ntnu.no (S. Eggen).

injected with MBs [22]. Furthermore, in a clinical study of patients with pancreatic tumors, combining US and the co-injection of gemcitabine and MBs revealed promising results [23].

The effects of therapeutic US can roughly be divided into thermal and non-thermal effects. The induction of hyperthermia has been reported to increase blood flow and enhance the permeability of the tumor vasculature [24,25] and to release the contents of thermosensitive nanocarriers. Non-thermal effects, also known as mechanical effects, include acoustic radiation forces and acoustic cavitation. The acoustic radiation force is the transfer of momentum from the propagating US beam to the tissue in the sonicated field, which may induce the translation of objects in the tissue in the same direction as the US beam [26]. Acoustic cavitation is the formation, growth, oscillation and collapse of gas bubbles under the influence of US waves. Stable cavitation is characterized by repetitive, non-collapse oscillations of gas bubbles, which can generate local streaming, shear stresses on nearby objects and increase the permeability of blood vessels [27]. Inertial cavitation occurs when bubble growth during the rarefactional phase of an US wave becomes large enough to cause the bubble to collapse violently during the compression phase of the wave, potentially inducing jet streams, shock waves and temperature elevations [28].

Gas bubbles with a size of 1–10 μm can be administered intravenously to improve the backscattered signal from blood in US diagnostic imaging. In addition, artificially introduced MBs act as cavitation nuclei and will significantly reduce the threshold for obtaining *in vivo* cavitation. In this study, we have combined US and a novel particle platform consisting of MBs stabilized by polymeric NPs to improve the delivery of a hydrophobic model drug to tumor xenografts growing in mice. The polymeric NPs consist of poly(butylcyanoacrylate) (PBCA), which is biodegradable and biocompatible and can be functionalized with PEG and conjugated with bioactive molecules for targeting [29]. Furthermore, the size of both the NPs and the MBs can be tailored, and different drugs and contrast agents can be encapsulated in the NPs [30]. The integration of NPs surrounding a gas bubble makes this a promising agent both for US contrast enhanced imaging and for US-mediated drug delivery (Fig. 1). The NP synthesis involves only a one-step miniemulsion polymerization followed by high-speed mixing of NPs and air to produce the MBs. In the present study, the hydrophobic fluorescent dye Nile red was chosen due to its unique spectral properties, emitting light at wavelengths that depend on the hydrophobicity of the molecule binding to Nile red [31]. Confocal laser scanning microscopy (CLSM) was used to investigate the effects of different US exposures on the tumor uptake of NPs on a microscopical level, estimating both the extravasation and penetration into the ECM. Optical imaging using a whole animal imaging system was used to investigate the clearance of the NPs from the circulation.

2. Materials and methods

2.1. Synthesis and characterization of nanoparticles and microbubbles

Miniemulsion polymerization was used to prepare PEGylated NPs of the polymer PBCA. Oil-in-water emulsions were prepared by emulsifying (Digital Sonifier®, Branson Ultrasonics, USA) a monomer phase, consisting of butyl-2-cyanoacrylate (BCA; Henkel Loctite, Ireland), a co-stabilizer (Miglyol 810N®, 2 wt.%, Cremer, Germany) and the fluorescent dye Nile red (0.4 wt.%,) or 1,1'-dioctadecyl-3,3,3',3'-tetramethylindotricarbocyanine iodide (DiR; 0.1 wt.%) in an acidic aqueous medium (0.1 M HCl) containing sodium dodecyl sulfate (SDS) as a surfactant. The initiation of the anionic polymerization was performed by adding Jeffamine M-1000® (Huntsman Corporation, Belgium) to the emulsion, resulting in PEGylated NPs [30]. Excess PEG and SDS were removed by extensive dialysis against distilled water using dialysis membranes with a MWCO of 12–14,000. The size and the zeta potential of the NPs were measured by dynamic light scattering in a Zetasizer Nano ZS (Malvern, UK).

Stable air MBs were prepared by self-assembly of the NPs (1 wt.%) at the air–water interface by the addition of bovine serum albumin (BSA) and vigorous stirring using an ultra-turrax (IKA Werke, Germany) as described by Mørch et al. [30]. The average MB diameter could be controlled by varying the stirring speed. The size distribution and concentration of MBs was determined using both a Coulter Counter (Beckman Multisizer 3) and light microscopy. The shelf stability of MBs was studied by light microscopy imaging. The behavior of the MBs during US was investigated using a flow mimicking phantom under different transmit frequencies and 10 transmit oscillations, using a conventional pulse inversion technique.

2.2. Cells and animals

Human PC3 prostate adenocarcinoma cells (American Type Culture Collection, USA) were cultured in Dulbecco's Modified Eagle Medium (Life Technologies Corporation, USA) with 10% fetal bovine serum at 37 °C and 5% CO₂.

Balb/c nude mice (Taconic, Denmark) were purchased at 8 weeks of age and housed in groups of 5 in individually ventilated cages (Tecniplast) at temperatures between 19 and 22 °C and a relative humidity of 50–60%. The housing conditions were free of specific pathogens according to the recommendations set by the Federation of European Laboratory Animal Science Associations [32], and the mice had free access to food and sterile water. All experimental procedures with the animals were conducted in compliance with protocols approved by the Norwegian National Animal Research Authorities.

2.3. Tumor models

The human prostate adenocarcinoma PC3 cells were grown as xenografts in athymic mice either subcutaneously or in dorsal window chambers. Before the inoculation of subcutaneous xenografts, the animals were anesthetized with 2% isoflurane, and a suspension containing 3×10^6 cells was slowly injected subcutaneously on the lateral aspect of one hind leg. The tumors were allowed to grow until they had reached a diameter of 5–10 mm.

Before implantation of dorsal skin-fold window chambers, the mice were anesthetized with 0.15 ml of a solution of fentanyl and fluanisone (Hypnorm® vet, VetaPharma Ltd, UK), midazolam (5 mg/ml; Roche Norge AS, Norway) and sterile water (1:1:2). Two symmetrical plastic frames were attached to an extended dorsal skin fold and a window was made and sealed with a cover slip as previously described [33]. For analgesia, the mice were given a subcutaneous injection of 0.05 mg meloxicam (Boehringer Ingelheim GmbH, Germany) prior to the surgery as well as on the two subsequent days. On the day following the surgery, the cover slip was removed, and a bolus of approximately

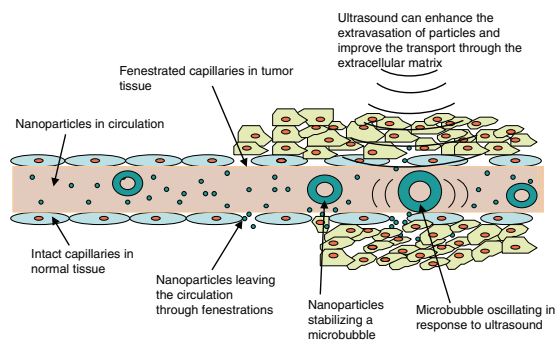


Fig. 1. Illustration of a tumor capillary with circulating nanoparticles and microbubbles stabilized by nanoparticles, exposed to focused ultrasound.

2×10^6 cells was deposited onto the exposed subcutaneous tissue. The area was then sealed with a new cover slip, and the tumors were allowed to grow for 2 weeks. Through the experimental period, the animals' drinking water was supplemented with 20 g sugar and 62.5 mg enrofloxacin (Bayer Animal Health, Germany) per 1000 ml.

2.4. Measurements of circulation half-life

The circulation half-life of PBCA NPs was measured after anesthetizing the mice with the fentanyl/fluanisone and midazolam solution as described above. Before injecting the NPs, a blood sample of approximately 20 μ l was drawn from the saphenous vein and diluted in 40 μ l of 10 IU/ml heparin. After injecting a 200 μ l bolus of PBCA NPs (7 mg/ml) containing the near-infrared dye DiR intravenously into the lateral tail vein, blood samples were drawn from the saphenous vein and diluted in heparin as described above at 10 and 30 min and then at 1, 2, 4, 6 and 24 h post-injection. The fluorescence in the blood samples was measured by imaging 20 μ l of plasma in a Pearl Impulse small-animal imaging system (LI-COR Biosciences, USA). DiR was excited using a 785-nm laser line, fluorescence was detected at 820 nm, and the image resolution was 85 μ m.

2.5. Intravital microscopy of the vasculature and microbubbles

Before intravital microscopy of the tumors in the dorsal window chambers, the mice were anesthetized with 200 μ l of a solution of haloperidol (5 mg/ml, Janssen), midazolam (5 mg/ml, Actavis), fentanyl (50 μ g/ml, Actavis) and water (2:3:3:4) and a 27G venflon was placed in the lateral tail vein. The window chamber was fixed on a custom-made insert and placed on the stage of a CLSM (Leica SP8; Leica Microsystems GmbH, Germany) with the cover slip of the chamber facing towards a $10\times/0.7$ air objective. To visualize blood vessels, approximately 30 μ l of a 20 mg/ml solution of 2 MDa Fluorescein Isothiocyanate-Dextran (FITC-Dextran, Sigma-Aldrich, USA) was injected intravenously. A time series of images was acquired during and after the injection of a 200 μ l bolus of PBCA NPs stabilizing MBs (concentration 10^7 /ml). Each single image in the time series had a dimension of $416 \times 416 \mu\text{m}$ or 1024×1024 pixels, and the acquisition frame was approximately 4 s. The time series continued until 150 images had been acquired or until movement of the chamber.

2.6. Ultrasound setup

The US signals were generated by a waveform generator (Agilent Technologies 33500B, USA), amplified by a power amplifier (ENI 2100L, USA) and monitored by an oscilloscope (LeCroy LT262, USA). The animals were exposed to ultrasound using either one of two custom-made transducers (Imasonic, France) with center frequencies of 300 kHz and 1 MHz, respectively, or using a commercially available Panametric transducer (V308; Olympus Corporation, Japan) with a frequency of 5 MHz. Fig. 2 illustrates the setup using the custom-made transducers (A) and the 5 MHz Panametric transducer (B).

The custom-made transducers have been characterized previously [34]. The circular single element transducers had a diameter of 55 mm for the 300 kHz frequency transducer and 50 mm for the 1 MHz transducer. The distance from the array to the focal area was 69 mm for the 300 kHz transducer and 125 mm for the 1 MHz transducer. The transducers were mounted inside an exposure chamber containing degassed water as illustrated in Fig. 2A, and a lid with a fibrous filter was placed at the surface of the water. The mice were placed on top of the lid, and the tumor-bearing leg was lowered into the water through a 10-mm opening. The transducer was positioned to ensure that the tumor was in the focus of the US beam.

The 5 MHz Panametric transducer was circular, with a diameter of 19 mm, a focal distance of 69 mm and a focal region of 1.6 mm. The transducer array was placed in a centrifuge tube with a 3-mm opening

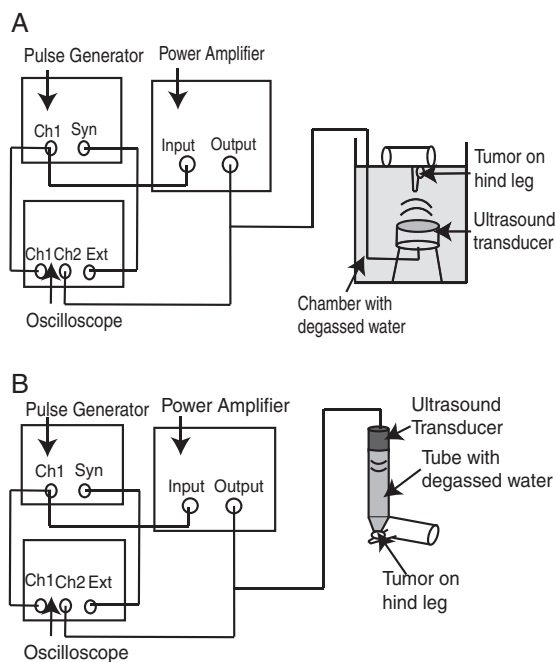


Fig. 2. Schematic illustration of the ultrasound setup. Exposure of the hindlimb xenograft using custom-made transducers of 1 MHz or 300 kHz (A) or the 5-MHz transducer (B).

at the tip, and the length of the tube corresponded to the focal distance. The tube was filled with degassed water and the tip was sealed with a thin plastic film. A rich amount of ultrasound gel (Parker Laboratories, USA) was used as coupling medium between the film on the tube and the skin covering the tumor. Because of the limited focal area, the transducer was scanned across the tumor using a step motor (Superior Electric Company, USA) and a Data Acquisition (DAQ) Pad (National Instruments Corporation, USA) controlled by a custom-made Laboratory Virtual Instrument Engineering Workbench (LabVIEW; National Instruments Corporation, USA) function.

2.7. Investigation of thermal effects

To study whether the chosen US parameters caused any temperature elevations, the US exposures were performed on a piece of *ex vivo* bovine muscle tissue, where the temperature was measured in the tissue using a thermocoupler before and within 5 s after the US exposure. Each US setting was tested three times.

2.8. US exposure when nanoparticles were administered as a solution of microbubbles

The mice were anesthetized with fentanyl/fluanisone and midazolam, and a 200- μ l bolus of MBs (concentration 10^8 /ml) stabilized with NPs containing Nile red was given intravenously through the lateral tail vein, and the tumors were exposed to US within 1 min post-injection. One group of mice ($n = 5$) was exposed to 1 MHz US with a peak negative pressure of 0.15 MPa, corresponding to a mechanical index (MI) of 0.15. The pulse length was 10 oscillations and the pulse repetition frequency (PRF) was 3 kHz, which gives a duty cycle of 3%. The duration of the exposure was 2 min. Another group of mice ($n = 5$) was exposed to 1 MHz US with a peak negative pressure of 0.4 MPa, corresponding to a MI of 0.4. The pulse length, PRF and insonation time were the same as with the 0.15-MI exposure. A third

group ($n = 4$) was given gas bubbles as in the previous groups, but was not exposed to US.

2.9. US exposure when nanoparticles were administered as a solution of particles without microbubbles

The mice were anesthetized with fentanyl/fluanisone and midazolam as described above. A 200- μ l bolus of PBCA NPs (17 mg/ml) containing Nile red was given intravenously through the lateral tail vein. The particles were allowed to circulate for 5 min or 24 h before the tumors were exposed to either 300 kHz or 5 MHz US ($n = 5$ for all groups). The MI applied was higher when no MBs were used. For the 300 kHz exposure, the duty cycle was 5% with a PRF of 250 Hz and a pulse length of 60 cycles. The peak negative pressure was 1.3 MPa corresponding to a MI of 2.4. The total duration of the exposure was 10 min. For the 5 MHz exposure, a pulse length of 10 cycles and a PRF of 1 kHz were used. The peak negative pressure was 1.57 MPa, corresponding to an MI of 0.7. In addition, the exposure generated a positive pressure of 7.1 MPa. The transducer was scanned across the tumor, and each point of the tumor was sonicated for 4 min.

2.10. Labeling of blood vessels and preparation of tumor sections

Post-US, 100 μ l of fluorescein-labeled *Lycopersicon esculentum* (Tomato) lectin (FITC-lectin; Vector Laboratories, USA) diluted in 0.9% NaCl to 1 mg/ml was given intravenously and allowed to circulate for 5 min. The animals were then euthanized, and the tumors were excised, embedded in OTC Tissue Tek (Sakura, The Netherlands) and frozen in liquid N₂. Frozen sections of 25 μ m were prepared from 5 depth levels in the tumor, with 250 μ m between each depth level. The sections were mounted on objective glass slides with Vectashield mounting medium (Vector Laboratories, USA) and sealed with a glass cover slip and nail polish around the edges of the cover slip.

2.11. Staining of frozen sections

The 25 μ m frozen sections were stained for histology using Harris hematoxylin for 8 min followed by erythrosine for 2 min. Subsequently, the sections were dehydrated and mounted using a xylene based medium and a cover slip.

2.12. Confocal laser scanning microscopy of tumor sections

The microscopic distribution of PBCA NPs, released Nile red and blood vessels were imaged using CLSM (Zeiss LSM510, Germany). FITC-labeled blood vessels and Nile red were excited using, respectively, a 488-nm argon laser line and a 543-nm helium/neon laser line. The Nile red emission spectra depend on the hydrophobicity of the molecules bound to the dye. Thus, to distinguish among released Nile red binding to various molecules in the tissue, Nile red in PBCA particles and tissue autofluorescence, the images were acquired in both channel mode and in lambda mode. In lambda mode, the fluorescence was detected at 10-nm intervals from 553 nm to 650 nm. Tile scan images for quantitative assessments of Nile red were obtained using a 20 \times /0.5 air objective, and the tumor sections were imaged along a radial track from periphery to periphery. The co-localization of Nile red and blood vessels was imaged using a 63 \times /1.4 oil immersion objective. Each single image had a resolution of 1024 \times 024 pixels. All images in one study were acquired using the same laser current, transmission, detector gain, amplitude gain and amplitude offset, all of which were chosen to minimize noise and utilize the gray scale.

2.12.1. Second-harmonic generation microscopy of collagen

The distribution of collagen in the tumor tissue was imaged by the second-harmonic generated signal [35] using the Leica SP8 CLSM. A Ti: Sapphire pulsed laser at 800 nm (Chameleon, Coherent Inc., USA) was

used for excitation, and the second-harmonic signal emitted from collagen was detected in forward scattered mode at 390–410 nm. FITC-labeled blood vessels were excited using a 488-nm Argon laser line. Images were acquired using a 25 \times /0.95 water immersion objective. Tile scan images were acquired to obtain an overview of the connective tissue within the tumor. Each single image in the tile scan had a resolution of 512 \times 512 pixels.

2.13. Image post-processing

2.13.1. Pearl Impulse images

Regions of interest (ROIs) were drawn around the blood samples, and the fluorescence intensity, corrected for sample volume, was determined using ImageJ (1.43m, National Institutes of Health, USA), and the Bio-Formats Importer plugin.

2.13.2. Intravital microscopy

Images from time series were imported into ImageJ and built into concatenated stacks. Based on FITC-labeled blood vessels, different ROIs were drawn in areas corresponding to the intravascular space and extravascular areas, respectively. The fluorescence intensity of Nile red as a function of time in each ROI was measured.

2.13.3. Assessment of the number of fluorescent objects and the distance from blood vessels

Single images acquired from peripheral and central regions of the tissue sections from all 5 depth levels were investigated for the number of fluorescent objects and their distance from FITC-labeled blood vessels. Lambda mode images were used to determine, based on the emission spectra, which fluorescent objects corresponded to Nile red in NPs, released Nile red and tissue autofluorescence. The numbers of fluorescent structures that were identified as NPs or released Nile red bound to hydrophobic molecules in the tissue were manually counted, and a line was drawn from Nile red fluorescent structures to their closest FITC-labeled blood vessels.

2.13.4. Quantitative assessment of NPs and released Nile red

The tile scans acquired in lambda mode were unmixed using the linear unmixing function in the software package from Zeiss LSM to separate Nile red in NPs, released Nile red and tissue autofluorescence. To quantify the contribution of Nile red in particles or released Nile red, the unmixed images were analyzed using a custom-made Matlab (Version R2007a; Natick, USA) function that estimated both the area of fluorescence and the mean fluorescence intensity along the tile scan images. To eliminate background and maintain the specific fluorescence signal, a threshold was manually set to 56.1 of 256 gray levels. The tumor uptake of Nile red in NPs or released Nile red was quantified by calculating the total fluorescence as the area of fluorescence multiplied by the mean intensity.

2.14. Statistical analysis

Data were imported into worksheets of Statistical Package for the Social Sciences (SPSS; IBM, USA) for statistical analyses. The data were not found to be Gaussian distributed; thus, to test for significant differences across groups, Kruskal Wallis tests were conducted. Where applicable, groups were compared pairwise using Mann–Whitney U tests. A p-value below 0.05 was considered significant. The effect size (r) was calculated by dividing the z-value from the Mann–Whitney U test by the square root of the total number of observations. The data are presented in box plots where the horizontal line represents the median observation, the box represents 50% of the measurements, and the lines protruding from the box represent the lower and upper range, respectively. Extreme observations are indicated by symbols, where circles and asterisks are observations that extend more than 1.5 and 3 box-lengths from the edge of the box, respectively.

3. Results

3.1. Characterization of the nanoparticles and microbubbles

Dynamic light scattering using the Zetasizer determined the average hydrodynamic diameter of the NPs to be 120–190 nm and the polydispersity index (PDI) = 0.1. The zeta potential was -30 to -20 mV at pH 7. The size distribution of the MBs was rather broad (Fig. 3A), and ranged from 1 to 10 μm . Measurements done by Coulter Counter also revealed aggregates of NPs in the size range of 0.5 to 1 μm (data not shown). The CLSM image (Fig. 3B) illustrates that the fluorescently labeled NPs formed a shell around the MBs. Light microscopy imaging of the MBs 8 months after their production gave similar images as Fig. 3A, demonstrating a shelf stability for more than 8 months. In a tissue mimicking flow phantom, moderate MB destruction was observed at a MI of 0.15, and complete MB destruction occurred at a MI of 0.4.

3.2. Circulation half-life of nanoparticles

The circulation half-life of the NPs was determined by analyzing the fluorescence in blood samples taken at different time points from the same animals. Fig. 4 presents a typical image of fluorescence in the blood samples (A) and the relative change in fluorescence intensity as a function of time (B).

The fluorescence intensity exhibited a biphasic response, indicating that a two-compartment distribution is the best model to describe the kinetics of the NPs in the blood. There was a rapid decline in the plasma fluorescence during the first hours post-administration, indicating that the particles were eliminated rather quickly from the circulation. The data were fitted to a bi-exponential decay function (Eq. (1)) with a rapid and a slow decay rate of, respectively, 0.52 h^{-1} and 315 h^{-1} . The rapid decay rate corresponds to a circulation half-life of 1.3 h.

$$f(t) = 142e^{(-0.52t)} - 141e^{(-315.38t)} \quad (1)$$

3.3. Intravital microscopy of nanoparticle-stabilized microbubbles

Intravascular microscopy is a unique tool to investigate the dynamics of the behavior of NPs in the vasculature as well as the extravasation and accumulation in the ECM [36]. Tumor tissue with fluorescently labeled blood vessels was imaged during and after i.v. injection of NP-stabilizing MBs (Fig. 5). Panels A, B, C and D represent 4 different tumors and the NPs, shown as white dots, behaved differently in the various tumors. The images were selected to illustrate the heterogeneity in tumor blood vessel morphology as well as the permeability and extravasation of administered nanoparticles. The tumors shown in panels A–D have capillaries with varying diameters. However, the extent of extravasation seemed to vary independently of the capillary diameter. Furthermore, within the same tumor, the vascular permeability and the ability of

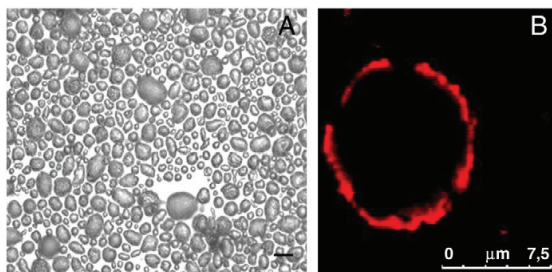


Fig. 3. A) Light microscopy image of a solution of microbubbles (scale bar = 10 μm). B) Confocal laser scanning image of one microbubble stabilized by polymeric nanoparticles (scale bar = 7.5 μm).

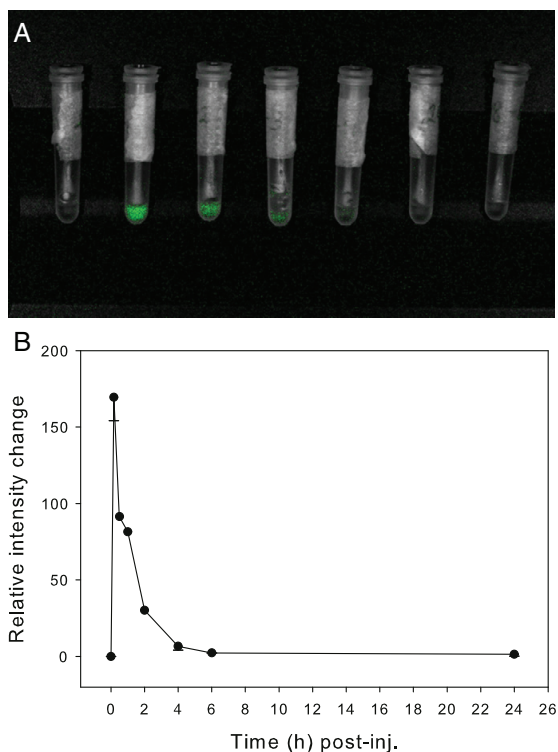


Fig. 4. A) Blood samples taken from mice before the injection of nanoparticles and then 10 min, 30 min, 1 h, 2 h, 4 h and 6 h post-injection. The nanoparticles were labeled with the infrared dye DiR. B) Change in plasma DiR fluorescence as a function of time post-injection.

NPs to extravasate differed to a large extent. The vessels in A and B exhibited low permeability and the NPs were mainly localized in the vasculature. In panels C and D, a substantial amount of extravasated NPs was observed 50 s after injection. However, both NPs that were confined to the vasculature as well as NPs that extravasated were rapidly eliminated. To obtain a more quantitative description of the dynamic behavior of NPs, the Nile red fluorescence intensity was measured in ROIs inside and outside the vasculature (Fig. 5E).

3.4. Temperature measurements

The US exposures using the 300 kHz and the 1 MHz transducers did not cause any temperature increase. For the exposure using the 300 kHz transducer, the temperature decreased from an average of 18.0 $^{\circ}\text{C}$ before the exposure to 16.8 $^{\circ}\text{C}$ immediately after the sonication. The 1 MHz exposure with an MI of 0.15 or 0.4 caused a temperature decrease from an average of 18.5 $^{\circ}\text{C}$ to 17.7 $^{\circ}\text{C}$ or from an average of 18.3 $^{\circ}\text{C}$ to 17.9 $^{\circ}\text{C}$, respectively. The 5 MHz exposure resulted in a minor temperature increase from an average of 18.1 $^{\circ}\text{C}$ to 18.5 $^{\circ}\text{C}$.

3.5. Spectral analysis of Nile red

The spectral properties of Nile red depend on what molecules the dye binds to [31]. Being a hydrophobic dye, Nile red tends to bind to lipophilic components. The emission spectrum of Nile red is shifted towards lower wavelengths when bound to lipids, compared with Nile red bound to less hydrophobic molecules or Nile red in NPs. The emission spectra make it therefore possible to distinguish between Nile red

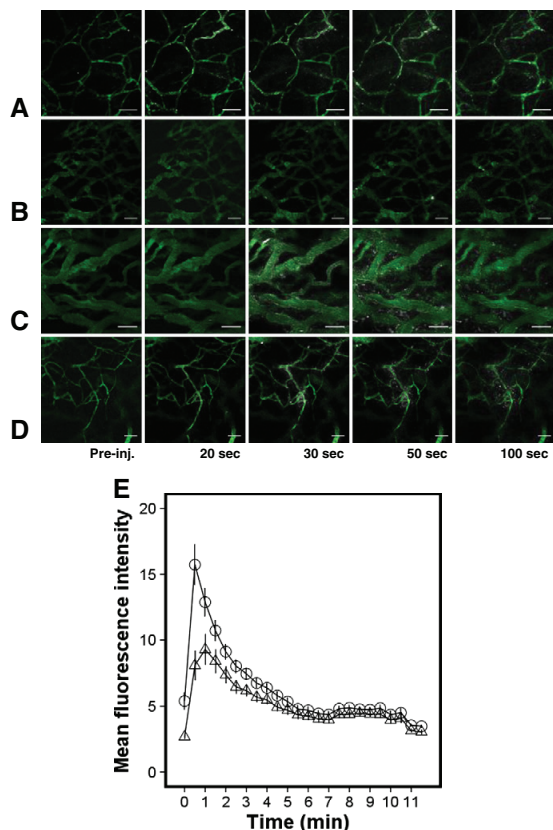


Fig. 5. A–D) CLSM images from four different tumors in window chambers at different time points post-injection of nanoparticle-stabilized microbubbles. The images show FITC-dextran-labeled blood vessels (green) and microbubbles stabilized by fluorescent nanoparticles (white). Scale bar = 50 μm . E) Fluorescence intensity as a function of time in the vasculature (\circ) and in the extravascular space (Δ). The mean and standard error of 11 time series are presented.

bound to lipid structures, Nile red in NPs and tissue autofluorescence. Fig. 6 presents one CLSM image where the emission spectra of different objects are displayed together with reference spectra. The Nile red fluorescence with an emission peak at 585 nm (Fig. 6A) was observed in large circular areas that had a homogeneous distribution of the fluorescent dye. The reference spectrum in Fig. 6A is the average from several such objects. Histological sections (Fig. 6D–F) revealed that adipocytes are present among the cancer cells both in the periphery and central part of the tumors, and myocytes were occasionally observed. Based on the observation of adipocytes together with the emission spectrum corresponding to Nile red in a lipophilic environment, it was assumed that the large circular areas represented clusters of adipocytes. The much smaller circular areas of Nile red exhibited an emission peak at approximately 600 nm. The fluorescence spectrum is consistent with the emission spectra measured in solutions of PBCA NPs containing Nile red (Fig. 6B). The emission spectrum of Nile red from NPs was measured using both a spectrophotometer and the META detector on the CLSM and was found to be the same (data not shown). Thus, the small circular fluorescent dots represent NPs or aggregates of NPs. The tumor tissue also contained fluorescent objects with broader emission spectra above 600 nm. These spectra were similar to the autofluorescence recorded from tumor tissue not exposed to NPs (Fig. 6C).

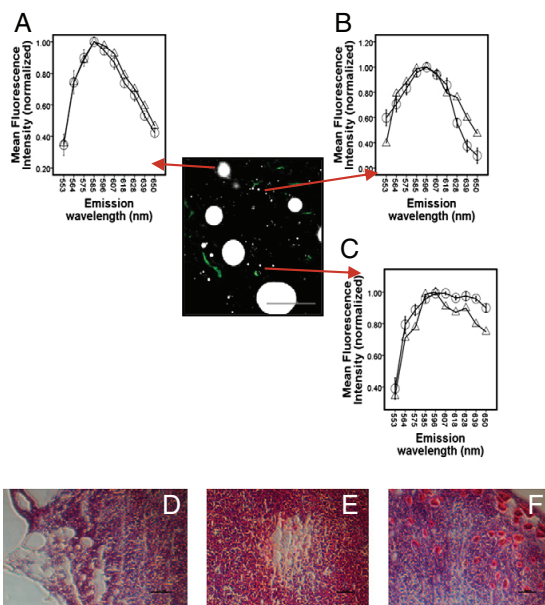


Fig. 6. A–C) CLSM image from a tumor section containing different fluorescent objects. Scale bar = 50 μm . A) Emission spectrum of a large, circular fluorescent structure (Δ) and emission spectra from similar structures (mean and standard error of 6 measurements) (\circ). B) Emission spectrum of a small fluorescent structure (Δ) and emission spectra from a solution of nanoparticles (mean and standard error of 6 measurements) (\circ). C) Emission spectrum of a small fluorescent structure (Δ) and emission spectra from autofluorescence in tumor tissue not exposed to nanoparticles (mean and standard error of 6 measurements) (\circ). D–F) Histological images (H&E staining) from tumor tissue revealing adipocytes in the periphery (D) and a central area (E), and myocytes (F) located among cancer cells.

3.6. Microscopic investigation of the distribution of Nile red from nanoparticle-stabilized microbubbles

3.6.1. Tumor uptake of nanoparticles and released Nile red

Images of the microdistribution of Nile red in periphery and central area of two tumors are presented in Fig. 7. The images are from tumors given NP-MBs and exposed to US with an MI of 0.4. There were large differences in the amount of extravasated NPs present in different areas within the same tumors, demonstrating the heterogeneous delivery of particles.

To obtain quantitative information about the amount of NPs present in the tumor tissue, the numbers of fluorescent objects in images acquired from the peripheral and central areas of tumor tissue sections were counted (Fig. 8). US with low MI enhanced significantly the number of NPs compared with the non-exposed group both in the periphery ($p = 0.002$, $r = 0.32$) (Fig. 8A) and the central parts of the tumor ($p < 0.000$, $r = 0.52$) (Fig. 8B), and the number of NPs increased further with increasing MI ($p = 0.004$ and $r = 0.54$ in periphery, $p = 0.036$ and $r = 0.7$ in central area). The mean rank values of NP cluster counts in non-exposed and low and high MI-exposed tumors were, respectively, 44.5, 67.3, and 88.1 in the periphery and 22.8, 45.0, and 56.9 in the central area of the tumors. The variation in the number of NPs from image to image was large, as shown by the indicated outliers. US using low MI increased the number of NPs to a larger extent in the central part of the tumor compared with the periphery ($p = 0.022$, $r = 0.25$), but no difference in the number of NPs in the two areas were observed for high MI US exposure. The large circular objects representing clusters of adipocytes were observed mainly in the

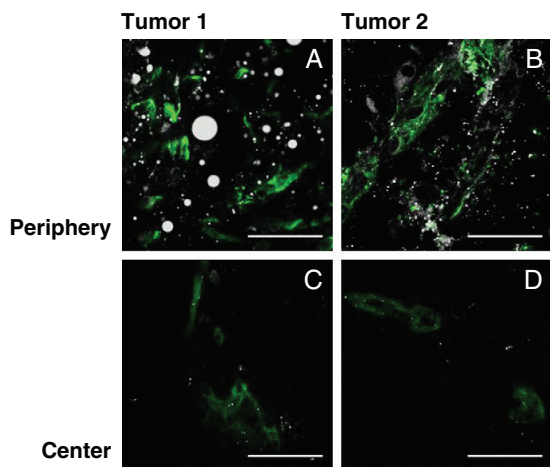


Fig. 7. Example CLSM images from different areas of two tumors after the administration of nanoparticle-stabilized microbubbles and exposing the tumors to 1-MHz ultrasound with an MI of 0.4. The amount and distribution of nanoparticles varies between areas within the tumors. Nile red fluorescence (white) and FITC-labeled blood vessels (green) are shown. Scale bar = 50 μ m.

peripheral areas (Fig. 8C). US enhanced the number of clusters of fluorescent adipocytes in the periphery of the tumor compared with non-exposed tumors ($p = 0.011$ and $r = 0.27$ for the low MI exposure and $p = 0.000$ and $r = 0.44$ for the higher MI exposure), and the mean rank of the fluorescent adipocyte counts was 52.7 for the non-exposed tumors and 68.4 and 79.95 in the two US exposed groups, respectively. In the central areas of the tumor, the number of fluorescent adipocytes was too low to perform any analysis.

3.6.2. Penetration of NPs from the blood vessels

Assessment of the distance from fluorescent structures to the closest blood vessel allows for estimation of the extent of penetration of NPs or released fluorescent dye into the ECM of the tumor. Low MI US increased the distance between NPs and blood vessels in the periphery ($p = 0.012$, $r = 0.24$) (Fig. 9A), where the mean rank values were 39.5 in the non-exposed tumors and 58.0 in the sonicated tumors. The distance was not affected by low MI US in the central part of the tumor (Fig. 9B). In the central part of the tumor, US exposure of higher MI seemed to be counterproductive, reducing the measured distance between NPs and blood vessels from a mean rank of 74.3 in non-exposed tumors to 49.5 in US-exposed tumors ($p = 0.001$, $r = 0.32$). The transport of Nile red that was released from the NPs and bound to adipocytes was not affected by either of the two US exposures (Fig. 9C).

3.7. Overall tumor uptake of Nile red from nanoparticle-stabilized microbubbles

To obtain information about the total tumor uptake of NPs, fluorescence from NPs and Nile red binding to adipocytes was measured in tile scan images from tumor sections. Tumor sections were imaged from one periphery to the other periphery of the sections at all 5 depths. The amount of fluorescence from the adipocytes and NPs, respectively, was quantified by a Matlab function after the linear unmixing process. Fig. 10 presents the distribution of NPs (A) and adipocytes (B) as a function of the position along the tile scan. Single observations of areas with strong fluorescence intensity resulted in peaks with large error bars. The total fluorescence, summarized across each tumor section and 5 tissue depths, is presented in Fig. 11. The tumor uptake of the NPs was

enhanced in the low MI group (mean rank = 27.2, $p = 0.001$, $r = 0.5$) as well as the higher MI group (mean rank = 26.7, $p = 0.000$, $r = 0.55$) compared with the non-exposed group (mean rank = 16.3). No significant difference was detected between the two US groups. US did not significantly alter the tumor uptake of Nile red bound to adipocytes; however, large variations between the tumors were found.

3.8. Tumor uptake of Nile red from nanoparticles without microbubbles

The total tumor uptake of NPs and Nile red bound to adipocytes was estimated from tile scans of the sections at all 5 depths as described for NP-MBs. Nile red fluorescence as a function of the position along the tile scan is presented in Fig. 12A, and the overall fluorescence, including both NPs and Nile red from adipocytes, is presented in Fig. 12B. US

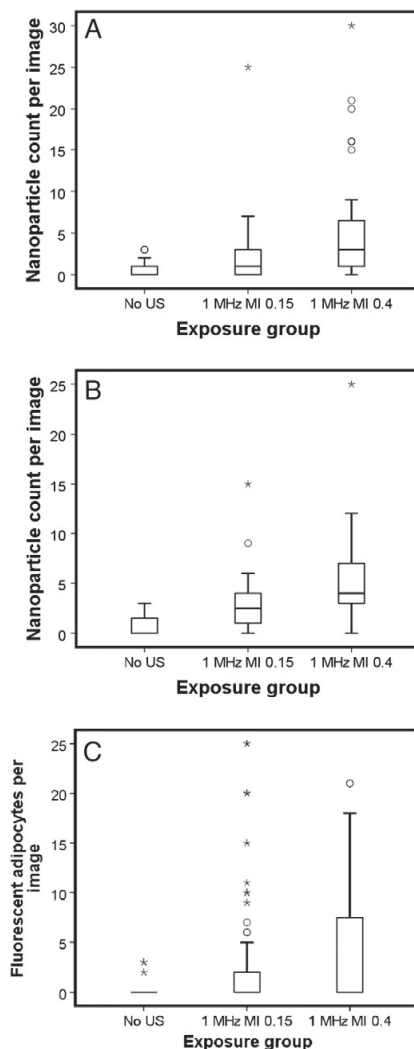


Fig. 8. Box plots showing the number of fluorescent objects counted per CLSM image. Number of clusters of nanoparticles in peripheral areas (A) and central areas (B). Number of clusters of fluorescent adipocytes in peripheral areas (C). The boxes are based on 64–83 measurements per group.

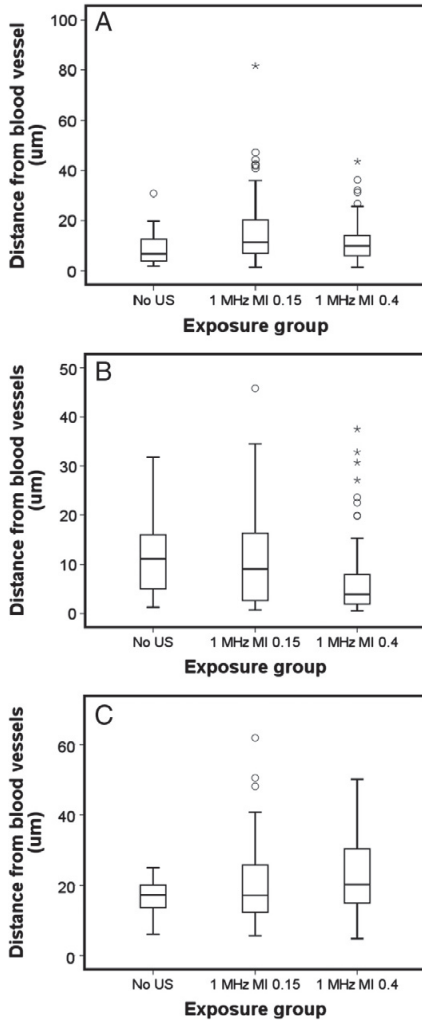


Fig. 9. Box plots showing the penetration distance of fluorescent objects into the tumor tissue. The distance has been measured by drawing a line from aggregates of nanoparticles (A and B) or fluorescent adipocytes (C) to the closest blood vessel on CLSM images acquired from tumor sections. The penetration distance has been measured from the aggregates of nanoparticles to the blood vessel in the tumor periphery (A) and in the tumor center (B), and from fluorescent adipocytes to the blood vessel in the tumor periphery (C). The boxes are based on 53–289 measurements per group.

performed 5 min after injection of NPs was more efficient in enhancing the uptake of Nile red fluorescence than US given after 24 h, and the enhancement was larger in the periphery of the tumor compared with the central area. When NPs had circulated for 5 min, US exposure at 5 MHz resulted in a significant increase in the tumor uptake of Nile red ($p = 0.043$, $r = 0.36$), whereas increasing the MI to 2.4 applying 300 kHz US did not cause any significant improvement. Furthermore, when the NPs had circulated for 24 h, US exposure using 300 kHz or 5 MHz did not enhance the tumor uptake of Nile red.

3.9. Collagen microscopy

The second-harmonic signal emitted from collagen fibers provided a good visualization of collagen in the tumor tissue. No apparent

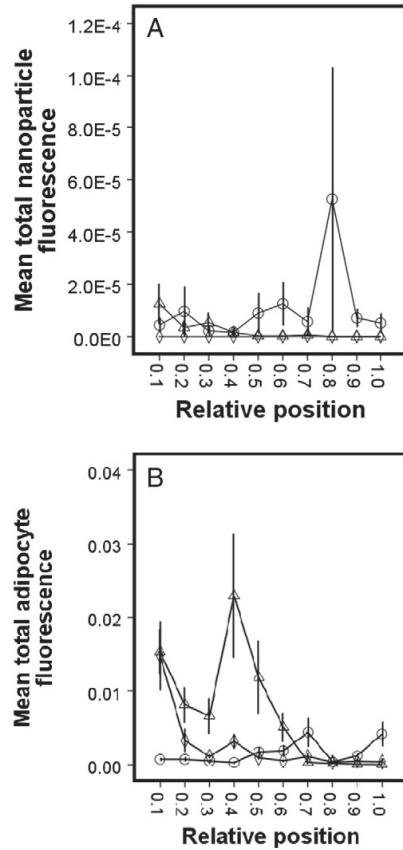


Fig. 10. Total fluorescence profiles in tumors from mice given nanoparticle-stabilized microbubbles. Fluorescence from nanoparticles (A) and adipocytes (B) as a function of position along tile scan images in tumors not exposed to ultrasound (∇), exposed to low MI ultrasound (Δ) and exposed to increased MI ultrasound (\circ). Each point represents the mean and standard error of 20–25 measurements.

difference in the structure or amount of collagen fibers was observed between non-sonated and US-exposed tumors. Tile scan images from the tumor periphery and towards the center are displayed in Fig. 13, where both collagen and FITC-labeled blood vessels are presented. The periphery of the tumor exhibited more collagen fibers that were more densely packed, whereas the fluorescent signals from collagen was less pronounced towards the center.

4. Discussion

4.1. US-induced extravasation

Exposing tumors to US had a positive effect on the tumor uptake of NPs. When NP-MBs were administered systemically followed by US exposure immediately afterwards, the tumor's uptake of NPs was improved both in the periphery and in the central regions. The number of clusters of NPs in the ECM was further improved when increasing the MI from 0.15 to 0.4. The enhancement in NPs is caused by improved extravasation of NPs. Intravital imaging of the vasculature and NPs demonstrated large heterogeneity of the vascular permeability, which has also been reported by others [12]. Three possible mechanisms could potentially be responsible for the enhancement. First, the detachment of

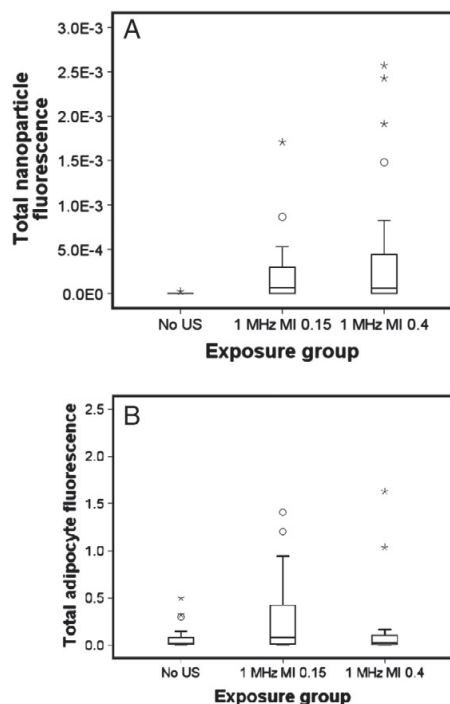


Fig. 11. Box plots showing the overall fluorescence measured in tile scans from tumor sections. Nanoparticle fluorescence (A) and adipocyte fluorescence (B) summarized along tile scans and from 5 depth levels. The boxes are based on 20–25 measurements per group.

NPs from bubble destruction due to US waves will result in a locally very high concentration of NPs in the vasculature in the sonicated field. These free NPs will be available for extravasation and can potentially leave the circulation simply due to the EPR effect. Burke and coworkers also investigated the benefit of having NPs linked to MBs upon US-mediated delivery [40]. During the destruction of the MBs, the delivery of the NPs was improved when the NPs were physically linked to the MBs, compared with co-injection of NPs and MBs, hence the effect of locally high concentrations of NPs at the delivery site is reasoned to be important. Second, the violent collapse of MBs due to inertial cavitation will generate fluid jet streams that can generate pores in the vessel wall [37,38], which can facilitate the extravasation of free NPs. Third, the effects that follow inertial cavitation can affect the released NPs so that they are pushed across the capillary wall and into the ECM of the tumor. During diagnostic imaging, the upper limit of the MI is set to 1.9 to avoid induction of cavitation when MBs have not been introduced [39]. In the presence of artificial MBs, acoustic cavitation appears at MI values well below the safety limit; however, the threshold for inertial cavitation will also depend on the shell and size of the MBs and their surroundings. In our setup, both US exposures applied enhanced the uptake of NPs, and the higher MI US resulted in a somewhat larger effect. When performing US exposure with an MI of 0.4, all MBs present in the sonication field will be destroyed during the first pulse of 10 oscillations, resulting in a very high concentration of free NPs in the circulation. The examination of tumor tissue revealed that many of these free NPs undergo extravasation. Due to the high PRF applied, new MBs from the circulation will be destroyed immediately as they enter the sonicated area. The lower MI US also increased the uptake of NPs, but less than that of higher MI, indicating that the effects on extravasation are less pronounced. The size distribution of our MBs is rather broad,

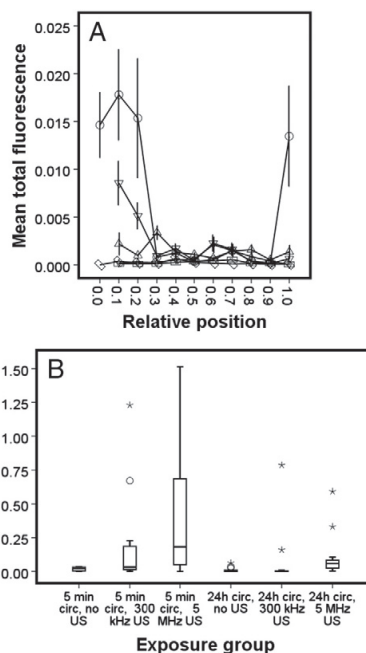


Fig. 12. A) Total fluorescence profiles in tumors from mice given nanoparticles without microbubbles. Fluorescence is displayed as a function of position along tile scan images in tumors with 5 min circulation and not exposed to ultrasound (○), 24 h circulation and not exposed to ultrasound (◊), 5 min circulation and 5 MHz ultrasound (○), 24 h circulation and 5 MHz ultrasound (Δ), 5 min circulation and 300 kHz ultrasound (▼) and 24 h circulation and 300 kHz ultrasound (□). B) Box plots revealing overall fluorescence from both nanoparticles and adipocytes measured in tile scans from tumor sections summarized along tile scans and from 5 depth levels. The boxes are based on 20–25 measurements per group.

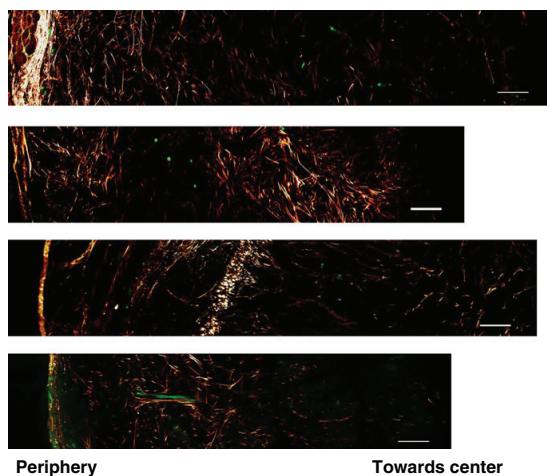


Fig. 13. CLSM tile scan images from two different tumor sections demonstrating the second-harmonic generated fluorescent signal from collagen (gold) and FITC-labeled blood vessels (green). The two upper images are from tumors not exposed to ultrasound, whereas the two lower images are from tumors exposed to 1 MHz ultrasound and MI of 0.4. The collagen fibers are more densely packed in the peripheral areas of the tumors. Scale bar = 150 μm .

and thus the fate of the MBs will differ when they are exposed to the low MI US, in the sense that some of the bubbles will be destroyed, while some will remain intact. Our MBs having a shell of NPs are probably stiffer than the commercial MBs surrounded by a lipid or protein shell, and higher acoustic energy might be required for oscillations. However, destruction of the MBs appeared at a MI of approximately 0.2 which is only slightly higher than for the commercial lipid shell MB SonoVue.

The presence of MBs was not required to increase the uptake of NPs and extravasation. Injecting NPs in solution without MBs and applying US 5 min later also enhanced the tumor uptake of NPs primarily in the periphery of the tumor. The US was applied at this time point to ensure a high concentration of NPs in the circulation as the circulation half-life was 1.3 h. The higher uptake in the periphery might be due to neo-angiogenesis and higher vessel density in these areas [41,42]. Additionally, more adipocytes were found in the periphery. 5 MHz US was more effective in promoting the tumor uptake of NPs than US of higher MI using 300 kHz. The temperature measurements on *ex vivo* tissue revealed that the 5 MHz exposure causes energy to be absorbed by the tissue, resulting in a minor temperature increase. A temperature increase might also have occurred *in vivo*, which potentially may have caused increased blood flow in the sonicated area [43] and these effects may have contributed to the improved delivery of the NPs into the tumors. The radiation force induced by the high-frequency US might also have pushed the NPs towards the vessel wall, thereby facilitating the extravasation without inducing sonoporation [44]. The vascular permeability is reported to be higher in the periphery of the tumor [45]; thus, forcing the NPs towards the vessel wall might be more efficient in the periphery than in the central areas of the tumor.

4.2. US-improved penetration through the extracellular matrix

After extravasation, the NPs must penetrate through the ECM to reach all parts of the tumor. In our study using NP-MBs, US was found to have a larger impact on the penetration throughout the tumor periphery compared with the central part of the tumor, and improved penetration was only observed for low MI US. In the low MI US, not all MBs will be destroyed immediately; and populations of MBs will be allowed to enter the sonication area and remain intact in the circulation before potential destruction takes place. Acoustic cavitation requires gas bubbles or small gas nuclei, and the injected MBs will only be present in the vasculature. The interaction between capillaries and oscillating MBs can cause the capillary wall to burst, and in this process NPs detached from the MB shell may receive enough energy to penetrate into the ECM. In contrast to the high MI US, intact MBs may persist for a longer time when the MI is reduced, and the destruction of bubbles may occur over a prolonged time. Radiation force is the other mechanical mechanism potentially responsible for the improved distribution of NPs. Radiation force increases with the frequency and intensity of the US beam and is not likely to be pronounced at 1 MHz and a pressure corresponding to MI of 0.15; hence, radiation force cannot explain the improved penetration. The difference in penetration between the periphery and central part of the tumor might be explained partly by the high IFP found in the tumor center. The IFP increases the first 400 μm from the periphery, followed by a stable high pressure further towards the center [15,46]. In the central part of the tumor, diffusion therefore becomes the major transport mechanism. However, diffusion is a slow process for large molecules such as NPs [47], and thus the penetration of NPs is poor. Hence, overcoming the interstitial transport barriers is easier in the periphery than in the central part of the tumor. When diffusing through the ECM, the NPs must penetrate through a network of collagen fibers embedded in a hydrophilic gel of glycosaminoglycans. The second harmonic imaging of collagen fibers revealed a denser network of collagen in the periphery than in the central part, as has been reported by others [48]; however, this network did not seem to cause a barrier for the NPs' penetration in the periphery.

To study the effect of US on NPs that had already accumulated in the ECM, US was performed 24 h after the injection of NPs without MBs. At this time point, NPs will have passively extravasated, although some of the NPs will also have been eliminated. No NPs were present in the vasculature, as the circulation half-life was rather short. US did not enhance the Nile red fluorescence when US was performed at this time point after NP injection. Additionally, the variation between tumors was large, likely due to the heterogeneity in vascular permeability.

It should be emphasized that the estimation of the penetration distances is semi-quantitative, as it is not possible to know from which blood vessels the NPs originate. The tumor is a 3D structure and the NPs that were imaged may have extravasated from blood vessels above or below the image plane.

4.3. US enhanced uptake of Nile red in adipocytes

The presence of non-neoplastic cells such as myocytes and adipocytes in the xenografts is a result of the tumor cells being implanted in a region where these cell types normally occur (Trond Viset, personal communication). The polymeric NPs were loaded with the hydrophobic dye Nile red, and the spectral analysis of Nile red in tumor tissue revealed that the dye is either located in the NPs or it is staining the adipocytes. US enhanced the uptake of Nile red by adipocytes. After US exposure, the fluorescence from the clusters of adipocytes was very bright, as demonstrated by the peaks in fluorescence intensity profile along tile scans. No such bright clusters of adipocytes were observed in non-sonicated tumors. It is not clear how US causes adipocytes to become more susceptible to Nile red. Low frequency, high intensity US has been reported to improve liposuction for fat reduction [49,50], and on *ex vivo* human adipose tissue, disruption of the plasma membrane of adipocytes, adipocytolysis and induction of apoptosis have been observed after US treatment [51,52]. US might also increase the release of Nile red from the NPs, and the hydrophobic dye will prefer the lipophilic environment within adipocytes. However, US has shown to have a limited effect on the release of Nile red from NPs in solution (data not shown).

5. Conclusion

The US-enhanced tumor uptake of our novel integrated polymeric NP-MBs clearly demonstrates the potential for these NPs as a carrier system for hydrophobic drugs. Stabilizing MBs with NPs makes it possible to improve the tumor uptake and the microdistribution throughout the tumor by applying US with low MI. Although we observed some uptake of NPs without MBs, this uptake requires high acoustic energy, which might damage the tissue. Surprisingly, we found that US enhanced the susceptibility of adipocytes to the hydrophobic dye.

The results indicate that US improves both extravasation and penetration throughout the ECM, and that the optimal US exposure might differ for these two transport steps. Thus, a multifrequency exposure might be useful for the optimal delivery of our new integrated NP-MBs.

Acknowledgments

The authors would like to thank Madelene Ericsson for preparing the tumor sections, Kristin Sæterbø for implanting the window chambers and for technical assistance, Astrid Bjørkøy for assistance during the operation of the confocal microscope, Einar Sulheim for providing a confocal laser scanning microscopy image, and senior consultant Trond Viset for examination of the histological sections. SINTEF also thanks Henkel Loctite, Cremer and Huntsman for providing BCA, Miglyol and Jeffamin, respectively, as a kind gift. This work was funded by the Norwegian Cancer Society (Grant no. 71014-PR2006-0394), NTNU's Strategic Area in Medical Technology and the Norwegian Research School in Medical Imaging (Research Council of Norway; Grant no. 190173/V50).






References

- [1] H. Maeda, J. Wu, T. Sawa, Y. Matsumura, K. Hori, Tumor vascular permeability and the EPR effect in macromolecular therapeutics: a review, *J. Control. Release* 65 (2000) 271–284.
- [2] J. Fang, H. Nakamura, H. Maeda, The EPR effect: unique features of tumor blood vessels for drug delivery, factors involved, and limitations and augmentation of the effect, *Adv. Drug Deliv. Rev.* 63 (2011) 136–151.
- [3] J.L. Arias, Liposomes in drug delivery: a patent review (2007–present), *Expert Opinion on Therapeutic Patents*, 2013.
- [4] C. Oerlemans, W. Bult, M. Bos, G. Storm, J.F. Nijssen, W.E. Hennink, Polymeric micelles in anticancer therapy: targeting, imaging and triggered release, *Pharm. Res.* 27 (2010) 2569–2589.
- [5] A. Tedcastle, R. Cawood, Y. Di, K.D. Fisher, L.W. Seymour, Virotherapy—cancer targeted pharmacology, *Drug Discov. Today* 17 (2012) 215–220.
- [6] S.A. Veltkamp, E.O. Witteveen, A. Capriati, A. Crea, F. Animati, M. Voogel-Fuchs, et al., Clinical and pharmacologic study of the novel prodrug delimitotecan (MEN 4901/T-0128) in patients with solid tumors, *Clin. Cancer Res.* 14 (2008) 7535–7544.
- [7] M. Aleku, P. Schulz, O. Keil, A. Santel, U. Schaeper, B. Dieckhoff, et al., Atu027, a liposomal small interfering RNA formulation targeting protein kinase N3, inhibits cancer progression, *Cancer Res.* 68 (2008) 9788–9798.
- [8] Y.L. Colson, M.W. Grinstaff, Biologically responsive polymeric nanoparticles for drug delivery, *Adv. Mater.* 24 (2012) 3878–3886.
- [9] L. Zhang, F.X. Gu, J.M. Chan, A.Z. Wang, R.S. Langer, O.C. Farokhzad, Nanoparticles in medicine: therapeutic applications and developments, *Clin. Pharmacol. Ther.* 83 (2008) 761–769.
- [10] H. Otsuka, Y. Nagasaki, K. Kataoka, PEGylated nanoparticles for biological and pharmaceutical applications, *Adv. Drug Deliv. Rev.* 55 (2003) 403–419.
- [11] N.K. Jain, M. Nahar, PEGylated nanocarriers for systemic delivery, *Methods Mol. Biol.* 624 (2010) 221–234.
- [12] F. Yuan, M. Leung, S.K. Huang, D.A. Berk, D. Papahadjopoulos, R.K. Jain, Microvascular permeability and interstitial penetration of sterically stabilized (stealth) liposomes in a human tumor xenograft, *Cancer Res.* 54 (1994) 3352–3356.
- [13] F. Yuan, Transvascular drug delivery in solid tumors, *Semin. Radiat. Oncol.* 8 (1998) 164–175.
- [14] C.H. Heldin, K. Rubin, K. Pietras, A. Ostman, High interstitial fluid pressure — an obstacle in cancer therapy, *Nat. Rev. Cancer* 4 (2004) 806–813.
- [15] L. Eikenes, O.S. Bruland, C. Brekken, C. deL Davies, Collagenase increases the transcapillary pressure gradient and improves the uptake and distribution of monoclonal antibodies in human osteosarcoma xenografts, *Cancer Res.* 64 (2004) 4768–4773.
- [16] C. deL Davies, L.M. Lundstrom, J. Frenglen, L. Eikenes, S.O. Bruland, O. Kaalhus, et al., Radiation improves the distribution and uptake of liposomal doxorubicin (caelyx) in human osteosarcoma xenografts, *Cancer Res.* 64 (2004) 547–553.
- [17] Y.H. Bae, Drug targeting and tumor heterogeneity, *J. Control. Release* 133 (2009) 2–3.
- [18] S. Eggen, M. Afadzi, E.A. Nilssen, S.B. Haugstad, B. Angelsen, C. deL Davies, Ultrasound improves the uptake and distribution of liposomal doxorubicin in prostate cancer xenografts, *Ultrasound Med. Biol.* 39 (2013) 1255–1266.
- [19] F. Yan, L. Li, Z. Deng, Q. Jin, J. Chen, W. Yang, et al., Paclitaxel–liposome–microbubble complexes as ultrasound-triggered therapeutic drug delivery carriers, *J. Control. Release* 166 (2013) 246–255.
- [20] K. Timbie, C. Burke, E. Nance, G. Woodworth, G.W. Miller, J. Hanes, et al., Ultrasound-targeted delivery of systemically administered therapeutic nanoparticles, *J. Acoust. Soc. Am.* 134 (2013) 4047.
- [21] S. Fokong, B. Theek, Z. Wu, P. Koczera, L. Appold, S. Jorge, et al., Image-guided, targeted and triggered drug delivery to tumors using polymer-based microbubbles, *J. Control. Release* 163 (2012) 75–81.
- [22] S. Kotopoulos, A. Delalande, M. Popa, V. Mamaeva, G. Dimcevski, O.H. Gilja, et al., Sonoporation-enhanced chemotherapy significantly reduces primary tumour burden in an orthotopic pancreatic cancer xenograft, *Mol. Imaging Biol.* 16 (2014) 53–62.
- [23] S. Kotopoulos, G. Dimcevski, O.H. Gilja, D. Hoem, M. Postema, Treatment of human pancreatic cancer using combined ultrasound, microbubbles, and gemcitabine: a clinical case study, *Med. Phys.* 40 (2013) 072902.
- [24] M.H. Gaber, N.Z. Wu, K. Hong, S.K. Huang, M.W. Dewhirst, D. Papahadjopoulos, Thermosensitive liposomes: extravasation and release of contents in tumor microvascular networks, *Int. J. Radiat. Oncol. Biol. Phys.* 36 (1996) 1177–1187.
- [25] G. Kong, M.W. Dewhirst, Hyperthermia and liposomes, *Int. J. Hyperthermia* 15 (1999) 345–370.
- [26] A.P. Sarvazyan, O.V. Rudenko, W.L. Nyborg, Biomedical applications of radiation force of ultrasound: historical roots and physical basis, *Ultrasound Med. Biol.* 36 (2010) 1379–1394.
- [27] H.A. Hancock, L.H. Smith, J. Cuesta, A.K. Durrani, M. Angstadt, M.L. Palmeri, et al., Investigations into pulsed high-intensity focused ultrasound-enhanced delivery: preliminary evidence for a novel mechanism, *Ultrasound Med. Biol.* 35 (2009) 1722–1736.
- [28] W. Lauterborn, T. Kurz, Physics of bubble oscillations, *Rep. Prog. Phys.* 73 (2010) 88.
- [29] C.K. Weiss, M.R. Lorenz, K. Landfester, V. Mailander, Cellular uptake behavior of unfunctionalized and functionalized PBCA particles prepared in a miniemulsion, *Macromol. Biosci.* 7 (2007) 883–896.
- [30] Y.A. Mørch, P.M. Stenstad, R. Schmid, R. Hansen, S. Berg, S. Eggen, et al., Ultrasound-mediated delivery of a novel nanoparticle–microbubble platform, Conference proceedings, European Summit for Clinical Nanomedicine and Targeted Medicine 6/13, Basel, Switzerland, 2013.
- [31] P. Greenspan, E.P. Mayer, S.D. Fowler, Nile red: a selective fluorescent stain for intracellular lipid droplets, *J. Cell Biol.* 100 (1985) 965–973.
- [32] W. Nicklas, P. Baneux, R. Boot, T. Decelle, A.A. Deeny, M. Fumanelli, et al., Recommendations for the health monitoring of rodent and rabbit colonies in breeding and experimental units, *Lab. Anim.* 36 (2002) 20–42.
- [33] N.K. Reitan, M. Thuen, P.E. Goa, C. deL Davies, Characterization of tumor microvascular structure and permeability: comparison between magnetic resonance imaging and intravital confocal imaging, *J. Biomed. Opt.* 15 (2010) 036004.
- [34] M. Afadzi, C. deL Davies, Y.H. Hansen, T. Johansen, O.K. Standal, R. Hansen, et al., Effect of ultrasound parameters on the release of liposomal calcein, *Ultrasound Med. Biol.* 38 (2012) 476–486.
- [35] A. Erikson, J. Ortegren, T. Hompland, C. deL Davies, M. Lindgren, Quantification of the second-order nonlinear susceptibility of collagen I using a laser scanning microscope, *J. Biomed. Opt.* 12 (2007) 044002.
- [36] S. Hak, N.K. Reitan, O. Haraldseth, C. deL Davies, Intravital microscopy in window chambers: a unique tool to study tumor angiogenesis and delivery of nanoparticles, *Angiogenesis* 13 (2010) 113–130.
- [37] V. Frenkel, Ultrasound mediated delivery of drugs and genes to solid tumors, *Adv. Drug Deliv. Rev.* 60 (2008) 1193–1208.
- [38] H. Shankar, P.S. Page, Potential adverse ultrasound-related biological effects: a critical review, *Anesthesiology* 115 (2011) 1109–1124.
- [39] R.S. Meltzer, Food and Drug Administration ultrasound device regulation: the output display standard, the “mechanical index,” and ultrasound safety, *J. Am. Soc. Echocardiogr.* 9 (1996) 216–220.
- [40] C.W. Burke, Y.-H. Hsiang, E. Alexander IV, A.L. Klibanov, R.J. Price, Covalently linking poly(lactic-co-glycolic acid) nanoparticles to microbubbles before intravenous injection improves their ultrasound-targeted delivery to skeletal muscle, *Small* 7 (2011) 1227–1235.
- [41] D.B. Ellegala, H. Leong-Poi, J.E. Carpenter, A.L. Klibanov, S. Kaul, M.E. Shaffrey, et al., Imaging tumor angiogenesis with contrast ultrasound and microbubbles targeted to alpha(v)beta3, *Circulation* 108 (2003) 336–341.
- [42] S. Hak, J. Cebulla, E.M. Huuse, C. deL Davies, W.J. Mulder, H.B. Larsson, et al., Periodicity in tumor vasculature targeting kinetics of ligand-functionalized nanoparticles studied by dynamic contrast enhanced magnetic resonance imaging and intravital microscopy, *Angiogenesis* 17 (2014) 93–107.
- [43] C.Y. Lai, B.Z. Fite, K.W. Ferrara, Ultrasonic enhancement of drug penetration in solid tumors, *Front. Oncol.* 3 (2013) 204.
- [44] P. Dayton, A. Klibanov, G. Brandenburger, K. Ferrara, Acoustic radiation force *in vivo*: a mechanism to assist targeting of microbubbles, *Ultrasound Med. Biol.* 25 (1999) 1195–1201.
- [45] H.F. Dvorak, J.A. Nagy, J.T. Dvorak, A.M. Dvorak, Identification and characterization of the blood vessels of solid tumors that are leaky to circulating macromolecules, *Am. J. Pathol.* 133 (1988) 95–109.
- [46] Y. Boucher, L.T. Baxter, R.K. Jain, Interstitial pressure gradients in tissue-isolated and subcutaneous tumors: implications for therapy, *Cancer Res.* 50 (1990) 4478–4484.
- [47] L. Eikenes, I. Tufto, E.A. Schnell, A. Bjorkoy, C. deL Davies, Effect of collagenase and hyaluronidase on free and anomalous diffusion in multicellular spheroids and xenografts, *Anticancer Res.* 30 (2010) 359–368.
- [48] T. Hompland, A. Erikson, M. Lindgren, T. Lindmo, C. deL Davies, Second-harmonic generation in collagen as a potential cancer diagnostic parameter, *J. Biomed. Opt.* 13 (2008) 054050.
- [49] N. Lawrence, W.P. Coleman III, The biologic basis of ultrasonic liposuction, *Dermatol. Surg.* 23 (1997) 1197–1200.
- [50] M.L. Zocchi, Basic physics for ultrasound-assisted lipoplasty, *Clin. Plast. Surg.* 26 (1999) 209–220.
- [51] P. Palumbo, B. Cinque, G. Miconi, C. La Torre, G. Zoccali, N. Vrentzos, et al., Biological effects of low frequency high intensity ultrasound application on *ex vivo* human adipose tissue, *Int. J. Immunopathol. Pharmacol.* 24 (2011) 411–422.
- [52] D. Pugliese, E. Maiorano, M. Pascone, Histopathological features of tissue alterations induced by low frequency ultrasound with cavitation effects on human adipose tissue, *Int. J. Immunopathol. Pharmacol.* 26 (2013) 541–547.

Paper II

ORIGINAL ARTICLE

Ultrasound and magnetic resonance imaging for group stratification and treatment monitoring in the transgenic adenocarcinoma of the mouse prostate model

Stein-Martin T. Fagerland MD^{1,2}  | Deborah K. Hill PhD²  |
Annemieke van Wamel PhD¹  | Catharina de Lange Davies PhD¹  | Jana Kim PhD² 

¹Department of Physics, Norwegian University of Science and Technology, Trondheim, Norway

²Department of Circulation and Medical Imaging, Norwegian University of Science and Technology, Trondheim, Norway

Correspondence

Catharina de Lange Davies, Department of Physics, NTNU, Høgskoleringen 5, 7491 Trondheim, Norway.
Email: catharina.davies@ntnu.no

Funding information

The Research Council of Norway, Grant/Award Number: 240316; Norwegian Cancer Society, Grant/Award Number: 6824920-2015; Liaison committee between the Central Norway Regional Health Authority and NTNU, Grant/Award Number: 90059700

Abstract

Background: The transgenic adenocarcinoma of the mouse prostate (TRAMP) is a widely used genetically engineered spontaneous prostate cancer model. However, both the degree of malignancy and time of cancer onset vary. While most mice display slowly progressing cancer, a subgroup develops fast-growing poorly differentiated (PD) tumors, making the model challenging to use. We investigated the feasibility of using ultrasound (US) imaging to screen for PD tumors and compared the performances of US and magnetic resonance imaging (MRI) in providing reliable measurements of disease burden.

Methods: TRAMP mice ($n = 74$) were screened for PD tumors with US imaging and findings verified with MRI, or in two cases with gross pathology. PD tumor volume was estimated with US and MR imaging and the methods compared ($n = 11$). For non-PD mice, prostate volume was used as a marker for disease burden and estimated with US imaging, MRI, and histology ($n = 11$). The agreement between the measurements obtained by the various methods and the intraobserver variability (IOV) was assessed using Bland-Altman analysis.

Results: US screening showed 81% sensitivity, 91% specificity, 72% positive predictive value, and 91% negative predictive value. The smallest tumor detected by US screening was 14 mm^3 and had a maximum diameter of 2.6 mm. MRI had the lowest IOV for both PD tumor and prostate volume estimation. US IOV was almost as low as MRI for PD tumor volumes but was considerably higher for prostate volumes.

Conclusions: US imaging was found to be a good screening method for detecting PD tumors and estimating tumor volume in the TRAMP model. MRI had better repeatability than US, especially when estimating prostate volumes.

KEYWORDS

cancer monitoring, preclinical, prostate cancer, prostate volume, repeatability, tumor volume

1 | INTRODUCTION

Prostate cancer (PCa) is the most common cancer in men in the European Union with estimated 450 000 new cases in 2018.¹ Even

though overall survival is high, 107 300 men were estimated to die from PCa in 2018.¹ New treatments are required to improve survival, and good disease models are needed to select the most promising treatments in preclinical trials. Mouse cancer models are often used

even though the mouse prostate differs from the human prostate in many respects. Unlike the human prostate, the mouse prostate does not have a fibrous capsule, is divided into multiple lobes, and is located in the abdominal cavity. The most commonly used mouse models in preclinical PCa studies are immunodeficient mice with subcutaneous xenografts grown from human cancer cell lines.² Several factors make these models less representative of human cancer, for example, immunodeficiency, homogenous tumor genetics, and, in the case of subcutaneous models, ectopic placement of the tumor.² It is believed that genetically engineered models (GEMs), with a functional immune system and orthotopic spontaneous cancer onset, are superior models that more accurately mimic human disease. Despite its promise, the use of GEM is still limited because of large variations in the degree of malignancy and age at cancer onset, which lead to high variation within treatment groups and planning experiments can be challenging.

The transgenic adenocarcinoma of the mouse prostate (TRAMP) is a widely used spontaneous PCa model.^{3,4} TRAMP mice develop cancer gradually from normal cells that transition through prostatic intraepithelial neoplasia to cancer.⁵⁻⁷ Because of neoplasia, the TRAMP prostate outgrows wild-type mouse prostates by 12 weeks of age. The TRAMP prostates continue growing as mice age, while wild-type mouse prostate volumes stabilize by 24 weeks of age.⁸ However, the disease progression is heterogenous, and a subgroup develops fast-growing poorly differentiated (PD) tumors from around 12 weeks of age.⁹ After PD tumor detection, mice often need to be euthanized within a few weeks because of tumor burden affecting animal welfare, whereas mice without PD tumors can live much longer, often up to 1 year of age.¹⁰ Consequently, the TRAMP model displays distinct phenotypes with different disease progression, which can make it challenging to determine treatment timepoints and to measure treatment response.

Variation in the cancer phenotype and age at cancer onset in the TRAMP model requires strategies to reduce the variation in outcome measurements. One strategy is starting the treatment when mice are young and the variation between individual mice is low. In such studies, treatment starts before cancer onset and the studies are often called chemopreventive. Another strategy is to use longitudinal outcome measurements acquired with *in vivo* imaging, enabling stratification of the mice in different treatment groups based on the phenotype and the use of longitudinal statistical methods.

A number of outcome measurements are used to compare the efficacy of treatments in the TRAMP model. Methods based on histology are most commonly used and several grading systems based on hematoxylin and eosin-stained sections have been developed for the TRAMP model^{6,7,10-13} and are often combined with immunohistochemistry markers for proliferation, apoptosis, and others. Often, tumor or prostate size is used to measure the treatment effect. The measurement is usually done *ex vivo*, since the prostate and prostate tumors are inaccessible for caliper measurements. Less frequently, imaging techniques are used to assess disease progression or treatment response *in vivo*. For PD mice, tumor volume is sometimes used to measure tumor burden.⁹ However, most TRAMP mice do not develop PD tumors and an alternative

treatment efficacy outcome such as prostate volume must be used.^{14,15} It has previously been shown that the prostate volume of the TRAMP background strain C57BL/6 does not usually grow past 40 mm³, while TRAMP mice can reach a volume of around 100 mm³ when they are 25 weeks of age.⁸ The change in prostate volume can, therefore, be attributed to neoplasia of the prostate in the TRAMP and be a marker of disease progression. However, the growth is not always caused by malignant disease and might not indicate aggressiveness or metastatic potential.

We hypothesize that *in vivo* imaging can be used to overcome challenges posed by the TRAMP model, by offering longitudinal outcome measurements and treatment group stratification based on phenotype. This could enable the use of more powerful longitudinal statistical analysis and reduce the number of mice needed per treatment group. Examples of longitudinal measurements are volume change over time, volume doubling time, and tumor-free survival. In this study, we investigated the performance of ultrasound (US) and magnetic resonance imaging (MRI) for imaging pathology of the prostate. Both imaging modalities are widely available in preclinical imaging facilities. Compared with MRI scanners, US scanners are generally less expensive to purchase, operate, and require less infrastructure. Moreover, US image acquisition is often quicker than MRI. Consequently, we were particularly interested in examining whether US imaging could be used to detect and measure changes in the prostate in the TRAMP model.

Thus, this study addresses two of the main challenges working with the TRAMP model; the unpredictable onset of PD tumors, and longitudinal monitoring of cancer progression or treatment response. First, we investigated the PD tumor screening performance of US imaging using MRI or gross pathology (in two cases) for verification. Second, we estimated PD tumor volume and compared agreement and intraobserver variability (IOV) for US imaging and MRI. Finally, we performed prostate volume measurements for non-PD mice and compared the agreement and IOV for US imaging, MRI, and histology.

2 | MATERIALS AND METHODS

2.1 | Mice

Mice were bred from an in-house colony established at the Norwegian University of Science and Technology (NTNU, Trondheim, Norway), with TRAMP mice originally purchased from the Jackson Labs in 2012. Initially, TRAMP mice homozygous for the TRAMP mutation were used in our experiments, but after a literature review, we changed to breeding heterozygous TRAMP mice in accordance with the majority of TRAMP studies. The in-house colony consisted of TRAMP mice homozygous for the TRAMP mutation. Heterogenous mice were bred using homozygous TRAMP females and C57BL/6 males acquired from the Jackson Labs. The presence of TRAMP mutation in the offspring was verified by a polymerase chain reaction. PD tumor screening and volume estimation were performed on mice heterozygous for the TRAMP mutation and prostate volume were calculated for TRAMP mice homozygous for the TRAMP mutation. All mice were housed

under specific pathogen-free conditions, in groups of one to six in ventilated cages (Model 1284L; Tecniplast) at temperatures from 21°C to 23°C, with 45% to 60% relative humidity, 70 air changes per hour and ad libitum access to food and sterile water.

2.2 | Ethics

All animal experiments were approved by the Norwegian Animal Research Authority and Norwegian Food Safety Authority.

2.3 | US imaging protocol and volume estimation

PD tumor screening and measurement of tumor volume were performed using a FUJIFILM Visualsonics Vevo 3100 scanner with an MX550D probe with 40 MHz center frequency, $30 \times 30 \mu\text{m}^2$ in-plane resolution and $80 \mu\text{m}$ through-plane resolution. Images were acquired every $76 \mu\text{m}$ using a 3D-motor. Imaging for prostate volume estimation was done with a FUJIFILM Visualsonics Vevo 2100 scanner with an MS550D probe with 40 MHz center frequency, $40 \times 40 \mu\text{m}^2$ axial resolution, and $90 \mu\text{m}$ lateral resolution. Images were acquired every $32 \mu\text{m}$ using a 3D-motor. The reason for the system change was an upgrade. Mice were kept under anesthesia during imaging using 1.5% to 2.5% isoflurane with 0.5 L/min 5:1 air:O₂ mix. Mice were restrained in the supine position by taping the legs to the imaging stage. Respiration was monitored visually, and anesthesia was adjusted to a respiration rate around 80 breaths per minute. Before imaging, the abdomen was shaved with an electric razor and depilation cream was used to remove remaining fur. US gel was applied before imaging. The US transducer was placed over the lower abdomen with an axial orientation. The bladder was easy to locate because of its size and anechoic urine content. After identifying the bladder, the transducer was swept caudally until the urethra was identified. The prostate was identified as a heterogeneous, hypoechoic structure ventral, lateral and often dorsal to the urethra. Gain and dynamic range were adjusted to see the prostate clearly while maintaining contrast to surrounding tissue. During PD tumor screening, the transducer was pressed manually against the pelvic region to detect tissues that were stiffer than the prostate. PD tumors were identified as spherical, hypoechogenic, with a heterogeneous contrast and were less compressible than surrounding tissue. After the extent of the prostate had been identified, a 3D-scan was acquired with the 3D-motor. Image stacks were imported into the Vevo LAB (FUJIFILM Visualsonics) software, processed with the "load into 3D function," exported as "TIFF for 3D Volume Slice (.tif)" and opened in FIJI ImageJ. A region of interest (ROI) was drawn around the PD tumor or prostate depending on the phenotype. For mice without PD tumor, ROIs were drawn over the ventral, dorsal, and lateral prostate lobes for approximately every 5th to 10th frame and interpolation was performed between frames. In the cranial direction, segmentation stopped when the seminal vesicle appeared, visualized as hypo or anechoic cystic septate structures. The volume of the ROIs in the image stack was calculated based on voxel size.

2.4 | MRI protocol and volume estimation

MRI was performed on a Bruker 7T Biospec 70/20 Avance III. Axial T2-weighted images were acquired using a RARE spin-echo sequence with fat suppression. For PD tumor detection and size measurement, several different coil setups and sequence parameters were used due to optimization at the beginning of the study: (a) four PD tumors were verified using an 86 mm volume resonator coil for RF transmission and reception with TE 58.5 ms, TR 4000 ms, RARE factor 8, averages 6, in-plane resolution $0.2 \times 0.2 \text{ mm}^2$, slice thickness 0.8 mm and acquisition time 3.7 minutes; (b) three PD tumors were verified using an 86 mm volume resonator coil for RF transmission and a phased array rat brain surface coil for RF reception with TE 58.5 ms, TR 4000 ms, RARE factor 8, averages 12, in-plane resolution $0.15 \times 0.15 \text{ mm}^2$, slice thickness 0.6 mm and acquisition time 5.2 minutes; (c) nine PD tumors were verified using an 86 mm volume resonator coil for RF transmission and a phased array mouse heart surface coil for RF reception with TE 58.5 ms, TR 5000 ms, RARE factor 6, averages 6, in-plane resolution $0.1 \times 0.1 \text{ mm}^2$, slice thickness 0.4 mm, and acquisition time 10 minutes. The third setup was preferred since the mouse heart coil gave the best signal from the prostate area compared with the volume resonator coil and the rat brain coil. All MRI PD tumor volume measurements were done with the third setup. For prostate volume measurements, axial T2w RARE images were acquired using an 86 mm volume resonator coil for RF transmission and a phased array mouse heart surface coil for RF reception with TE 36 ms, TR 5500 ms, RARE factor 8, averages 5, in-plane resolution $0.1 \times 0.1 \text{ mm}^2$, slice thickness 0.33 mm, and acquisition time 7 minutes. The TE was changed from 36 to 58.5 ms to increase the contrast between prostate tissue and seminal vesicle.

Mice were kept under anesthesia with 1.5% to 2.5% isoflurane with 0.5 L/min 5:1 air:O₂ mix. Respiration was monitored with a pressure sensor connected to a physiological monitoring system (SA Instruments) and anesthesia adjusted to a respiration rate around 80 breaths per minute. Mice were restrained in the scanner bed in a prone position using tape across the lower back. The imaging volume was selected by using a quick localizer scan and a quick low-resolution scan in both axial and coronal orientation to identify the extent of the tumor or prostate. PD tumors were identified as spherical with a homogenous contrast and hyperintense signal compared with the surrounding tissue. Only the bladder displayed a higher signal than PD tumors. Prostate tissue was identified based on its heterogeneous signal and location mainly ventral, lateral, and dorsal to the urethra. MRI images were exported as DICOM files from Paravision 6.0.1 and loaded into FIJI ImageJ where ROIs were drawn manually on all volume slices and ROI volumes estimated.

2.5 | Histology protocol and volume estimation

Eleven TRAMP mice were imaged by US and MRI the same day and were euthanized immediately after imaging to harvest the prostates.

The prostate was harvested together with the seminal vesicle, bladder, and urethra and fixed in 4% formaldehyde and paraffin-embedded before sectioning with a microtome (Leica RM2255). Before embedding, the prostate was oriented using the bladder, ductus deference, and urethra as landmarks, to align histology sections to axial images from US and MRI to be able to compare the three diagnostic modalities. From all eleven prostates, five sections (5 μ m thick) were collected every 200 μ m and stained with hematoxylin-erythrosine-saffron (HES). Saffron stains collagen fibers, and HES staining is standard at our university's core facility. However, adding saffron did not help distinguishing prostate from surrounding tissue. Every other slide was scanned using brightfield with a Zeiss LSM810 microscope using a $\times 2.5$ objective with a numerical aperture of 0.085. Multiple images were acquired to cover each section and images were stitched together using the Zeiss Zen software. Files were opened in Zeiss Blue software and one ROI was drawn around the ventral, dorsal, and lateral prostate lobe in each section. ROIs were drawn based on characteristic histological features.¹⁶ After ROIs were drawn, the area of the ROIs was multiplied with the distance between slides and summed to estimate the prostate volume.

2.6 | Tumor screening

US screening for PD tumors was performed in 81 mice every third week in the age range from 16 to 24 weeks (Figure S1). The total number of US screens per mouse ranged from one to three. After PD tumor verification with MRI, no further US imaging was performed. MRI was used to verify the US findings in 72 mice and gross pathology in two mice. Seven mice were excluded since they died or had to be euthanized before MRI at week 25 due to kidney tumors or reduced activity as a sign of illness. Initially, US screening started at week 20, but after two mice needed to be euthanized because of large tumors, screening was moved to week 17 ± 1 week. These two mice were euthanized immediately due to animal welfare requirements, and US findings verified by gross pathology.

Mice with PD tumors detected by US screening were scanned with MRI the following day to verify the result. Mice with a negative US screen or a MRI verified false-positive result, were imaged again using US after 3 to 4 weeks. At 23 to 26 weeks of age, all mice were imaged with MRI to verify earlier US findings.

US screening performance was assessed by estimating sensitivity, specificity, positive predictive value (PPV), and negative predictive value (NPV). Sensitivity was defined as a number of true-positive/(true-positive + false-negative), specificity as true-negative/(true-negative + false-positive), PPV as true-positive/(true-positive + false-positive) and NPV as true-negative/(true-negative + false-negative). PD tumor growth rate was assessed in four mice that were imaged weekly from week 19 or 20 of age until tumor burden necessitated euthanasia. Tumor doubling time was estimated by fitting tumor growth data to an exponential function $V(t) = V_0 \exp(bt)$. The curve fitting toolbox in MATLAB R2018b was used to estimate the rate constant b and the doubling time was given by $t_d = \ln(2)/b$.

2.7 | Imaging modality comparison and IOV of volume estimates

PD tumor and prostate volume estimates were based on the sum of voxel volumes within ROIs containing PD tumors or prostate tissue. For mice without PD tumor, ROIs were limited to the ventral, dorsal, and lateral lobes of the prostate, since the anterior prostate lobe, can be difficult to distinguish from the seminal vesicle on images. ROIs were drawn in the same image stack by the same observer two times at least 1 week apart and the repeated measurements were used to assess IOV and to compare imaging modalities using the methods described by Bland and Altman.¹⁷ Volume estimations were done by SM Fagerland (MD), who had limited experience with US imaging, MRI, and histology at the start of the study. US training was supplied in two sessions by application specialists from FUJIFILM VisualSonics, MRI training was given by researchers with extensive experience with the TRAMP model and identification of the prostate on histological sections was based on the papers by Berman-Booty⁷ and Oliveira.¹⁶ Agreement between imaging modalities was visualized using a scatter plot and a Bland-Altman plot, where the difference between the modalities is plotted on the vertical axis and the mean of the results obtained by the two modalities on the horizontal axis. Because the magnitude of the difference is dependent on the size measured, we used percentage difference from the mean on the vertical axis to correct for the size-dependent variation.¹⁸ The mean of the differences between the repeated measurements was calculated and represented the bias or the systematic difference between the measurements. The standard deviation (SD) of the differences between repeated measurements was also calculated. The agreement between modalities and IOV was quantified using limits of agreement as defined by Bland-Altman. The limits of agreement are calculated as bias ± 1.96 SD. When the modalities were compared, the mean of two repeated measurements was used and the calculation of limits of agreement was corrected according to Bland-Altman.¹⁷ The precision of the estimated bias and limits of agreement were calculated using 95% confidence intervals (CIs), as described in the paper by Giavarina.¹⁸ Eleven mice with PD tumors were used to compare the tumor volume obtained by US imaging and MRI and to investigate the IOV of US and MRI volume estimations. Similarly, 11 mice with age span 21 to 31 weeks without PD tumors were used to compare prostate volume measurements obtained by US imaging, MRI, and HES sections and to investigate the IOV for each modality.

3 | RESULTS

3.1 | Characterization of TRAMP phenotypes

The TRAMP mice exhibited two different phenotypes. All mice displayed a hyperplastic prostate with atypia, but 22% developed a fast-growing PD prostate tumor in addition. No TRAMP mouse developed more than one PD tumor. Representative HES sections from the two phenotypes are shown in Figure 1. The PD tumors have few, sparse glands, and display anaplastic sheets of pleomorphic cells. The prostate tissue is generally

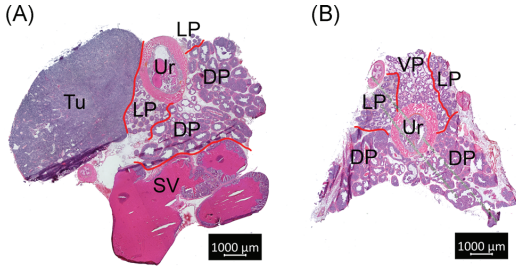


FIGURE 1 A, HES section from a TRAMP mouse prostate with a PD tumor of approximately 200 mm³ measured by MRI. B, HES section of prostate with a high degree of prostatic intraepithelial neoplasia in all lobes and especially the dorsal prostate. DP, dorsal prostate; HES, hematoxylin-erythrosine-saffron; LP, lateral prostate; MRI, magnetic resonance imaging; SV, seminal vesicle; TRAMP, transgenic adenocarcinoma of the mouse prostate; Tu, tumor; Ur, urethra; VP, ventral prostate [Color figure can be viewed at wileyonlinelibrary.com]

characterized by cells filling the lumen of glands, herniation of cells into the smooth muscle layer, and hyperplastic epithelium.

3.2 | PD tumor screening

The PD prostate tumors appeared relatively spherical and homogenous compared with surrounding tissue on both US and MR images and were often located in the ventral or lateral lobe of the prostate (Figure 2). Left-right image asymmetry could also be a sign of PD tumor, since the normal

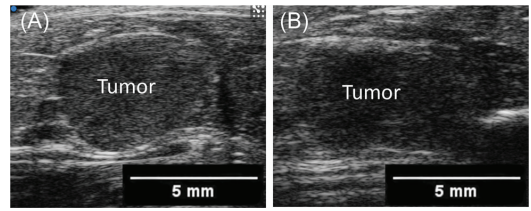


FIGURE 3 A, An US image of a PD tumor from a 20-week-old mouse acquired under compression and shows a clear border between the tumor and surrounding tissue. B, The same tumor with low compression during the same image session where the border is less well-defined. The tumor had a maximum diameter of 4.6 mm and volume 39.4 mm³ estimated by US. Based on MRI the volume was estimated to be 56.7 mm³. MRI, magnetic resonance imaging; PD, poorly differentiated; US, ultrasound [Color figure can be viewed at wileyonlinelibrary.com]

prostates display a left-right symmetry in axial images. US imaging and MRI differed in PD tumor signal intensity compared with surrounding tissue; PD tumor signal intensity was relatively low for US imaging and relatively high for T2-weighted MR images. Tumors smaller than 3 mm often had a heterogenous contrast and unclear border on US images. Compression could be used to enhance the contrast between tissues, as shown in Figure 3. The border between the tumor and surrounding tissue appeared more distinct when the tissue was compressed, as PD tumors were not as compressible as surrounding prostate tissue.

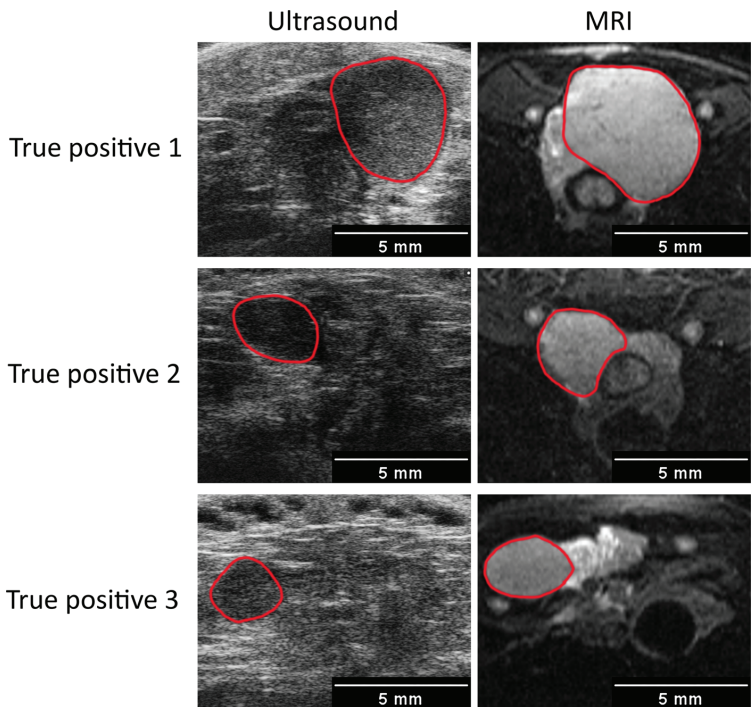


FIGURE 2 PD prostate tumors (outlined in red) imaged with US in the left column and MRI in the right column. The three mice were 17 weeks old when imaged. The tumors appear relatively spherical and homogenous compared with surrounding tissues. The signal intensity of PD prostate tumors is relatively low on US imaging and relatively high on T2-weighted MRI, compared with the surrounding tissue. MRI, magnetic resonance imaging; PD, poorly differentiated; US, ultrasound [Color figure can be viewed at wileyonlinelibrary.com]

TABLE 1 US screening performance in TRAMP mice verified by MRI (n = 72) and gross histology (n = 2)

Sensitivity	81%	True-positive	n = 13
Specificity	91%	False-positive	n = 5
Positive predictive value	72%	False-negative	n = 3
Negative predictive value	91%	True-negative	n = 53
Prevalence of prostate PD tumors	22%		

Abbreviations: MRI, magnetic resonance imaging; PD, poorly differentiated; TRAMP, transgenic adenocarcinoma of the mouse prostate; US, ultrasound

US imaging performed well in PD tumor screening. US imaging was performed one to three times per mouse in the age range 16 to 24 weeks. This resulted in 81% sensitivity, 91% specificity, 72% PPV, and 91% NPV (Table 1). Sixty-six cases were classified correctly as true-positive (13 mice) or as true-negative (53 mice). Eight cases were misclassified as false positives (5 mice) or false-negative (3 mice). The false negatives were detected with MRI 3 weeks after the last US screening and volumes were in the range of 21 to 93 mm³ measured with MRI. In four out of five false-positive cases the ventrolateral area of the prostate was misinterpreted as tumor (Figure 4). Misinterpretation occurred since the prostate sometimes shares characteristics with PD

tumors by appearing spherical during compression or a tilted mouse position can make the prostate appear asymmetrical. Twenty-two percent of the mice (16 of 74) developed PD tumors by 25 weeks of age.

Figure 5 shows mouse age and tumor volume at the time of PD prostate tumor detection either by US imaging or MRI. Volumes were estimated using MRI or US. US screening detected PD tumors as small as 14 mm³ measured with MRI and a maximum diameter of 2.6 mm when measured with US. PD tumor volume varied widely in mice of the same age, ranging from 14 to 420 mm³ in week 17 and 16 to 3100 mm³ in week 20. No PD tumors were detected at week 16 or 18. Four of the mice with PD tumors were imaged weekly by MRI until they reached a tumor diameter of more than 1.5 cm. The growth data for these four mice are plotted in Figure 5. The growth data were fitted to an exponential function and all R² values were greater than 0.99. On the basis of the exponential function, PD tumor doubling time was 4.0, 4.2, 5.3, and 5.9 days.

3.3 | Comparing tumor volume estimated by US imaging and MRI

PD tumor volumes (Table S1) estimated from US images correlated well with, but were generally smaller than MRI measurements, as

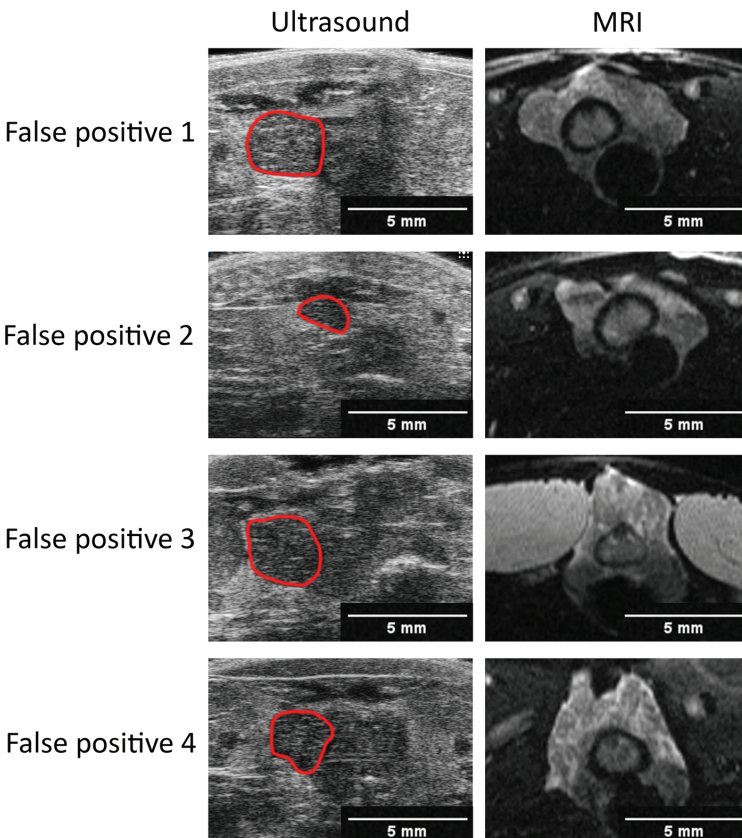


FIGURE 4 Images of the TRAMP model where US screening gave false-positive results. Corresponding US and MR images are shown in the left and right columns, respectively. Structures misinterpreted as PD tumors on US are outlined in red. Misinterpretation of the ventrolateral aspect of the prostate on US images led to four out of five false positives. MR, magnetic resonance; PD, poorly differentiated; TRAMP, transgenic adenocarcinoma of the mouse prostate; US, ultrasound [Color figure can be viewed at wileyonlinelibrary.com]

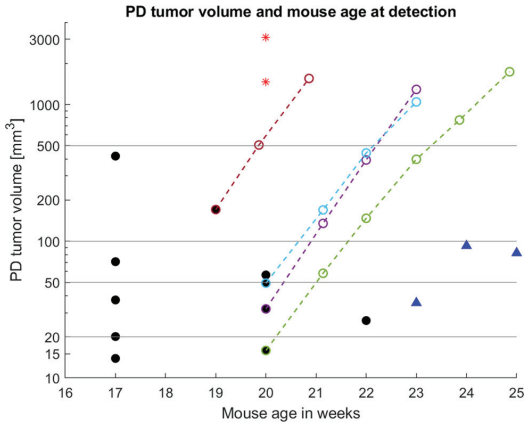


FIGURE 5 PD tumor volumes (n = 16) are plotted on a logarithmic scale on the vertical axis and mouse age at PD tumor detection on the horizontal axis. Black circles (n = 11) represent individual tumors detected with US and volumes were estimated by MRI. Red asterisks (n = 2) represent individual tumors for which volumes were estimated by US. Blue triangles (n = 3) indicate individual tumors detected and measured by MRI but not US (false negatives). The colored, dashed lines show growth data for four PD tumors. All growth data fitted an exponential function with $R^2 > 0.99$. MRI, magnetic resonance imaging; PD, poorly differentiated; US, ultrasound [Color figure can be viewed at wileyonlinelibrary.com]

demonstrated from the log-log scatter plot in Figure 6A. The tumor volumes for the 11 tumors varied from 8.1 to 587 mm³ when estimated with US imaging and 8.5 to 721 mm³ when estimated with MRI. To obtain more detailed information about the difference in the volumes obtained by the two imaging modalities, the data were

analyzed in a Bland-Altman plot (Figure 6B). The blue line indicates the systematic difference between the methods and shows that the tumor volumes measured by US imaging were on average 22% smaller than volumes measured by MRI, with a 95% CI of 5.4% to 38.9%. The red lines indicate the limits of agreement, which were -71.9% to 27.6% (Figure 6B).

3.4 | IOV in tumor volume estimation

IOV was slightly larger for US imaging than for MRI as shown on the Bland-Altman plot (Figures 7 and Tables S2, S3). The bias for US imaging and MRI was 2.6% (95% CI: -1.8%-7.1%) and -0.1% (95% CI: -3.8%-3.7%), respectively, indicating no systematic difference between the repeated measurements. The limits of agreement for volume measurements were -11.2% to 16.5% for US imaging and -11.1% to 10.9% for MRI.

3.5 | Comparing prostate volume measured by US imaging, MRI, and histology

Figure 8 shows prostate tissue ROIs for US imaging, MRI, and histology in three different mice (Tables S4-S6). The contrast between the prostate and surrounding tissues can be low, especially for US imaging. The border between the prostate and seminal vesicle is the most difficult to distinguish in US imaging and MRI, because of the uneven nature of the border and relatively low contrast. On HES images, the dorsal and anterior lobe could sometimes be mistaken for each other. Normally the lobes can be distinguished based on the epithelial lining of the gland, which is more columnar for the anterior gland, and the secretion, which is more eosinophilic in the anterior

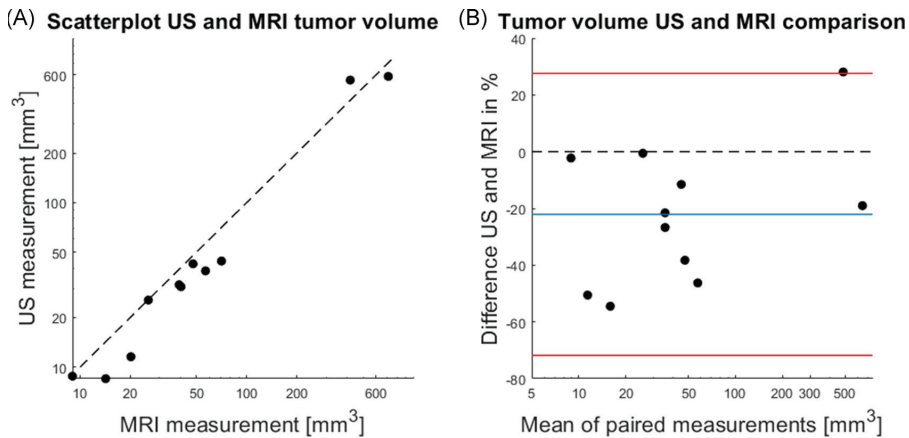


FIGURE 6 A, Log-log scatter plot comparing tumor volumes obtained by US imaging and MRI. The dashed line shows the line of equality. Circles represent the mean of paired PD volumes estimated by MRI vs PD volume estimated by US imaging. B, Bland-Altman plot comparing tumor volume estimated by US imaging and MRI. The vertical axis shows the percentage difference between volumes obtained by US imaging and MRI, and the horizontal axis shows the mean of the volumes from US imaging and MRI on a logarithmic scale. The blue line shows the mean of the differences, indicating that the tumor volumes measured by US imaging are on average 22% lower than MRI measured volumes. The red lines show the limits of agreement. MRI, magnetic resonance imaging; PD, poorly differentiated; US, ultrasound [Color figure can be viewed at wileyonlinelibrary.com]

Tumor volume intraobserver variation

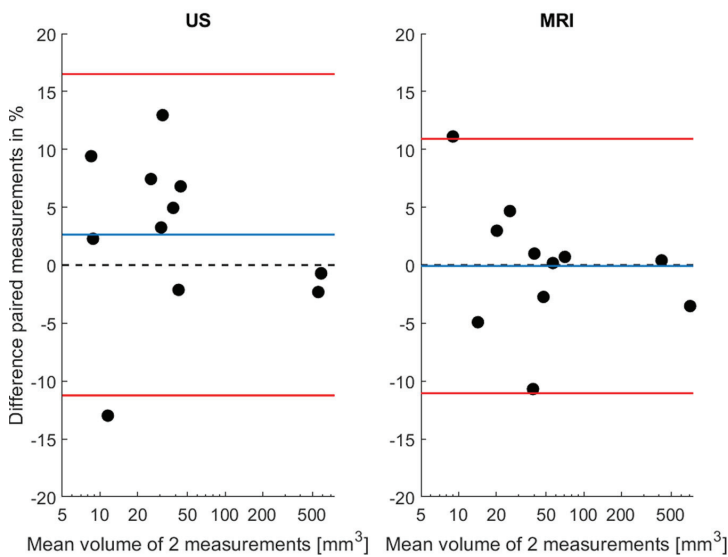


FIGURE 7 Bland-Altman plots of IOV in tumor volume obtained from US imaging and MRI. The vertical axis shows the percentage difference between two repeated measurements, and the horizontal axis shows the mean of the two repeated measurements (logarithmic scale) measured by US (left) or MRI (right). The blue lines indicate the mean of the differences and the red lines show the limits of agreement. Volume estimates from MRI have lower IOV than US imaging. IOV, intraobserver variability; MRI, magnetic resonance imaging; US, ultrasound [Color figure can be viewed at wileyonlinelibrary.com]

gland. However, sometimes neoplastic epithelium fills the glands and the hallmarks identifying the glands can disappear.

Prostate volume estimations from US images were, in general, much smaller than estimations from histology and MRI. MRI volume estimations were closer to histology volumes with a small overestimation, as

demonstrated from the log-log scatter plot in Figure 9A. The prostate volumes from 11 mice varied from 19.6 to 55.8 mm³ on US imaging, 33.6 to 97.4 mm³ on MRI, and 31.8 to 70.9 mm³ on histology. Comparisons between US and histology, US and MRI, and MRI and histology are plotted in a Bland-Altman plot to visualize and quantify the agreement

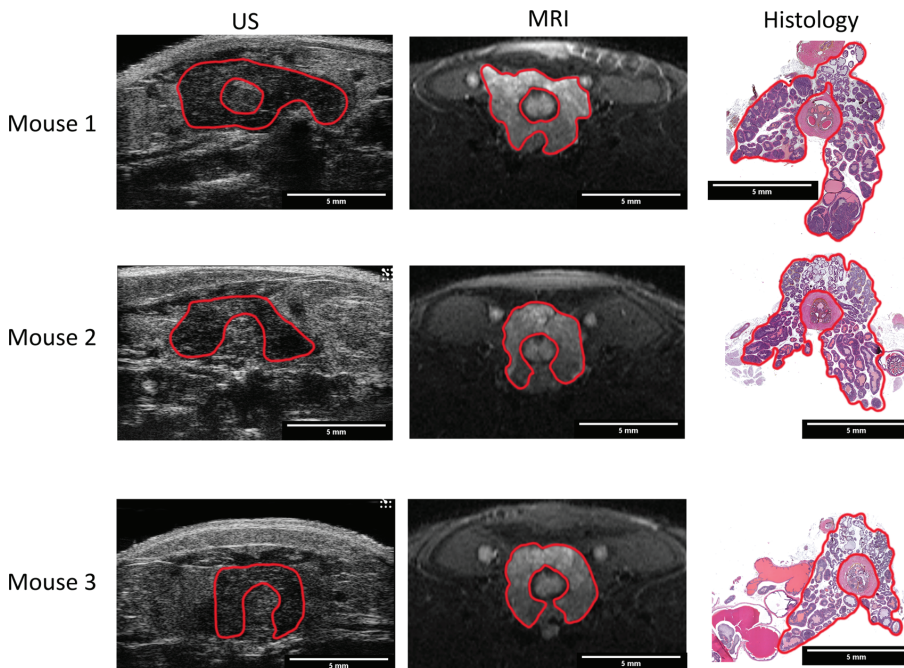


FIGURE 8 Segmentation of prostate for volume estimation in three representative mice with US imaging, MRI and histology. Prostate tissue is outlined in red. MRI, magnetic resonance imaging; US, ultrasound [Color figure can be viewed at wileyonlinelibrary.com]

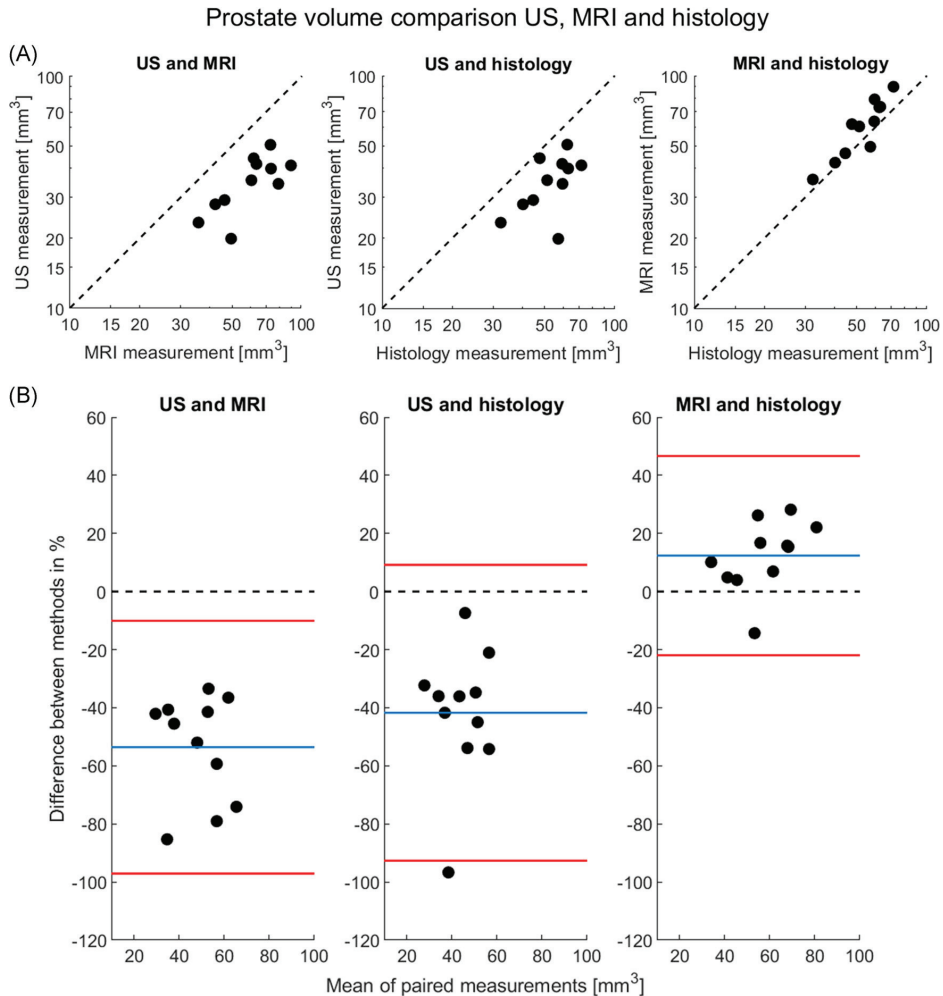


FIGURE 9 A, Log-log scatterplots comparing prostate volumes obtained from US imaging, MRI, and HES section scans. The dashed line shows the line of equality. Each circle represents the prostate volume of a different mouse. B, Bland-Altman plots comparing volume estimations from US, MRI, and histology. Percentage differences between measurements are plotted on the vertical axis and the mean of the measurements is plotted on the horizontal axis. The blue lines show the mean of the differences, and the red lines show the limits of agreement. HES, hematoxylin-erythrosine-saffron; MRI, magnetic resonance imaging, US, ultrasound [Color figure can be viewed at wileyonlinelibrary.com]

(Figure 9B). The limits of agreement between US and histology were -92.7% to 9.2% with a bias of -41.7% , the limits of agreement between US and MRI were -97.1% to -10.1% with a bias of 53.6% and the limits of agreement between MRI and histology were -21.9% to 46.6% with a bias of 12.4% .

3.6 | IOV in prostate volume

The IOV for prostate volume measurement was much larger for US imaging compared with MRI and histology, whereas the IOV for prostate volumes obtained by MRI and histology were almost the same as shown on the Bland-Altman plot (Figure 10 and Tables S7-

S9). The mean of the differences for US imaging, MRI, and histology was not significantly different from 0, indicating no systematic difference between the repeated measurements. The limits of agreement were -35.1% to 53.9% for US imaging, -24.3% to 20.2% for MRI and -26.8% to 19.0% for histology.

4 | DISCUSSION

Since the establishment of the TRAMP model in 1995,¹⁹ the model has been widely used to study PCa progression and to develop new therapies and strategies to prevent or treat PCa. However, working with the

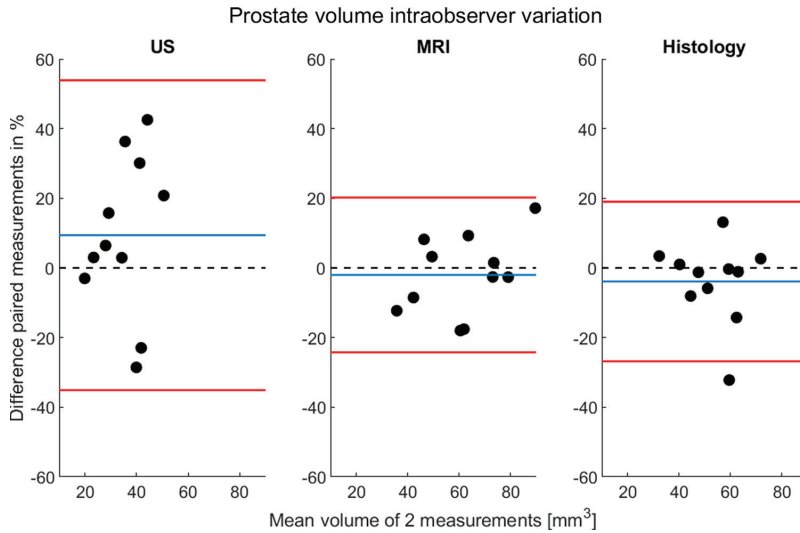


FIGURE 10 Bland-Altman plots showing IOV for volume estimation based on US imaging, MRI, and histology. The vertical axis is percentage differences between two repeated measurements and the horizontal axis is the mean of the two repeated measurements. The blue lines show the mean of the differences. The red lines show the limits of agreement. MRI and histology show comparable IOV, while US has a larger IOV. IOV, intraobserver variability; MRI, magnetic resonance imaging; US, ultrasound [Color figure can be viewed at wileyonlinelibrary.com]

TRAMP model is challenging because of unpredictable disease onset characteristics and variation in cancer malignancy. While histology has been the standard method to evaluate treatment response, imaging can improve treatment evaluation by enabling longitudinal measurements or stratifying TRAMP phenotypes before commencing treatment. Stratification reduces the number of mice needed in preclinical studies through a reduction in the variation in treatment response between groups. Most TRAMP mice do not develop solid tumors during their life span, but show the cancerous transformation of the prostate and increase in prostate volume; a smaller subgroup develops PD tumors, which causes a large variation in treatment outcomes. We demonstrated that US imaging, being a low-cost and broadly available imaging modality, could be used to screen TRAMP mice for PD tumors. In addition, PD tumor volumes obtained by US and MRI were compared, as well as prostate volumes obtained by US imaging, MRI, or histology.

4.1 | PD tumor screening

Stratification of mice into different treatment groups based on the disease phenotype is important to reduce variation in treatment response within treatment groups and to reduce the number of mice needed in preclinical trials. US imaging every third week, up to three times in total, was found to detect PD tumors in mice aged 16 to 24 weeks with 81% sensitivity and 91% specificity, demonstrating that US imaging can be a valuable tool for detecting PD tumors. For the false-negative cases, the volumes were too small for detection by US imaging and the validation with MRI performed 3 weeks later revealed volumes in the range of 21 to 93 mm³. Thus, at the time of US imaging, the tumors were most likely below 2 mm in diameter.

Misclassification of prostates as false positives occurred because the TRAMP prostate and PD tumors sometimes share characteristics, for example, compression can make the prostate appear spherical and a tilted image plane can make the prostate appear asymmetrical.

The screening performance could be improved by repeating US weekly. Wirtzfeld et al²⁰ achieved a sensitivity of 95% and specificity of 100% when screening 33 mice from the spontaneous PCa model PSP-TGMAP with US imaging weekly from 16 to 32 weeks of age. In that study, three investigators reached consensus over the presence or absence of tumors while having previous imaging data available. Together with the higher frequency of imaging sessions compared with our study, this led to an improved screening performance. Other factors that can contribute to the difference are the use of a different mouse model, different US set-up and fewer mice in the Wirtzfeld study. A limitation of both our and Wirtzfeld's study is that negative US screenings were not immediately validated by MRI or histology. In our study, mice with negative US screening were screened up to three times before validation and in Wirtzfeld's study, they were screened even more often.

The smallest tumor we detected at week 17 during US screening had a volume of 14 mm³ measured on MRI and a maximum diameter of 2.6 mm on US, which was similar to the study by Wirtzfeld who reported tumor detection down to 2.4 mm. Degraasi et al⁹ detected PD tumors with a diameter of 1 to 2 mm using MRI from week 12 of age, and the tumor doubling time for the PD tumors was 5 days, consistent with the doubling times in our study which were from 4.0 to 5.8 days. Several factors can influence the detection limit for PD tumors. In addition to tumor volume, the detection limit will depend on how close to the skin the tumor is located, if the tumor affects image symmetry and the tumor contrast to surrounding tissue.

When determining the mouse age at the start of screening and intervals between screening, important considerations are mouse age at PD tumor debut and PD tumor growth rate as well as the aim of the study to be performed. If a study requires small initial PD tumor volumes or one wants to follow tumor development closely, screening should start early (eg, at 16 weeks of age) and occur frequently (for example weekly). If the goal is to separate PD tumor mice from a population of TRAMP mice without tumors, screening can start later and be done less frequently. Knowledge of the tumor growth rate for a particular TRAMP strain might be used to extrapolate the growth curve to determine the start of screening and screening frequency to select mice with PD tumors of a certain volume.

4.2 | PD tumor measurement agreement and IOV

The repeatability of the volume measurements depends on the ROI placement around the tumor, which depends on how distinct the border between the tumor and surrounding tissue is. During US imaging, compression was used to improve the contrast between tissues and make borders more distinct, especially for tumors smaller than 3 mm in diameter. Large tumors often show a mass effect, compressing the tissue around it, giving a good contrast on US imaging without external compression. The agreement between US imaging and MRI was low, and the mean difference between measurements was 22% smaller with US imaging. Compression during US imaging could change the shape of the tumor, causing an apparent smaller volume especially for the smaller tumors where compression was done more often. Linxweiler et al²¹ compared US and MRI estimated volumes for orthotopic prostate tumors and they also found that US imaging resulted in smaller volumes than obtained by MRI. Their US measurements were on average 4.85 mm³ smaller than the MRI measurements and the limits of agreement were around -120 and 120 mm³.²¹ If we report our findings in absolute values rather than relative, they are very comparable to Linxweiler with a bias of 6.2 mm³ and limits of agreement from -122 to 120 mm³ (Figure S2). We quantified the difference with relative values instead of absolute values, since the variation depends on the tumor size and limits of agreement based on absolute values will be more dependent on larger tumors. In addition, one of the main benefits of using *in vivo* imaging is the longitudinal measurements quantify changes over time, which is a relative measurement, making relative measurements more relevant than absolute values.

The IOV for tumor volume estimation was slightly lower for MRI than US. The slightly better IOV for MRI could be because of a more distinct border and stronger contrast between tumor and the surrounding tissue compared with US imaging. This variation in measurement should be considered when estimating the number of animals needed for a study.

4.3 | Prostate volume measurement agreement and IOV

Prostate volumes were estimated by US imaging, MRI and histology. This is to our knowledge the first time a study comparing the three

methods has been performed in TRAMP mice. We included the ventral, lateral, and dorsal prostate lobes in the volume estimate, since the TRAMP mutation affects all prostate lobes. The anterior lobe was not included in the volume estimate because it was hard to determine the extent of it by US imaging. Defining the ROI around the prostate in US and MR images can be difficult due to an unclear border between prostate lobes and surrounding tissue, especially between the dorsal prostate and the seminal vesicle. Volume estimates based on US imaging were 42% smaller than volumes estimated by histology and 54% smaller than volumes estimated from MRI. MRI and histology had a much better agreement. Compression during US imaging could have been a contributing factor for the low agreement between volumes obtained by US imaging and the other methods. During compression, the prostate changes shape and parts of it could have moved out of the imaged volume. The prostate volume measured by histology is expected to be less than volumes measured *in vivo*, because of shrinking during tissue fixation and subsequent tissue processing. The degree of shrinkage depends on both tissue and the processing steps. In kidney and prostate tumors some authors have reported a mean volumetric shrinkage of 11.4% and 12.4%, respectively.^{22,23} This is in good agreement with the 12.4% difference we observed between volumes measured by MRI and histology. Prostate volume IOV was generally high, especially for US imaging. The border between dorsal prostate and seminal vesicles was least clear on US imaging (Figure S3) due to low contrast between the dorsal prostate and seminal vesicles. In addition, the bladder and preputial glands occasionally affected image contrast due to posterior acoustic enhancement. These factors make the transition from dorsal prostate to seminal vesicle a complex area where the placement of ROIs can be difficult and hard to reproduce. Our results indicate that the superior parts of the dorsal prostate may have been mistaken for seminal vesicles and thus were not included in the prostate ROI. While US imaging is relatively fast and cost-effective, the high IOV makes it less reliable for repeatable volume measurements than MRI. Therefore, a trade-off has to be made between the time-cost and reliability of measurements.

5 | CONCLUSIONS

US imaging was found to be a useful screening method for detecting PD tumors in the TRAMP model and for estimating PD tumor volume. MR imaging has better repeatability than US, especially for the estimation of prostate volumes and may be more suitable as a treatment monitoring method than US imaging.

ACKNOWLEDGMENTS

Animals were housed at the comparative medicine core facility, magnetic resonance imaging data were acquired at the MR core facility and histology was performed at the cellular and molecular imaging (CMIC) core facility, all at NTNU. The project is supported by the Research

Council of Norway (Project number: 240316), the Norwegian Cancer Society (Project number: 6824920-20156824920-2015), The liaison committee between the Central Norway Regional Health Authority and NTNU; (Project number: 90059700).

CONFLICT OF INTERESTS

The authors declare that there are no conflict of interests.

ORCID

Stein-Martin T. Fagerland  <http://orcid.org/0000-0002-1159-5922>
 Deborah K. Hill  <http://orcid.org/0000-0002-6441-5489>
 Annemieke van Wamel  <http://orcid.org/0000-0002-4704-2203>
 Catharina de Lange Davies  <http://orcid.org/0000-0003-4371-5025>
 Jana Kim  <http://orcid.org/0000-0003-4386-440X>

REFERENCES

- Ferlay J, Colombet M, Soerjomataram I, et al. Cancer incidence and mortality patterns in Europe: estimates for 40 countries and 25 major cancers in 2018. *Eur J Cancer*. 2018;103:356-387.
- Gengenbacher N, Singhal M, Augustin HG. Preclinical mouse solid tumour models: status quo, challenges and perspectives. *Nat Rev Cancer*. 2017;17:751-765.
- Ittmann M, Huang J, Radaelli E, et al. Animal models of human prostate cancer: the consensus report of the New York meeting of the mouse models of Human Cancers Consortium Prostate Pathology Committee. *Cancer Res*. 2013;73:2718-2736.
- Kido LA, de Almeida Lamas C, Marostica MR Jr, Cagnon VHA. Transgenic adenocarcinoma of the mouse prostate (TRAMP) model: a good alternative to study PCa progression and chemoprevention approaches. *Life Sci*. 2019;217:141-147.
- Gingrich JR, Barrios RJ, Morton RA, et al. Metastatic prostate cancer in a transgenic mouse. *Cancer Res*. 1996;56:4096-4102.
- Kaplan-Lefko PJ, Chen TM, Ittmann MM, et al. Pathobiology of autochthonous prostate cancer in a pre-clinical transgenic mouse model. *Prostate*. 2003;55:219-237.
- Berman-Booty LD, Sargeant AM, Rosol TJ, et al. A review of the existing grading schemes and a proposal for a modified grading scheme for prostatic lesions in TRAMP mice. *Toxicol Pathol*. 2012;40:5-17.
- Hill DK, Kim E, Teruel JR, et al. Diffusion-weighted MRI for early detection and characterization of prostate cancer in the transgenic adenocarcinoma of the mouse prostate model. *J Magn Reson Imaging*. 2016;43:1207-1217.
- Degrassi A, Russo M, Scanziani E, et al. Magnetic resonance imaging and histopathological characterization of prostate tumors in TRAMP mice as model for pre-clinical trials. *Prostate*. 2007;67:396-404.
- Gingrich JR, Barrios RJ, Foster BA, Greenberg NM. Pathologic progression of autochthonous prostate cancer in the TRAMP model. *Prostate Cancer Prostatic Dis*. 1999;2:70-75.
- Suttie A, Nyska A, Haseman JK, Moser GJ, Hackett TR, Goldsworthy TL. A grading scheme for the assessment of proliferative lesions of the mouse prostate in the TRAMP model. *Toxicol Pathol*. 2003;31:31-38.
- Shappell SB, Thomas GV, Roberts RL, et al. Prostate pathology of genetically engineered mice: definitions and classification. The consensus report from the Bar Harbor meeting of the Mouse Models of Human Cancer Consortium Prostate Pathology Committee. *Cancer Res*. 2004;64:2270-2305.
- Chiaverotti T, Couto SS, Donjacour A, et al. Dissociation of epithelial and neuroendocrine carcinoma lineages in the transgenic adenocarcinoma of mouse prostate model of prostate cancer. *Am J Pathol*. 2008;172:236-246.
- Søgaard CK, Moestue SA, Rye MB, et al. APIM-peptide targeting PCNA improves the efficacy of docetaxel treatment in the TRAMP mouse model of prostate cancer. *Oncotarget*. 2018;9:11752-11766.
- Arbab AS, Shankar A, Varma NR, et al. MRI to assess chemoprevention in transgenic adenocarcinoma of mouse prostate (TRAMP). *BMC Med Imaging*. 2011;11:21.
- Oliveira DS, Dzinic S, Bonfil AI, Saliganan AD, Sheng S, Bonfil RD. The mouse prostate: a basic anatomical and histological guideline. *Bosn J Basic Med Sci*. 2016;16:8-13.
- Bland JM, Altman DG. Statistical methods for assessing agreement between two methods of clinical measurement. *The Lancet*. 1986;327:307-310.
- Giavarina D. Understanding Bland Altman analysis. *Biochem Med*. 2015;25:141-151.
- Greenberg NM, DeMayo F, Finegold MJ, et al. Prostate cancer in a transgenic mouse. *Proc Natl Acad Sci*. 1995;92:3439-3443.
- Wirtzfeld LA, Wu G, Bygrave M, et al. A new three-dimensional ultrasound microimaging technology for preclinical studies using a transgenic prostate cancer mouse model. *Cancer Res*. 2005;65:6337-6345.
- Linxweiler J, Körbel C, Müller A, et al. A novel mouse model of human prostate cancer to study intraprostatic tumor growth and the development of lymph node metastases. *Prostate*. 2018;78:664-675.
- Tran T, Sundaram CP, Bahler CD, et al. Correcting the shrinkage effects of formalin fixation and tissue processing for renal tumors: toward standardization of pathological reporting of tumor size. *J Cancer*. 2015;6:759-766.
- Schned AR, Wheeler KJ, Hodorowski CA, et al. Tissue-shrinkage correction factor in the calculation of prostate cancer volume. *Am J Surg Pathol*. 1996;20:1501-1506.

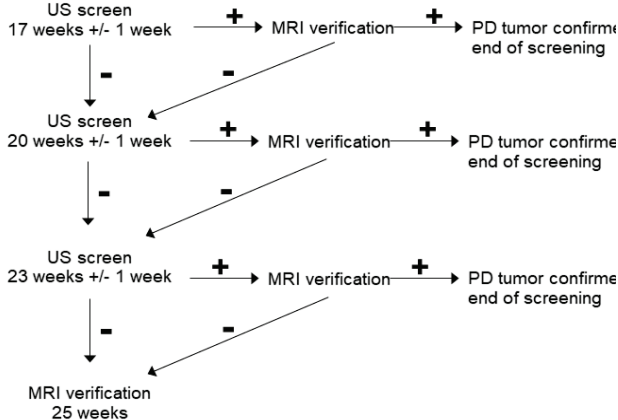
SUPPORTING INFORMATION

Additional supporting information may be found online in the Supporting Information section.

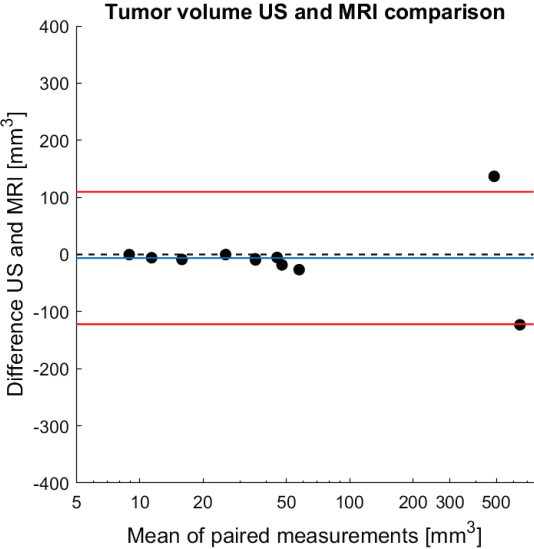
How to cite this article: Fagerland S-MT, Hill DK, van Wamel A, de Lange Davies C, Kim J. Ultrasound and magnetic resonance imaging for group stratification and treatment monitoring in the transgenic adenocarcinoma of the mouse prostate model. *The Prostate*. 2019;1-12.
<https://doi.org/10.1002/pros.23930>

Supporting information

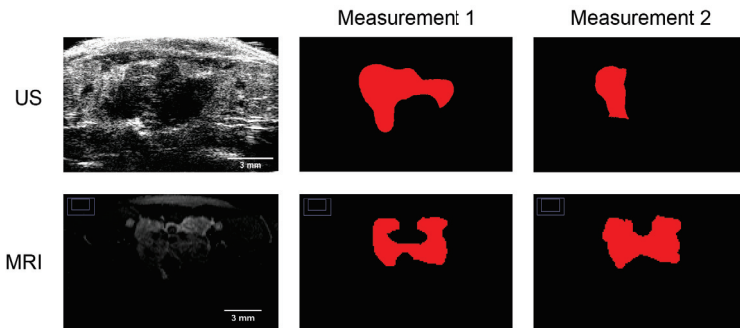
Flow chart PD tumor screening



Supplemental figure 1. Flow chart showing when ultrasound (US) and magnetic resonance imaging (MRI) examinations were performed. '+' indicates a poorly differentiate (PD) tumor positive examination and '-' indicates a PD tumor negative examination.



Supplemental figure 2: Poorly differentiated (PD) tumor volume comparison between ultrasound (US) imaging and MRI in absolute values. The blue line shows the mean of the differences and the red line the limits of agreement. Values are: Bias: -6.2 mm³, SD 59.1 mm³ (corrected for repeated measurements). Limits of agreement were from -122 to 110 mm³.



Supplemental figure 3: The top row shows an ultrasound (US) image of the prostate and regions of interest (ROIs) from two different sessions. The imaged area is close to the border between the dorsal prostate and the seminal vesicle and illustrate difficulty in repeating ROI placement. The bottom row shows the corresponding MR image and ROIs.

Table 1: US compared to MRI PD tumor volume

Tumor	US mean	MRI mean	Mean	Difference	Diff/mean%
1	31.7	39.3	35.5	-7.7	-21.6
2	8.5	14.3	11.4	-5.8	-50.5
3	25.6	25.7	25.6	-0.2	-0.6
4	555.5	418.8	487.1	136.8	28.1
5	11.6	20.2	15.9	-8.7	-54.5
6	38.5	56.7	47.6	-18.2	-38.3
7	44.1	70.7	57.4	-26.6	-46.3
8	8.8	9.0	8.9	-0.2	-2.2
9	42.5	47.7	45.1	-5.2	-11.5
10	585.1	708.2	646.6	-123.1	-19.0
11	30.8	40.3	35.6	-9.5	-26.7

Table 2: US PD tumor volume IOV

Tumor	Measurement1	Measurement2	Mean	Difference	Diff/mean%
1	33.7	29.6	31.7	4.1	13.0
2	8.9	8.1	8.5	0.8	9.4
3	26.5	24.6	25.6	1.9	7.4
4	549.1	561.9	555.5	-12.8	-2.3
5	10.8	12.3	11.6	-1.5	-13.0
6	39.4	37.5	38.5	1.9	4.9
7	45.6	42.6	44.1	3.0	6.8
8	8.9	8.7	8.8	0.2	2.3
9	42.0	42.9	42.5	-0.9	-2.1
10	583.0	587.1	585.1	-4.1	-0.7
11	31.3	30.3	30.8	1.0	3.2

Table 3: MRI PD tumor volume IOV

Tumor	Measurement1	Measurement2	Mean	Difference	Diff/mean%
1	37.2	41.4	39.3	-4.2	-10.7
2	13.9	14.6	14.3	-0.7	-4.9
3	26.3	25.1	25.7	1.2	4.7
4	419.6	417.9	418.8	1.7	0.4
5	20.5	19.9	20.2	0.6	3.0
6	56.7	56.6	56.7	0.1	0.2
7	70.9	70.4	70.7	0.5	0.7
8	9.5	8.5	9.0	1.0	11.1
9	47.0	48.3	47.7	-1.3	-2.7
10	695.7	720.6	708.2	-24.9	-3.5
11	40.5	40.1	40.3	0.4	1.0

Table 4. Ultrasound compared to MRI prostate volume

Mouse	US mean	MRI mean	Mean	Difference	Diff/mean%
1	44.2	62.0	53.1	-17.8	-33.4
2	39.9	73.6	56.7	-33.7	-59.3
3	41.8	63.7	52.7	-21.9	-41.4
4	41.2	89.7	65.5	-48.5	-74.1
5	34.3	79.2	56.7	-44.9	-79.1
6	50.6	73.2	61.9	-22.6	-36.5
7	35.6	60.6	48.1	-25.0	-52.0
8	29.2	46.4	37.8	-17.2	-45.5
9	28.0	42.3	35.2	-14.3	-40.7
10	23.4	35.8	29.6	-12.5	-42.1
11	19.9	49.5	34.7	-29.6	-85.3

Table 5. Ultrasound compared to histology prostate volume

Mouse	US mean	Histology mean	Mean	Difference	Diff/mean%
1	44.2	47.6	45.9	-3.4	-7.4
2	39.9	63.1	51.5	-23.2	-45.0
3	41.8	59.4	50.6	-17.6	-34.8
4	41.2	71.9	56.5	-30.7	-54.2
5	34.3	59.6	47.0	-25.3	-53.9
6	50.6	62.5	56.5	-11.9	-21.1
7	35.6	51.2	43.4	-15.7	-36.1
8	29.2	44.6	36.9	-15.4	-41.7
9	28.0	40.3	34.2	-12.3	-36.0
10	23.4	32.4	27.9	-9.0	-32.3
11	19.9	57.2	38.5	-37.3	-96.7

Table 6. MRI compared to histology prostate volume

Mouse	MRI mean	Histology mean	Mean	Difference	Diff/mean%
1	62.0	47.6	54.8	14.4	26.2
2	73.6	63.1	68.3	10.5	15.4
3	63.7	59.4	61.5	4.3	6.9
4	89.7	71.9	80.8	17.9	22.1
5	79.2	59.6	69.4	19.6	28.2
6	73.2	62.5	67.8	10.7	15.8
7	60.6	51.2	55.9	9.3	16.7
8	46.4	44.6	45.5	1.8	4.0
9	42.3	40.3	41.3	2.0	4.8
10	35.8	32.4	34.1	3.5	10.1
11	49.5	57.2	53.3	-7.7	-14.3

Table 7: Ultrasound prostate volume IOV

Mouse	Measurement1	Measurement2	Mean	Difference	Diff/mean%
1	53.6	34.8	44.2	18.8	42.5
2	34.2	45.6	39.9	-11.4	-28.6
3	37.0	46.6	41.8	-9.6	-23.0
4	47.4	35.0	41.2	12.4	30.1
5	34.8	33.8	34.3	1.0	2.9
6	55.8	45.3	50.6	10.5	20.8
7	42.0	29.1	35.6	12.9	36.3
8	31.5	26.9	29.2	4.6	15.8
9	28.9	27.1	28.0	1.8	6.4
10	23.7	23.0	23.4	0.7	3.0
11	19.6	20.2	19.9	-0.6	-3.0

Table 8: MRI prostate volume IOV

Mouse	Measurement1	Measurement2	Mean	Difference	Diff/mean%
1	56.5	67.4	62.0	-10.9	-17.6
2	74.1	73.0	73.6	1.1	1.5
3	66.6	60.7	63.7	5.9	9.3
4	97.4	82.0	89.7	15.4	17.2
5	78.1	80.2	79.2	-2.1	-2.7
6	72.2	74.1	73.2	-1.9	-2.6
7	55.1	66.0	60.6	-10.9	-18.0
8	48.3	44.5	46.4	3.8	8.2
9	40.5	44.1	42.3	-3.6	-8.5
10	33.6	38.0	35.8	-4.4	-12.3
11	50.3	48.7	49.5	1.6	3.2

Table 9: Histology prostate volume IOV

Mouse	Measurement1	Measurement2	Mean	Difference	Diff/mean%
1	47.3	47.9	47.6	-0.6	-1.3
2	62.7	63.4	63.1	-0.7	-1.1
3	59.3	59.5	59.4	-0.2	-0.3
4	72.8	70.9	71.9	1.9	2.6
5	50.0	69.2	59.6	-19.2	-32.2
6	58.0	66.9	62.5	-8.9	-14.3
7	49.7	52.7	51.2	-3.0	-5.9
8	42.8	46.4	44.6	-3.6	-8.1
9	40.5	40.1	40.3	0.4	1.0
10	32.9	31.8	32.4	1.1	3.4
11	60.9	53.4	57.2	7.5	13.1

Paper III

Nanoparticle and ultrasound mediated delivery of chemotherapy in the transgenic adenocarcinoma of the mouse prostate (TRAMP) model

Stein-Martin T. Fagerland^{1,2}, Sigrid Berg^{2,4,5}, Deborah K. Hill², Sofie Snipstad^{1,3,5}, Einar Sulheim^{1,3,5}, Astrid Hyldbakk^{1,3}, Jana Kim², Catharina de Lange Davies¹

¹Department of Physics, Norwegian University of Science and Technology, Trondheim, Norway

²Department of Circulation and Medical Imaging, Norwegian University of Science and Technology, Trondheim, Norway

³Department of Biotechnology and Nanomedicine, SINTEF Industry, Trondheim, Norway

⁴Department of Health Research, SINTEF Digital, Trondheim, Norway

⁵Cancer Clinic, St. Olavs Hospital, Trondheim, Norway

Abbreviations

Cab – cabazitaxel

Cab-US+MB - cabazitaxel combined with therapeutic ultrasound and microbubbles

Ctrl – control

DD – ductus deference

HES - hematoxylin, erythrosine and saffron

IHC – immunohistochemistry

MRI – magnetic resonance imaging

MS – mass spectrometry

NE - neuroendocrine

NP – nanoparticle

Pr - prostate

PBS – phosphate-buffered saline

PD – poorly differentiated

PEBCA – poly (2-ethyl-butyl cyanoacrylate)

PIN - prostatic intraepithelial neoplasia

SV – seminal vesicle

TRAMP – transgenic adenocarcinoma of the mouse prostate

Tu – tumor

Ur - urethra

US – ultrasound

US+MB – therapeutic ultrasound combined with microbubbles (SonoVue)

Abstract

Both nanoparticle (NP) and ultrasound (US) mediated drug delivery of chemotherapeutic agents have shown promising results in pre-clinical and clinical studies. Until now, most pre-clinical studies have been done in immunodeficient mice with xenografted tumors. In this study, we used two phenotypes of the spontaneous model transgenic adenocarcinoma of the mouse prostate (TRAMP) and followed treatment response with magnetic resonance imaging. TRAMP mice with poorly differentiated (PD) tumors (n=12) detected by US imaging were treated with either the chemotherapeutic agent cabazitaxel (Cab), Cab combined with therapeutic US and microbubbles (MBs) or were untreated controls treatment. Cab reduced the volume of all tumors, but an additional effect from US+MB was not detected; one mouse, however, did not show sign of tumor recurrence. TRAMP mice with dysplastic prostates (n=47) were treated with either Cab, Cab combined with therapeutic US and microbubbles (MBs), NPs encapsulating Cab, NPs encapsulating Cab combined with therapeutic US and microbubbles (MBs) or were untreated controls. All treatments reduced the mean prostate volume compared to the control and to the volume before treatment. However, the prostates started growing again after treatment, and six weeks after treatment the mean prostate volume was similar between groups. Also, histology grading and Ki-67 immunostaining did not reveal difference between groups. Mass spectrometry analysis showed that NP encapsulation of Cab increased the circulation time of Cab and enhanced the accumulation in the liver and the spleen. Overall, Cab reduced PD tumor and prostate volume in the TRAMP model, but the effect was transient. The study did not show any clear added therapeutic efficacy from combining Cab with NP encapsulation or US+MB.

Introduction

Prostate cancer is the third most deadly cancer among men in the European Union with an estimated 107,300 deaths in 2018¹. Thus, more efficient therapies are needed to improve prostate cancer survival. Nanoparticles (NPs) and ultrasound combined with microbubbles (US+MB) are promising methods to increase the delivery and efficacy of chemotherapeutic drugs. By encapsulating drugs in NPs, the pharmacokinetic properties can be altered to improve efficacy and reduce adverse effects². NPs have shown promising results in pre-clinical studies³ and are thought to improve treatment through the enhanced permeability and retention effect (EPR effect), where NPs passively target tumors due to leaky tumor capillaries and are retained there because of the lack of effective lymphatic drainage⁴. However, a review of studies has shown that a median of only 0.7% injected NPs reaches the tumor⁵. Further methods to improve drug delivery are therefore needed. US+MB mediated drug delivery is known under many terms, including sonopermeation⁶. Sonopermeation effects are mediated by acoustic radiation force, which causes a fluid stream in the direction of the US pulse, and cavitation, which is the creation and oscillation of bubbles in the acoustic field. This might lead to changes in tumor perfusion, enhanced vascular permeability and facilitated transport of drugs through the extracellular matrix towards cancer cells. US+MB mediated drug delivery has increased drug efficacy in both pre-clinical and clinical studies⁶.

Most preclinical studies of the treatment efficacy of drug-loaded NPs alone or combined with US+MB have been conducted in immunodeficient xenograft cancer models in mice, which differ from human cancer in several regards: the tumor develops from cells that are already malignant, leading to less heterogenous cancer genetics; the mice are immunodeficient, thus diminishing the anti-cancer role of the immune system, and the cancer cells are often grown outside of their tissue of origin, preventing interplay between the cancer cells and the organ specific connective tissue⁷. The use of genetically engineered cancer models can address these shortcomings. The transgenic adenocarcinoma of the mouse prostate (TRAMP) is a commonly used spontaneous prostate cancer model where cancer develops from normal prostate cells that transition through dysplastic stages before they become malignant^{8,9}. The TRAMP model has mainly been used to examine cancer preventive effects of interventions, ranging from the efficacy of diets¹⁰ and supplements of silibinin¹¹ or selen¹², to some types of drugs, for example non-steroidal anti-inflammatory drugs¹³ and tyrosine kinase inhibitors¹⁴. In studies of cancer prevention, the treatment is administered from early in life, before the onset of cancer. Studies of anti-cancer efficacy should however start later in life, once the disease has developed. Some studies have examined the anti-cancer effect of chemotherapeutic agents^{15,16} in the TRAMP model, but as far as we know no studies have assessed the therapeutic effect of using NPs or sonopermeation for drug delivery in the TRAMP model.

In this study, we investigated if NP encapsulation and US+MB could enhance the therapeutic efficacy of cabazitaxel (Cab) in two phenotypes of the TRAMP model. In the TRAMP model, a subgroup develops poorly differentiated (PD) tumors, whereas the majority develop a dysplastic prostate with a high grade of prostatic intraepithelial neoplasia (PIN). The therapeutic response was thus evaluated either by the volume of the tumor (PD group) or by the volume of the prostate (PIN group). In addition, the effect of NP encapsulation and US+MB on biodistribution of Cab was assessed using mass spectrometry (MS). To our knowledge, this is the first time a study is conducted in the TRAMP model using Cab and NP-encapsulated Cab alone or in combination with US+MB.

Materials and Methods

Animal model

All animal experiments were approved by the Norwegian Food Safety Authority. TRAMP mice were purchased from Jackson Labs in 2012 and used to establish an in-house colony at the Norwegian University of Science and Technology (NTNU, Trondheim, Norway). Mice heterozygous for the TRAMP mutation were bred using homozygous females from the in-house colony and C57BL6 males purchased from Jackson Labs. The presence of TRAMP mutation was verified using polymerase chain reaction. Mice were housed under specific pathogen-free conditions, in groups of one to six in individually ventilated cages (Model 1284 L, Tecniplast, Lyon, France) at temperatures from 21°C–23°C, with 45–60% relative humidity, 70 air changes per hour, 12 h light/dark cycle and ad libitum access to food and sterile water. They were fed RM1 expanded pellets (Special Diets Services) and the cages were enriched with housing, nesting material and gnaw sticks. Approximately 20% of the TRAMP mice bred in a C57BL6 background strain develop fast growing PD tumors¹⁷, and these mice need to be euthanized few weeks after PD tumor detection because of tumor burden, while TRAMP mice with dysplastic prostate without tumors can live up to 52 weeks¹⁸. Mice were euthanized if they were moribund, displayed signs of excessive scratching, had a weight loss >10% or a tumor diameter >15 mm.

Ultrasound imaging and screening

To separate the TRAMP mice with fast growing PD tumors from the mice with a dysplastic prostate, the mice were screened with US imaging as described earlier¹⁷. Imaging was performed with a FUJIFILM Visualsonics Vevo 3100 scanner and an MX550D probe with 40 MHz center frequency, giving a 30x30 μm^2 in-plane resolution and 80 μm through-plane resolution. 3D images were acquired by imaging every 76 μm using a 3D motor. Mice were anesthetized with 1.5% to 2.5% isoflurane with 0.5 L/min 5:1 air:O₂ mix. The isoflurane dose was adjusted to reach a target respiratory rate of 80 breaths per min. Mice were restrained in supine position by taping the hind limbs to the imaging stage. To remove fur, the mice were shaved with an electric razor followed by application of depilation creme. US imaging gel was used to secure good acoustic contact between the transducer and the mouse skin. Mice were screened one to three times at an age ranging from 16 to 24 weeks. If a PD tumor was detected with US, the mouse was imaged with MRI the following day to verify the findings, upon which, the mouse was treated the same week, or the week after if PD tumor volume was <30 mm³. The same MRI protocol was used for treatment monitoring and is described later.

Treatment groups

Mice with PD tumors were available in limited numbers and were divided into three treatment groups, examining the therapeutic effect of Cab and Cab combined with ultrasound and microbubbles (US+MB):

- 1) Control (Ctrl): No treatment.
- 2) Cabazitaxel (Cab): 10 mg/kg Cab once a week for three weeks.
- 3) Cab combined with US and MB (Cab-US+MB): 10 mg/kg Cab once a week for three weeks combined with US+MB.

Mice without PD prostate tumors were divided into five different groups, examining the therapeutic effect of Cab and NP with and without US+MB:

- 4) Control (Ctrl): No treatment.
- 5) Cabazitaxel (Cab): 10 mg/kg Cab once a week for three weeks.
- 6) Cab combined with US and MB (Cab-US+MB): 10 mg/kg Cab once a week for three weeks combined with US+MB.
- 7) Nanoparticles (NP): 10 mg/kg Cab encapsulated in NPs once a week for three weeks.
- 8) NP combined with US and MB (NP-US+MB). 10 mg/kg Cab encapsulated in NPs once a week for three weeks combined with US+MB.

Cabazitaxel and nanoparticles

Cab is approved as a second-line treatment in metastatic prostate cancer and is a good candidate for polymeric NP encapsulation as its high toxicity makes altered biodistribution and pharmacokinetics favorable. Cab (Biochempartner Co. Ltd.) was dissolved in distilled water with 1040 mg/mL Tween-80 (Sigma-Aldrich) to 40 mg/mL and stored at +4°C. At each day of experiment, Cab was diluted 1:4 in 13% ethanol and further diluted in 0.9% NaCl to reach a 6 mg/mL concentration before iv injection. PEGylated poly(2-ethyl-butyl cyanoacrylate) NPs loaded with Cab were synthesized as described previously¹⁹. Cab concentration in the NPs was measured by MS and NP solution was diluted in 0.9 % NaCl to a 6 mg/mL concentration of Cab, resulting in a NP concentration around 67 mg/mL in the injected volume of 41 to 62 μ L. Iv access was established by placing a 24G catheter (BD Neoflon, Becton Dickinson Infusion Therapy) in the tail vein.

MRI-guided ultrasound treatment

US treatment was done MRI guided, combining a FUS Instruments RK100 with a Bruker 7T Biospec 70/20 Avance III MRI scanner. The RK100 consists of a water tank containing a 3-axis positioning system with a US transducer and a control station with a PC, amplifier and a signal generator. Approximately 8 L of deionized water was filled in the water tank and heated to approximately 40°C to reduce the amount of dissolved gas in the water and avoid hypothermia during treatment. At each day of treatment, the spatial coordinates of the US system and the MRI scanner were co-registered for calibration following the instructions from the producer.

MRI scans were acquired before US treatment to localize the prostate or tumor and determine which areas to treat. These MRI images were acquired using an 86 mm volume resonator coil for both RF transmission and reception. Axial T2 weighted coronal images were acquired with settings TE 58.5 ms, TR 4000 ms, RARE factor 8, averages 6, in-plane resolution 0.2x0.2 mm², slice thickness 0.8 mm and acquisition time 6 minutes.

US treatment was done using a single-element spherically-curved transducer with resonance frequency 1.1 MHz, aperture 75 mm and focus at 60 mm. The US settings were peak negative pressure of 0.545 MPa, resulting in mechanical index ($=\text{peak negative pressure (MPa)} / \sqrt{\text{center frequency (MHz)}}$) of 0.5, 10k cycles and 3 minutes sonication time. Pulse repetition time varied depending on the area of tumor or prostate. In tumors, the mean number of treatment points were 10 with a range of 6 to 14, covering an area of 50 to 117 mm² (Figure 1 Left). The mean pulse repetition time was 2.8 s with range 1.8 to 3.5 s. When treating prostates, the mean number of treatment points was 15 with a range of 8 to 20 (Figure 1 Right), covering an area of 67 to 167 mm². The mean pulse repetition time was 3.8 s with range 2.2 to 4.8 s. All treatment points were selected at the same depth, since the axial pressure wave stayed within -6 dB over 8.18 mm, giving good coverage in the anterior-posterior direction. The US contrast agent SonoVue (Bracco) was used. Mice received an iv injection of 50 μ L SonoVue before each of three sonications, resulting in a total treatment time

of 9 min per week. The treatment was repeated weekly for three weeks. Figure 2 shows the treatment timeline for US+MB treatment sessions.

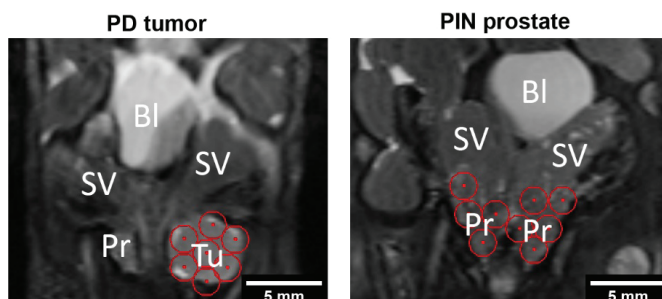


Figure 1.

MR images showing representative examples of placement of treatment areas for ultrasound treatment (red circles) on the PD tumors and PIN prostates. The individual treatments points are 1.63 mm in diameter, corresponding to the full width at half maximum for the radial pressure profile. Abbreviations: B, bladder; Pr, prostate; SV, seminal vesicle and Tu, tumor.

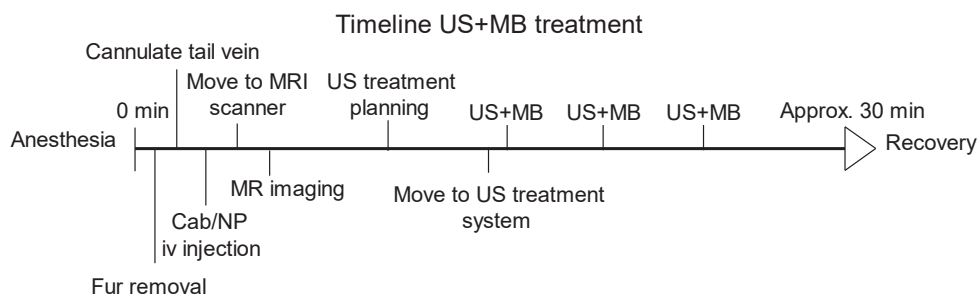


Figure 2.

Timeline showing the treatment steps involved in US+MB treatment. The treatment was repeated weekly for three weeks. Abbreviations: Cab, cabazitaxel; MRI, magnetic resonance imaging; NP, nanoparticle; US+MB, ultrasound combined with microbubbles. iv, intravenous

Treatment monitoring

The treatment response was monitored by measuring PD tumor volume or prostate volume with MRI. Imaging was done using a Bruker 7T Biospec 70/20 Avance III scanner with an 86 mm volume resonator coil for RF transmission, and a phased array mouse heart surface coil was placed close to the lower abdomen for RF reception. Axial T2 weighted images were acquired with settings TE 58.5 ms, TR 5000 ms, RARE factor 6, averages 6, in-plane resolution 0.1 x 0.1 mm², slice thickness 0.4 mm and acquisition time 10 minutes. Mice were kept under isoflurane gas anesthesia and were placed on the scanner bed in prone position with a gauze and tape over the lower back to reduce motion from breathing. Mice with PD tumors were imaged weekly and mice with PIN prostate were imaged every other week. MRI

images were exported as DICOM from Paravision 6.0.1 and loaded into FIJI ImageJ²⁰ where volumes were estimated based on manual segmentation of the image stacks. The ventral, lateral and dorsal prostate lobes were included in the segmentation. The anterior prostate lobe was not included since it is hard to differentiate from the seminal vesicle because of their intertwined relationship. Sogaard et al. also choose to leave out the anterior lobe¹⁶.

Histology and immunohistochemistry

For a subgroup of mice without PD tumors, the treatment effect was also assessed by histology and immunohistochemistry. 30 mice were included in the analysis, three per treatment group and the analysis was performed at two time points, two and six weeks after end of treatment. Mice were euthanized by cervical dislocation and prostates harvested together with the seminal vesicle, bladder and urethra and fixed in 4% formaldehyde before paraffin embedding. Sectioning was done with a microtome (Leica RM2255) and the sections were stained for hematoxylin, erythrosine and saffron (HES) or the proliferation marker Ki-67 with a light hematoxylin counterstain.

Ki-67 staining was done using a Dako Autostainer. Sections were incubated with anti-Ki67 antibody (Abcam ab16667, clone SP6 1:50) for 40 minutes. After a rinse, the sections were washed in buffer and incubated for 30 minutes in Labelled polymer HRP anti-Rabbit (Dako K4003) and with DAB (Dako K3468) to develop the stain. In Sakura Tissue-Tek © Prisma™, the slides were lightly counterstained with hematoxylin. The stained sections were digitalized using a slide microscope (Olympus VS120-S5). The proliferative index (PI) was quantified as the percentage of cells positive for Ki-67 marker and was calculated using QuPath software²¹. Regions of interest were drawn over separate prostate lobes and the number of Ki-67 positive cells were found using the positive cell detection function. The prostates were fixed preserving the whole structure which made it hard to find the transition between dorsal and anterior lobe when the PIN was high grade. Because of this, the inferior part of the dorsal lobe was used to score the dorsal lobe and the anterior lobe was left out from HES and Ki-67 quantification.

HES sections were graded using the TRAMP grading scheme by Berman-Booty²². This grading scheme was chosen since the output is quantitative. The scheme grades lesions based on seven levels of severity (normal, three grades of PIN, phyllodes tumor and three grades of malignancy) and distribution (focal, multifocal or diffuse). The score is the sum of the most severe lesion and the most common lesion. The grading scheme differentiates high-grade PIN from well-differentiated adenocarcinoma by the presence of invasion, which requires invasion of epithelial cells into underlying smooth muscle and reactive fibroblasts and myoepithelial cells in the area of invasion.

Biodistribution of cabazitaxel

MS quantification of Cab was performed to assess the effect of NP encapsulation and US+MB on the drug biodistribution. Twelve TRAMP mice in the age range from 25 to 28 weeks were included. Mice were imaged with US two days prior to the experiment to remove mice with PD tumors. The mice were exposed to a single treatment equivalent to groups 5, 6, 7 and 8, and euthanized two hours later. In order to only quantify Cab residing in the organ tissue and not include Cab content from the blood, all mice were perfused with phosphate-buffered saline (PBS). Euthanasia was done by first anesthetizing the mice with isoflurane and administering a lethal dose of pentobarbital intraperitoneally. After the mouse stopped breathing, the chest was opened, and a blood sample was collected from the right ventricle. Further, an incision was made in the right atrium. Then a catheter was used to puncture the left ventricle and perfuse the mouse with 10 mL PBS. After perfusion, the brain, heart, lung, liver, kidney, spleen, anterior prostate lobe, dorsolateral lobes and the ventral lobe were harvested and

frozen individually. Prostate lobes were separated using microdissection. All samples were lyophilized and weighted before and after lyophilization. The Cab content of the samples was extracted and quantified by MS as described earlier²³.

Toxicity

Iv NP injection led to instant apnea in all mice treated with NPs. Heart rate and respiration rate was monitored during and after iv injection of NP in four mice, using a Vevo3100 (Fujifilm Visualsonics) system. Body weight was recorded by weighing mice weekly during treatment and every other week after end of treatment.

Statistical analysis

A two-way mixed ANOVA was performed to evaluate if prostate volumes and body weights were significantly different between treatment groups. A p-value of 0.05 was considered to show statistical significance.

Results

TRAMP phenotype stratification

TRAMP mice were screened to distinguish between mice with and without PD tumors (Figure 3 shows representative images). 82 TRAMP mice were screened for PD tumors and 16 tumors were detected in the age range 17-25 weeks. Two of the mice were euthanized due to tumor burden at the time of PD tumor detection, and 14 of the mice with PD tumors were included in treatment groups 1-3. Mice without PD tumors were expected to have prostates displaying PIN. Among PIN mice, 21 mice were removed during the study because of kidney tumors, bad health, change in MRI measurement protocol after first treatment or complications from iv cannulation and injection. 45 mice with PIN prostates were included in treatment groups 4-8 and were treated and followed up as intended. Figure 4 shows time points where mice were removed from the study.

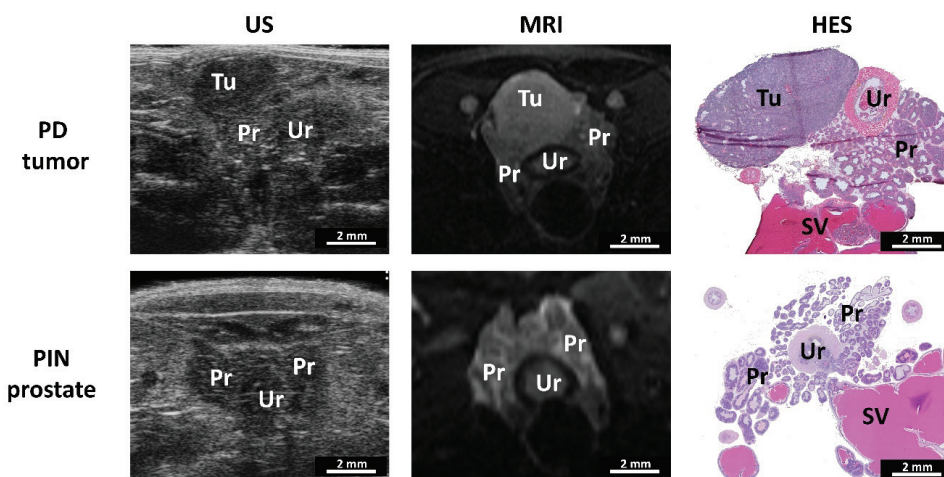


Figure 3.

The image panel shows representative images of PD prostate tumors (top row) and prostates with PIN (bottom row) acquired with US imaging (left column), MRI imaging (middle column) and HES slide (right column). Abbreviations: HES; hematoxylin, erythrosine and saffron, MRI; magnetic resonance imaging, PIN; prostatic intraepithelial neoplasia, PD; poorly differentiated, Pr; prostate, SV; seminal vesicle, Tu; tumor and Ur; urethra.

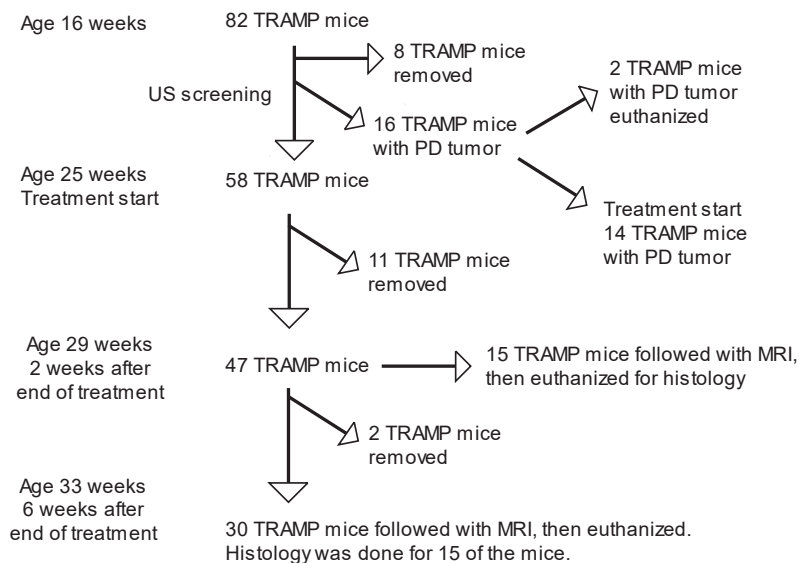


Figure 4.

Flow chart displaying recruitment of the two phenotypes of TRAMP mice to treatment studies. Fourteen mice with PD tumor and 45 mice with PIN prostate were treated and followed up as intended. Abbreviations: PD, poorly differentiated; TRAMP, transgenic adenocarcinoma of the mouse prostate and US, ultrasound.

Treatment effect on PD tumor volume

The therapeutic effect of Cab and Cab combined with US+MB was studied in TRAMP mice with PD tumors, and the tumor growth is presented in Figure 5. 12 out of 14 mice received all intended treatments. Mice were euthanized because of tumor burden (n=8), bad health (n=3) or air injection (n=1). For the untreated controls, all tumors had an approximately logarithmic growth in volume. For the Cab group, three of four tumors decreased in size following treatment, but regrowth took place two to six weeks after the last treatment. One tumor continued to grow despite treatment, but the growth rate was less than for the untreated controls. This tumor was approximately 4 times larger in volume compared to the other PD tumors at treatment start, which can explain the poor therapeutic response. In the US+MB group, all tumors decreased in size after treatment. One mouse survived for ten weeks after treatment without tumor recurrence (MR images shown in Figure 6). The PD tumor could not be detected by MRI, in contrast to the other mice, where PD tumors were still detectable. The mouse without recurrence was euthanized ten weeks after the end of treatment due to acute poor health. Necropsy revealed gut necrosis. Among the other mice receiving US+MB treatment one died during the last treatment because of unintended injection of air and another was euthanized due to weight loss 3 weeks after start of treatment.

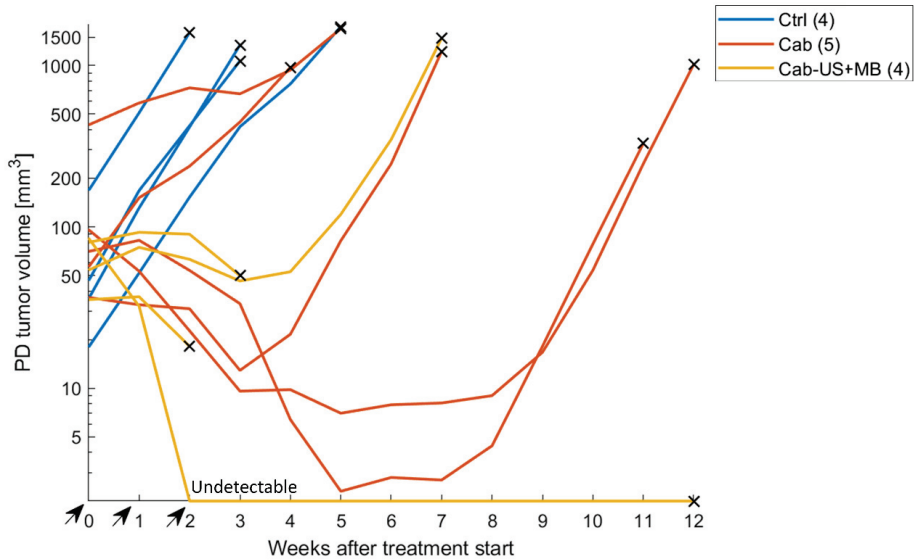


Figure 5.

Tumor volume in mm^3 on a logarithmic axis as a function of time after start of treatment. Treatment was given in week 0, 1 and 2 (marked with arrows). The colored lines show tumor growth for individual mice. Time of euthanasia is marked with a cross. Abbreviations: Ctrl, control; Cab, cabazitaxel; Cab-US+MB, cabazitaxel combined with therapeutic ultrasound and microbubbles

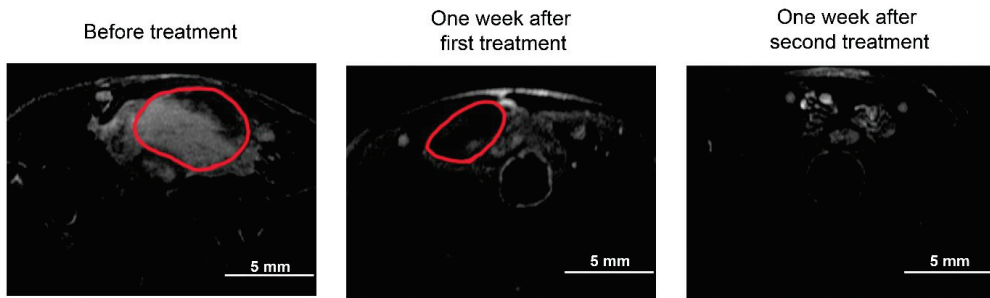


Figure 6.

The image panel shows weekly MR images of a mouse receiving weekly Cab and US+MB. In the left image, the tumor is seen as an oval structure with a mix of homogenous mid intensity area and a dark area in the periphery. One week after the first treatment the whole tumor structure has a low signal intensity and one week after the second treatment the dark structure is further reduced in size.

Treatment effect on prostate volume

The treatment efficacy of Cab, Cab-US+MB, Cab-loaded NP and Cab-loaded NP with US+MB was assessed by recording the prostate volume of 47 mice. Two weeks after end of treatment, the mean prostate volume was increased by 26% for the untreated control group and for all

treated mice the prostate volume was reduced by 16-18%. There was no significant difference between the different treatments. The prostate volume for all treated mice were significantly different from the untreated control group. 30 mice were followed up to six weeks after the last treatment (Figure 7). Between two and four weeks after treatment, the mean prostate volume increased in all groups, and the growth rate was faster than in the untreated control group. Six weeks after end of treatment, there was no difference between the mean prostate volume of the different groups. Large variations were observed between individual prostates, especially for the untreated controls (Supplementary Figure 1). For the untreated controls, the prostate volume increased rapidly for one mouse, increased slowly for most of the mice and decreased for two mice. The variation was less for the mice treated with Cab either free or encapsulated. The majority (except two given free Cab) of the prostates decreased in volume during treatment. For the prostates that were also treated with US+MB, the variation was even less, and all prostate volumes decreased during treatment.

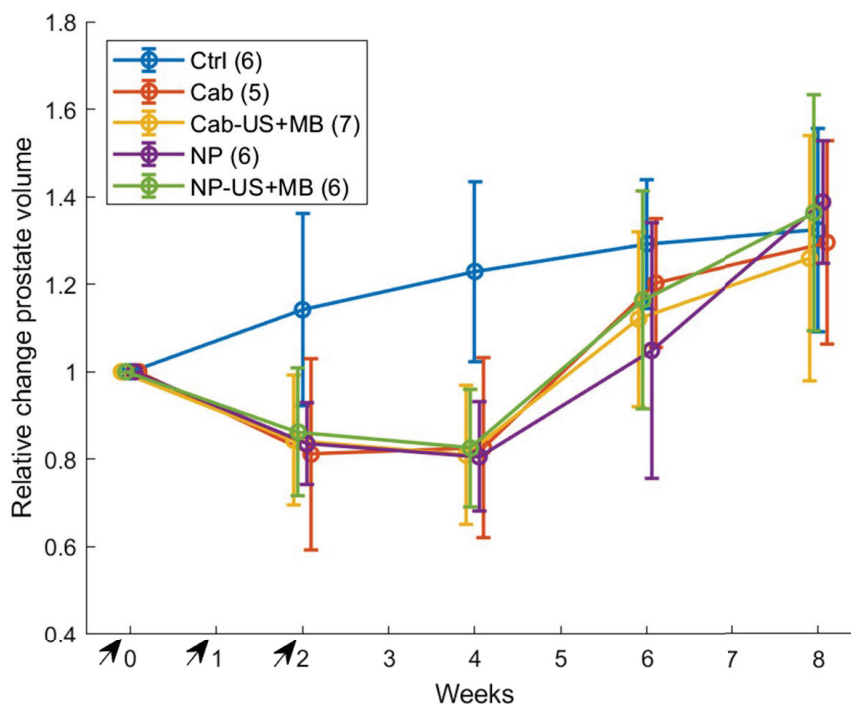


Figure 7.

Mice followed from before treatment until eight weeks after start of treatment. Relative prostate volume as a function of time after start of treatment. Treatment was given in weeks 0, 1 and 2 (marked with arrows). The colored symbols show group mean and the error bars show standard deviation. The number of animals per group are given in the figure legend. Abbreviations: Ctrl, control; Cab, cabazitaxel; Cab-US+MB, cabazitaxel combined with therapeutic ultrasound and microbubbles; NP, cabazitaxel encapsulated in nanoparticles and NP-US+MB, cabazitaxel encapsulated in nanoparticles combined with therapeutic ultrasound and microbubbles.

Treatment effect on prostate histology scoring and proliferative index

Mice without PD tumor were euthanized either two or six weeks after end of treatment and prostates were harvested for analysis. HES sections were graded with the scheme by Berman-Booty²² and the Ki-67 sections were quantified based on the percentage of positive cells. Figure 8 shows representative HES and Ki-67 staining of TRAMP prostates and details of the ventral, lateral and dorsal prostate lobe. On HES stained sections, the ventral prostate was characterized by multifocal low grade PIN and not much change in the stroma. The lateral and dorsal lobe expressed diffuse high grade PIN. The lateral lobe's connective tissue had fibroblast invasion and collagen fibers surrounding the lobes, while the dorsal lobe had hypertrophic smooth muscle cells surrounding the glands. Cells positive for Ki67 were typically epithelial cells located basally in the glands.

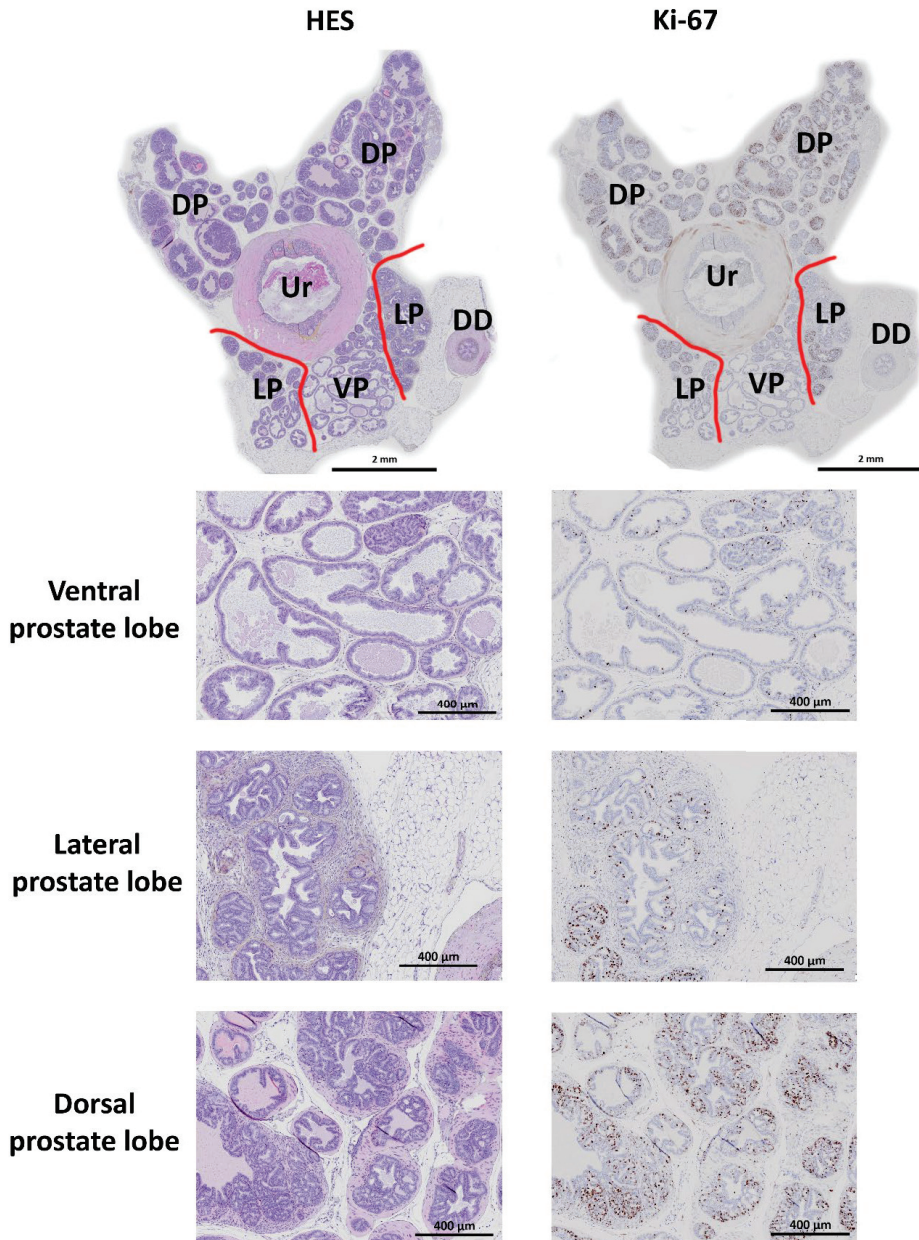


Figure 8.

The image panel shows HES stained sections in the column to the left and Ki-67 stained sections in the column to the right. The top row of images shows an overview of the prostate and the other rows show details of different prostate lobes. The images are representative of the most common lesions in the respective lobes: Multifocal low grade PIN in the ventral prostate lobe and diffuse high grade PIN in the lateral and dorsal prostate lobe. Abbreviations: DD, ductus deference; DP, dorsal prostate lobe; HES, hematoxylin, erythrosine and saffron; LP, lateral prostate lobe; VP, ventral prostate and Ur, urethra.

To obtain a quantitative number for the malignancy of the prostate, HES images were scored using the Berman-Booty grading scheme. The scores were similar between all groups and between the two time points (Figure 9), i.e. there was no clear difference between the treatment groups and untreated control. Most groups showed one prostate with higher or lower score than the majority. Only one sample was classified as malignant. This mouse was in the NP group and displayed PD tumor tissue in the ventral prostate, but the PD tumor was small and had not been detected during MR imaging. In general, the ventral prostates were homogenous, with most prostates scoring 8. This score was characterized by a multifocal distribution of cell stratification and crowding of epithelial cells. The lateral and dorsal prostate were especially homogenous, with most samples scoring 18, corresponding to a diffuse distribution of features like tall papillary projections filling the lumen and clusters of cells herniating into the surrounding smooth muscle.

The proliferative index was similar between all treatment groups (Figure 9) although there was a large variation within the groups. For the ventral and lateral prostate, the proliferative index was lower six weeks after treatment compared to two weeks after treatment. The ventral lobe showed lowest proliferative activity with 10-20% and 0-20% proliferative cells two and six weeks after treatment, respectively. Cells in the lateral and dorsal lobes had higher proliferative activity and the Ki-67 positive cells ranged from 0-50% or 10-60% in the lateral and dorsal lobe, respectively. Staining with the proliferation marker Ki-67 was quite homogenous in the ventral prostate lobe and heterogenous for the lateral and dorsal lobe, corresponding to larger variation in proliferative index in the lateral and dorsal lobes compared to the ventral lobe.

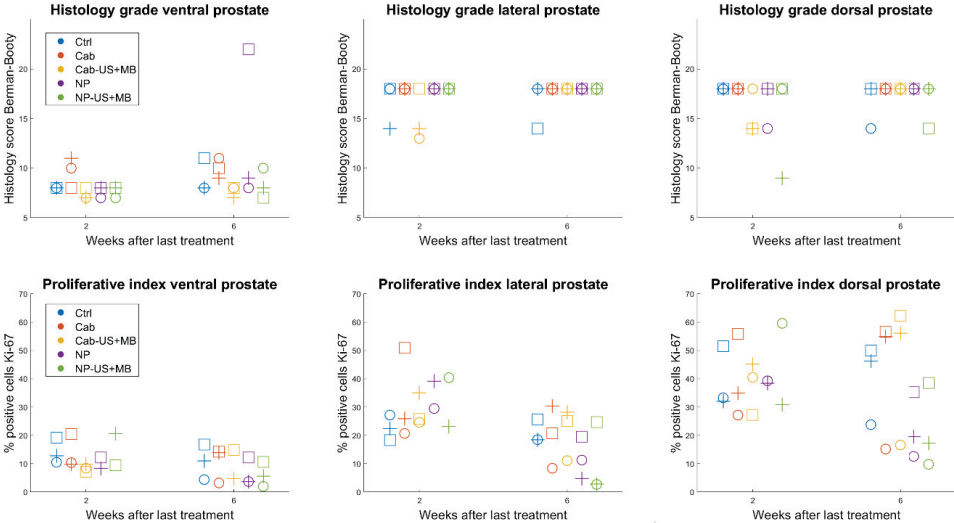


Figure 9. The top row shows histology grading using the Berman-Booty grading system two and six weeks after the last treatment for all different groups. The bottom row shows the proliferative index (% positive Ki-67 stained cells) for three different prostate lobes. Each symbol represents an individual mouse, some data points have perfect overlap.

NP and US+MB effect on cabazitaxel biodistribution

The biodistribution of Cab was assessed by MS quantification of Cab for samples harvested two hours after treatment in mice without PD tumors (Figure 10). Encapsulating Cab in NP enhanced the amount of Cab per mg of organ in all organs, especially in spleen, liver and blood. The blood concentration of free Cab was very low compared to Cab encapsulated in NPs. Cab was not detected in the brain for any mouse. The concentration of Cab in the prostate lobes was higher for NP groups than free Cab groups (Figure 10B). The mice were perfused, thus the increased uptake should be extravasated NP or drugs, although it cannot be ruled out that some NPs are left in the vessels. US+MB did not affect the amount of Cab neither in the prostate nor in any of the other organs two hours after treatment.

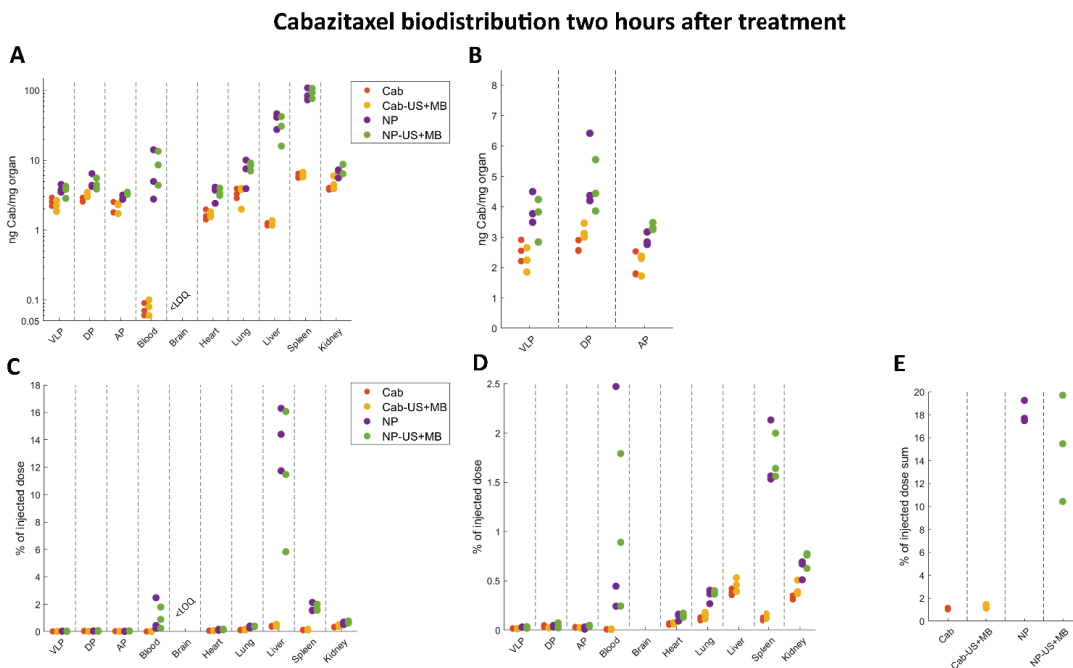


Figure 10.

A Amount of cabazitaxel (Cab) in ng per mg organ on a logarithmic axis for all organs and blood. The data points represent measurements from organs of individual mice, three per treatment group. **B** ng Cab per mg organ on a linear axis for the prostate lobes only. **C** % of injected dose in all organs and blood. **D** % of injected dose in all organs on a shorter axis to visualize differences between groups. **E** % of injected dose adding up the amount of Cab in all harvested organs 2 hours after treatment. Abbreviations: APL, anterior prostate lobe; Cab, cabazitaxel; DPL, dorsal prostate lobe; LOQ, limit of quantification and VPLP, ventral and lateral prostate lobe.

Apnea after NP injection

All mice receiving iv NP injections suffered from apnea and bradycardia immediately after injection. Data from four mice showed a mean apnea duration of 40 s, ranging from 38 to 43 s. The mean duration from start of bradycardia until the heart rate was the same as before

injection was 54 s, ranging from 50 to 57 s. The mean heart rate before injection was 441 bpm and the mean minimum heart rate after injection was 109 bpm. No mice died from the iv NP injection.

Weight loss

Body weight was assessed as a measure of toxicity and is displayed in Supplementary Figure 2. There was no significant difference in body weight between groups at start of treatment. Two weeks after end of treatment, the mean body weight of the untreated control was unchanged, whereas the treated mice had a mean reduction of 5-7% body weight. At this timepoint the difference was statistically significant between the control group (0.0% mean change in body weight) and the NP group (6.2% mean reduction in body weight), and the control group and the NP-US+MB group (7.1% mean reduction in body weight). Six weeks after end of treatment there was no significant difference in body weight between the groups.

Discussion

The treatment efficacy of Cab both with and without NP encapsulation and US+MB treatment was evaluated in the TRAMP model. To our knowledge, such a study has not been published before in a spontaneous, orthotopic prostate cancer model. The rationale behind this study was to verify the promising strategy of using NPs and US+MB for improving the delivery of drugs^{6,19} in a more clinically relevant model. Spontaneous orthotopic models are thought to represent human cancers better than xenografts, since mice are immunocompetent, have more heterogenous tumor genetics, and have organ specific stroma around the cancer cells⁷. The TRAMP model develops different phenotypes, which are probably representative of different types of human disease. Previous studies of TRAMP PD tumors have shown that they are positive for IHC staining for synaptophysin, indicating a neuroendocrine (NE) phenotype²⁴. In human disease, prostate cancer with a NE phenotype is rare and carries a poor prognosis²⁵. However, as prostate cancer progresses it sometimes differentiates to a NE phenotype in late stages of the disease. Studying the TRAMP PD neuroendocrine phenotype might therefore bring insights in treatment of the aggressive NE phenotype or transformed late-stage adenocarcinoma²⁶.

Most mice in this study did not develop PD tumors, but prostate volumes increased compared to wild-type mice²⁷ and histology revealed high grade PIN, classified by the Berman-Booty grading scheme²². Chiaverotti et. al²⁴ have argued that the dysplastic lesions in the TRAMP do not progress to cancer and that PIN is therefore a misleading term, since it implies a malignant potential. Generalizing from the non-tumor TRAMP mice to human disease is not straight forward, since it is unclear if it progresses to malignant disease. Depending on the grading scheme used, it could be argued that we have treated a benign condition, a premalignant condition or a malignant disease.

Treatment effect on PD tumor volume

A subgroup of the TRAMP mice developed PD tumors, and the therapeutic efficacy of Cab and Cab combined with US+MB was studied. Because of small numbers of PD tumors, the effect of NP encapsulation was not assessed. All mice with PD tumors responded to Cab or Cab combined with US+MB either by reduction of growth rate or reduction in PD tumor volume, demonstrating that Cab is an effective drug for PD tumors in the TRAMP model.

Degrassi¹⁵ et al. showed that doxorubicin can reduce the volume of PD tumors in the TRAMP¹⁵. Degrassi treated six mice with PD tumors with 7.5 mg/kg doxorubicin per week for three weeks and monitored treatment response with MRI. All tumor volumes were reduced, but three tumors started growing again during 40 days of follow up. Treating the PD tumors with Cab combined with US+MB had similar effects as Cab alone, except for one PD tumor, which disappeared completely on MRI imaging. However, the number of tumors is too small to conclude whether US+MB enhances the treatment effect of Cab. The results, however, are encouraging and are in line with observations using xenografts, where treating subcutaneous xenografts with drugs or NPs combined with US+MB caused reduced tumor growth and even resulted in complete remission¹⁹.

The benefit of using US+MB is probably greatest in tumors where extravasation and penetration of drug through the extracellular matrix limits drug delivery. In xenografts expressing low EPR, sonopermeation is reported to be more effective than in xenografts with high EPR²⁸. Thus, sonopermeation depends on tumor physiology, such as the vascular network and the composition and structure of the extracellular matrix, which are known to vary

between within and between tumors, which can explain some of the variation in therapeutic responses to US+MB.

Treatment effect on PIN prostate

All treatments that included Cab significantly reduced the prostate volume compared to both the starting volume and to the untreated controls. There was no clear added effect from using NPs or sonopermeation. This might indicate that Cab, either free or encapsulated, diffuses efficiently through the prostate and that sonopermeation does not improve the delivery and therapeutic response. NPs in the prostate might not encounter the same barriers as in solid tumors, such as the high interstitial fluid pressure and dense stroma²⁹⁻³¹. The observation that encapsulated Cab is as efficient as free drug is promising because encapsulating drugs have the potential to reduce toxicity from chemotherapeutic agents³².

The mean prostate volume regrew beyond the pre-treatment volume in all treatment groups during the 6 weeks after the last treatment. Since hyperplasia has a genetic cause that was not removed by the treatment, regrowth could be expected. Also, none of the mice were castrated, thus testosterone would still stimulate the prostate tissue to grow. The results are consistent with the few comparable studies available: Degrassi et. al.¹⁵ treated six TRAMP mice without tumors with 7.5 mg/kg doxorubicin weekly for three weeks and monitored treatment response with volume measurements based on MRI. They also observed a clear reduction in prostate size initially and a regrowth after end of treatment outgrowing the pre-treatment size. Sjøgaard et. al.¹⁶ treated the TRAMP with either docetaxel or docetaxel plus a peptide targeting the cellular scaffold protein PCNA. Both groups receiving docetaxel had smaller prostate volumes than the control up to four weeks after one treatment with 3 mg/kg docetaxel.

Histology grading and Ki-67 staining was done to assess treatment effects on the microscopic level. Both histology grading and Ki-67 staining did not show any difference between treatment groups and no difference between the two time points (two and six weeks after treatment), which is in line with results observed in prostate volume. The time points were chosen to late to detect the transient effect of the treatment. Several studies on prevention of cancer in the TRAMP model have shown reduction in the expression of Ki-67 in the model. For example though administration of the flavone apigenin³³ and a energy restriction mimetic agent³⁴. However, these studies assess the preventive effect of treatment and begin at young age, treat for a long time and often euthanize while therapy is still on-going.

Biodistribution

Improved therapeutic response requires an improved uptake of the drug in the tumor and in neoplastic cells. Thus, the prostate uptake of free and encapsulated Cab and the biodistribution in various organs were quantified with MS. Encapsulation of Cab into NPs had a clear effect on blood concentration and biodistribution two hours after intravenous administration. These results are in line with previous work on the biodistribution of the PEBCA NPs^{3,19}. The lungs also had increased levels of Cab when it was encapsulated in NPs, however the lungs were not perfused with PBS, making it difficult to separate the contribution from Cab in blood from Cab in lung tissue. Mice treated with Cab encapsulated in NPs had a higher Cab content in the different prostate lobes compared to mice treated with Cab, but the approximately 1.7 times higher uptake was not sufficient for any therapeutic improvement. Possible mechanisms for the higher uptake of encapsulated Cab are lower distribution volume,

longer circulation time and slower excretion. US+MB did not have any clear effect on prostate uptake for free Cab or Cab encapsulated in NP.

Toxicity

Throughout the study, injection of NPs led to transient apnea and bradycardia in the TRAMP mice. The apnea and bradycardia usually occurred simultaneously, which could indicate a reflex mediated response. The Bezold-Jarish reflex is known to give this effect in mice, and can be triggered by different stimuli, both chemical and mechanical³⁵. However, in previous studies in female Balb/c nude mice, NP injection did not lead to transient apnea^{3,19}. Further investigation is needed to find the cause of the apnea and bradycardia in the TRAMP mice. Clinical studies have shown that pulmonary disease is an important concern in clinical studies with polymeric NPs. In a phase II clinical trial with Doxorubicine Transdrug, a polymeric nanoformulation of doxorubicin using the PEBCA polymer (Livatag), 4 out of 17 patients developed acute respiratory distress syndrome, and three of them died³⁶.

Mice in all groups receiving free Cab or NPs lost weight during the treatment period. The mean weight loss for the treated groups was 5-7%. Fusser et. al.³ experienced a weight loss of around 15% with two treatments of 15 mg/kg of Cab both free and NP encapsulated three days apart when treating female athymic nude foxn1_{nu} mice. Snipstad et. al.¹⁹ treated female Balb/c nude mice with Cab in NPs 10 mg/kg weekly for two weeks which caused no weight loss¹⁹. Weight loss caused by Cab might be dependent of the mouse model and 10 mg/kg weekly might be close to the maximum dose tolerated in the TRAMP model.

Conclusion

Cabazitaxel reduces PD tumor and prostate volume in the TRAMP model, but the effect is transient and regrowth beyond pre-treatment volume took place after the end of treatment. The study did not show any clear added therapeutic efficacy from combining Cab with NP encapsulation or US+MB. These results differ from previous studies in xenograft models, which showed an improved treatment response from NP encapsulation and US+MB treatment. We did not see any effect on histology grading and proliferation marker staining two and six weeks after treatment. Quantification of Cab by MS showed a clear increase in Cab concentration in blood, liver and spleen from encapsulating Cab in NPs.

Acknowledgement

We acknowledge the support from and the use of the following infrastructures: Animal breeding, housing and genotyping was provided by the Comparative medicine Core Facility (CoMed). Histology and immunohistochemistry sectioning and staining was performed at the Cellular and Molecular Imaging Core Facility (CMIC). CoMed and CMIC are both at the Norwegian University of Science and Technology (NTNU) and are funded by the Faculty of Medicine at NTNU and Central Norway Regional Health Authority. MRI was performed at the MR core facility at the Norwegian University of Science and Technology. Equipment for therapeutic US was provided by The Norwegian Centre for Minimally Invasive Image Guided Therapy and Medical Technologies (NorMIT). We also acknowledge Yrr Mørch and Anne Hatletveit at SINTEF Industry for providing NPs and guidance. MS analysis was also performed at SINTEF Industry. The project was supported by the Research Council of Norway (project number 240316) and Central Norway Regional Health Authority.

References

1. Ferlay J, Colombet M, Soerjomataram I, et al. Cancer incidence and mortality patterns in Europe: Estimates for 40 countries and 25 major cancers in 2018. *European journal of cancer (Oxford, England : 1990)*. 2018;103:356-387.
2. Peer D, Karp JM, Hong S, Farokhzad OC, Margalit R, Langer R. Nanocarriers as an emerging platform for cancer therapy. *Nature nanotechnology*. 2007;2(12):751-760.
3. Fusser M, Overbye A, Pandya AD, et al. Cabazitaxel-loaded Poly(2-ethylbutyl cyanoacrylate) nanoparticles improve treatment efficacy in a patient derived breast cancer xenograft. *Journal of controlled release : official journal of the Controlled Release Society*. 2019;293:183-192.
4. Maeda H, Wu J, Sawa T, Matsumura Y, Hori K. Tumor vascular permeability and the EPR effect in macromolecular therapeutics: a review. *Journal of controlled release : official journal of the Controlled Release Society*. 2000;65(1-2):271-284.
5. Wilhelm S, Tavares AJ, Dai Q, et al. Analysis of nanoparticle delivery to tumours. *Nature Reviews Materials*. 2016;1(5):16014.
6. Snipstad S, Sulheim E, de Lange Davies C, et al. Sonopermeation to improve drug delivery to tumors: from fundamental understanding to clinical translation. *Expert opinion on drug delivery*. 2018;15(12):1249-1261.
7. Gengenbacher N, Singhal M, Augustin HG. Preclinical mouse solid tumour models: status quo, challenges and perspectives. *Nature reviews Cancer*. 2017;17(12):751-765.
8. Gingrich JR, Barrios RJ, Morton RA, et al. Metastatic prostate cancer in a transgenic mouse. *Cancer research*. 1996;56(18):4096-4102.
9. Greenberg NM, DeMayo F, Finegold MJ, et al. Prostate cancer in a transgenic mouse. *Proceedings of the National Academy of Sciences of the United States of America*. 1995;92(8):3439-3443.
10. Liu Y, Wu X, Jiang H. Combined maternal and post-weaning high fat diet inhibits male offspring's prostate cancer tumorigenesis in transgenic adenocarcinoma of mouse prostate model. *The Prostate*. 2019;79(5):544-553.
11. Raina K, Rajamanickam S, Singh RP, Deep G, Chittechath M, Agarwal R. Stage-specific inhibitory effects and associated mechanisms of silibinin on tumor progression and metastasis in transgenic adenocarcinoma of the mouse prostate model. *Cancer research*. 2008;68(16):6822-6830.
12. Wang L, Bonorden MJ, Li GX, et al. Methyl-selenium compounds inhibit prostate carcinogenesis in the transgenic adenocarcinoma of mouse prostate model with survival benefit. *Cancer prevention research (Philadelphia, Pa)*. 2009;2(5):484-495.
13. Silva RS, Kido LA, Montico F, Vendramini-Costa DB, Pilli RA, Cagnon VHA. Steroidal hormone and morphological responses in the prostate anterior lobe in different cancer grades after Celecoxib and Goniothalamin treatments in TRAMP mice. *Cell biology international*. 2018;42(8):1006-1020.
14. da Silva RF, Banzato TP, Alves LF, Carvalho JE, Agarwal R, Cagnon VHA. Antiangiogenic therapy with Nintedanib affects hypoxia, angiogenesis and apoptosis in the ventral prostate of TRAMP animals. *Cell and tissue research*. 2019.
15. Degrassi A, Russo M, Scanziani E, et al. Magnetic resonance imaging and histopathological characterization of prostate tumors in TRAMP mice as model for pre-clinical trials. *The Prostate*. 2007;67(4):396-404.
16. Sogaard CK, Moestue SA, Rye MB, et al. APIM-peptide targeting PCNA improves the efficacy of docetaxel treatment in the TRAMP mouse model of prostate cancer. *Oncotarget*. 2018;9(14):11752-11766.

17. Fagerland ST, Hill DK, van Wamel A, de Lange Davies C, Kim J. Ultrasound and magnetic resonance imaging for group stratification and treatment monitoring in the transgenic adenocarcinoma of the mouse prostate model. *The Prostate*. 2019.
18. Kaplan-Lefko PJ, Chen TM, Ittmann MM, et al. Pathobiology of autochthonous prostate cancer in a pre-clinical transgenic mouse model. *The Prostate*. 2003;55(3):219-237.
19. Snipstad S, Berg S, Morch Y, et al. Ultrasound Improves the Delivery and Therapeutic Effect of Nanoparticle-Stabilized Microbubbles in Breast Cancer Xenografts. *Ultrasound in medicine & biology*. 2017;43(11):2651-2669.
20. Schindelin J, Arganda-Carreras I, Frise E, et al. Fiji: an open-source platform for biological-image analysis. *Nature Methods*. 2012;9(7):676-682.
21. Bankhead P, Loughrey MB, Fernández JA, et al. QuPath: Open source software for digital pathology image analysis. *Scientific Reports*. 2017;7(1):16878.
22. Berman-Booty LD, Sargeant AM, Rosol TJ, et al. A review of the existing grading schemes and a proposal for a modified grading scheme for prostatic lesions in TRAMP mice. *Toxicologic pathology*. 2012;40(1):5-17.
23. Sulheim E, Morch Y, Snipstad S, et al. Therapeutic Effect of Cabazitaxel and Blood-Brain Barrier opening in a Patient-Derived Glioblastoma Model. *Nanotheranostics*. 2019;3(1):103-112.
24. Chiaverotti T, Couto SS, Donjacour A, et al. Dissociation of epithelial and neuroendocrine carcinoma lineages in the transgenic adenocarcinoma of mouse prostate model of prostate cancer. *The American journal of pathology*. 2008;172(1):236-246.
25. Sun Y, Niu J, Huang J. Neuroendocrine differentiation in prostate cancer. *American journal of translational research*. 2009;1(2):148-162.
26. Grabowska MM, DeGraff DJ, Yu X, et al. Mouse models of prostate cancer: picking the best model for the question. *Cancer metastasis reviews*. 2014;33(2-3):377-397.
27. Hill DK, Kim E, Teruel JR, et al. Diffusion-weighted MRI for early detection and characterization of prostate cancer in the transgenic adenocarcinoma of the mouse prostate model. *Journal of magnetic resonance imaging : JMRI*. 2016;43(5):1207-1217.
28. Theek B, Baues M, Ojha T, et al. Sonoporation enhances liposome accumulation and penetration in tumors with low EPR. *Journal of controlled release : official journal of the Controlled Release Society*. 2016;231:77-85.
29. Boucher Y, Baxter LT, Jain RK. Interstitial pressure gradients in tissue-isolated and subcutaneous tumors: implications for therapy. *Cancer research*. 1990;50(15):4478-4484.
30. Eikenes L, Tari M, Tufto I, Bruland OS, de Lange Davies C. Hyaluronidase induces a transcapillary pressure gradient and improves the distribution and uptake of liposomal doxorubicin (Caelyx) in human osteosarcoma xenografts. *Br J Cancer*. 2005;93(1):81-88.
31. Netti PA, Berk DA, Swartz MA, Grodzinsky AJ, Jain RK. Role of extracellular matrix assembly in interstitial transport in solid tumors. *Cancer research*. 2000;60(9):2497-2503.
32. Harris L, Batist G, Belt R, et al. Liposome-encapsulated doxorubicin compared with conventional doxorubicin in a randomized multicenter trial as first-line therapy of metastatic breast carcinoma. *Cancer*. 2002;94(1):25-36.
33. Shukla S, Bhaskaran N, Babcook MA, Fu P, Maclennan GT, Gupta S. Apigenin inhibits prostate cancer progression in TRAMP mice via targeting PI3K/Akt/FoxO pathway. *Carcinogenesis*. 2014;35(2):452-460.
34. Berman-Booty LD, Chu PC, Thomas-Ahner JM, et al. Suppression of prostate epithelial proliferation and intraprostatic progrowth signaling in transgenic mice by a new energy restriction-mimetic agent. *Cancer prevention research (Philadelphia, Pa)*. 2013;6(3):232-241.
35. Campagna JA, Carter C. Clinical relevance of the Bezold-Jarisch reflex. *Anesthesiology*. 2003;98(5):1250-1260.

36. Merle P, Camus P, Abergel A, et al. Safety and efficacy of intra-arterial hepatic chemotherapy with doxorubicin-loaded nanoparticles in hepatocellular carcinoma. *ESMO Open*. 2017;2(4):e000238.

Supplements

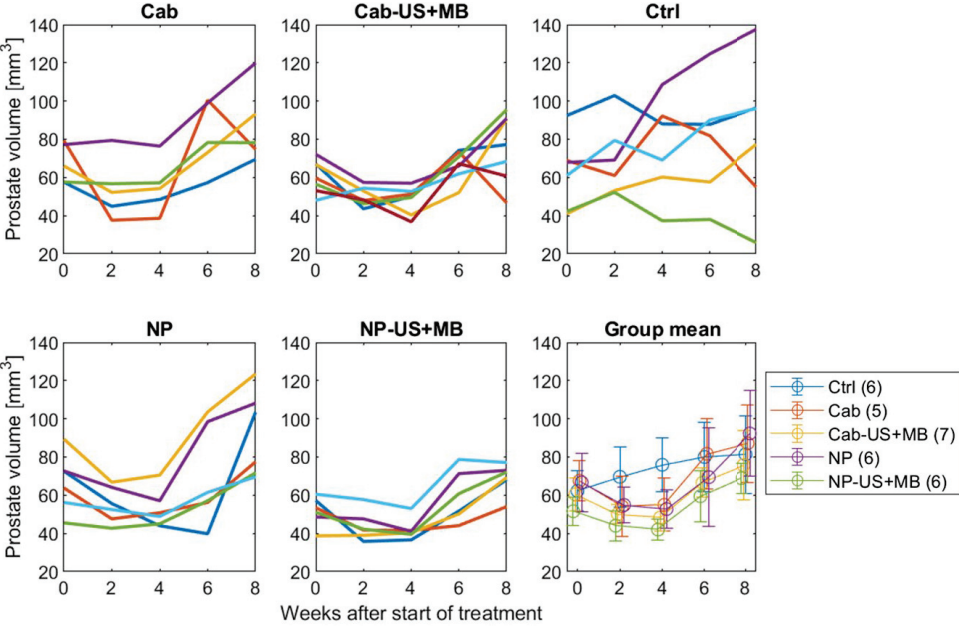


Figure S1

Individual plots of mice followed from before treatment until eight weeks after start of treatment. Absolute prostate volume as a function of time after start of treatment. Relative prostate volume as a function of time after start of treatment. Treatment was given in week 0, 1 and 2. The lower right plot show the mean values and standard deviation for each group. Abbreviations: Ctrl, control; Cab, cabazitaxel; Cab-US+MB, cabazitaxel combined with therapeutic ultrasound and microbubbles; NP, cabazitaxel encapsulated in nanoparticles and NP-US+MB, cabazitaxel encapsulated in nanoparticles combined with therapeutic ultrasound and microbubbles.

Body weight change over time since start of treatment

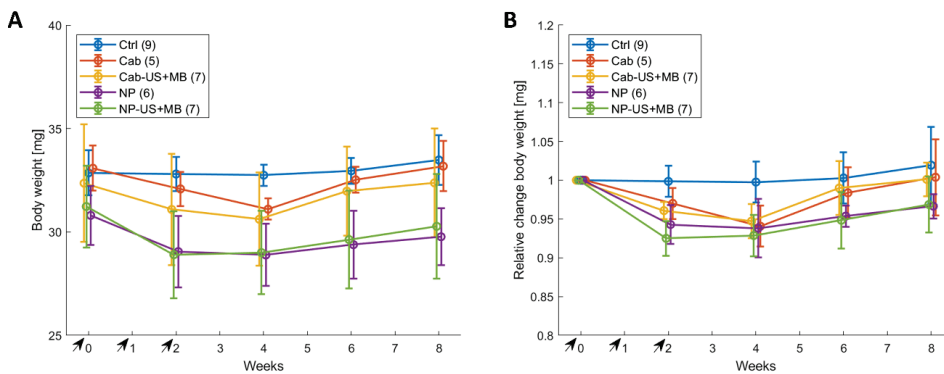


Figure S2

Body weight from start of treatment as a function of time. Treatment was given in week 0, 1 and 2 (marked with arrows). The colored lines show group mean and the error bars show standard deviation. The number of animals per group is given in the figure legend. **A** Change in absolute body weight. **B** Change in relative body weight. Abbreviations: Ctrl, control; Cab, cabazitaxel; Cab-US+MB, cabazitaxel combined with therapeutic ultrasound and microbubbles; NP, cabazitaxel encapsulated in nanoparticles and NP-US+MB, cabazitaxel encapsulated in nanoparticles combined with therapeutic ultrasound and microbubbles.

ISBN 978-82-326-4546-6 (printed ver.)
ISBN 978-82-326-4547-3 (electronic ver.)
ISSN 1503-8181